UNIVERSITÀ DEGLI STUDI DI PAVIA
DOTTORATO DI RICERCA IN FISICA – XXXIII CICLO

Measuring Z boson production in heavy-ion collisions with ALICE

with a view on the upgrade of the experiment

Nicolò Valle

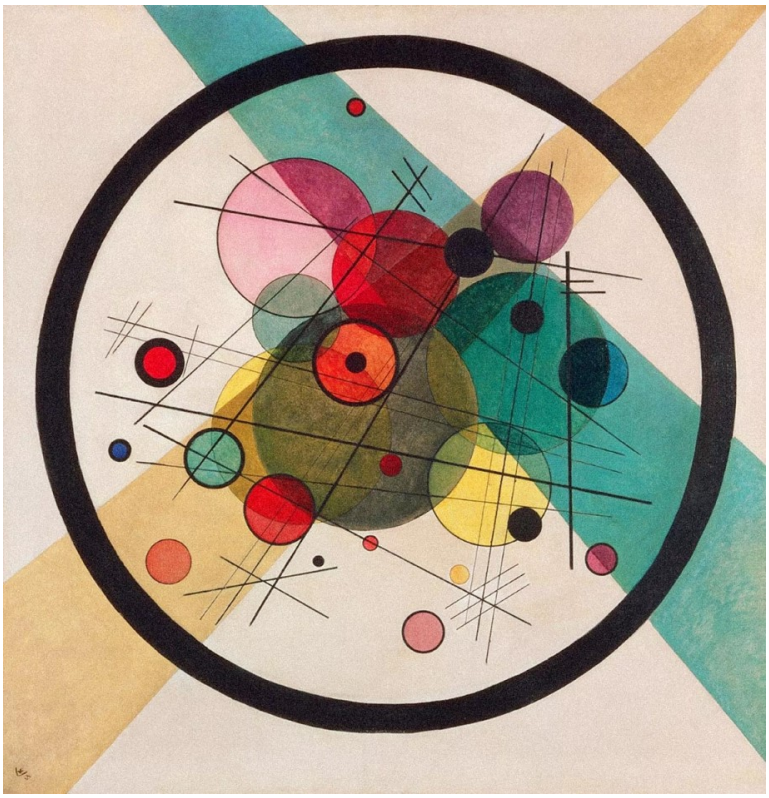

Tesi per il conseguimento del titolo

Università degli Studi di Pavia

Dipartimento di Fisica

DOTTORATO DI RICERCA IN FISICA - XXXIII CICLO

Measuring Z boson production in heavy-ion collisions with ALICE

with a view on the upgrade of the experiment

Nicolò Valle

Submitted to the Graduate School of Physics in partial fulfillment of the requirements for the degree of *Dottore di Ricerca in Fisica* at the University of Pavia

Supervisor: Prof. Gianluigi Boca

Cover: *Circles in a Circle*, W. Kandinsky, 1923.

Measuring Z boson production in heavy-ion collisions with ALICE, with a view on the upgrade of the experiment
Nicolò Valle
Ph.D. thesis - University of Pavia
Pavia, November 2020

Introduction

> "The data provide evidence for colour deconfinement in the early collision stage and for a collective explosion of the collision fireball in its late stages. The new state of matter exhibits many of the characteristic features of the theoretically predicted Quark-Gluon Plasma."

This is part of the abstract of a special seminar given by L. Maiani and the spokespersons from CERN's SPS experiments on 10th February 2000.[1] It is the first announcement of the creation in a laboratory of a state of matter made of deconfined quarks and gluons. In the last ten years, the experimental results originated in the relatively low SPS energy scale have been expanded and the Quark-Gluon Plasma (QGP) was rediscovered again with the higher energies provided at the Relativistic Heavy Ion Collider (RHIC) and the Large Hadron Collider (LHC).

The interest in this research is driven by the many open points about the nature of the interaction between quarks and gluons, as well as by cosmological reasons (free quarks and gluons were the elementary degrees of freedom in the early stage of the universe). I like to underline some striking features of this interaction. The theoretical framework is a gauge theory known as Quantum Chromodynamics (QCD) and it is formulated in terms of colour-charged particles which have never been observed free in nature. They only exist as bound states, more complex particles named hadrons. Although much of the physics of QCD is well understood, some questions still remain unresolved, such as the origin of the confinement of quarks and gluons and the mechanism of the generation of the mass. They can be investigated by bringing the hadronic matter at the extreme conditions of high matter and energy densities. The technological progress of the last decades has provided us with the possibility of achieving these conditions in the laboratory by colliding heavy ions.

[1] http://cdsweb.cern.ch/record/431351/. Maiani was at that time the CERN Director-General.

The experimental handles for the study of the QGP are many. Some of them will be presented in this thesis, which is focused on the interactions between lead ions measured by the ALICE experiment at the LHC. More attention will be given to the initial state of the collisions. The physics of heavy ions is indeed not limited to the phenomenology of the hot matter created when they collide. The nuclear environment modifies the behavior of the nucleons and their constituents independently on the subsequent QGP formation. The investigation of such "cold" nuclear effects is interesting in itself being at the boundary between nuclear and particle physics, but it also constitutes a necessary reference for the correct interpretation of those effects induced by the presence of the hot medium.

Content of this thesis

This thesis aims at presenting the research activity I carried out within the ALICE Collaboration. The core of this work is the measurement of Z boson production in lead-lead collisions at the nucleon-nucleon center-of-mass energy $\sqrt{s_{\mathrm{NN}}} = 5.02$ TeV . Electroweak bosons are a clean tool for the investigation of the aforementioned cold nuclear effects, and in particular the nuclear modification of the Parton Distribution Functions (PDFs). For this reason the main goal of the analysis is to enrich the small existing database with new measurements able to constrain the nuclear-modified PDFs in a kinematic region where they are known with the largest uncertainty.

Chapter 3 gives the details of my work on the analysis of the entire Pb-Pb data sample collected by ALICE at $\sqrt{s_{\mathrm{NN}}} = 5.02$ TeV . Before that, the importance of this research and the state of the art on these measurements are reviewed. The first chapter of the thesis presents different aspects of the heavy ion collisions. An overview is given on the geometry of the collision and on the physics of the QGP. The last sections are dedicated to the cold matter effects and in particular to the nuclear PDFs. The second chapter presents the ALICE Experiment and part of its physics program. The results of my work are presented and discussed at the end of chapter 3. The measurements will show the presence of a significant suppression of the Z production due to nuclear modification of the PDFs. This is actually the strongest evidence of nuclear shadowing measured by ALICE with gauge bosons. The results of the analysis have been approved by the Collaboration, presented in different international conferences and they are published in reference [69].

Finally the last chapter, given as an appendix, is dedicated to the ongoing operations on the ALICE upgrade. Since the beginning of the second LHC Long Shutdown (end of 2018), both LHC and the Experiments put their effort in the upgrade activities. I took part in such activities by collaborating in the assembly

and commissioning of the new ALICE silicon pixel tracker. In particular, the last chapter of the thesis will be dedicated to the description of a cycle of quality and ageing tests I performed on the detector to confirm its robustness for the next years of operation. The results are described in this thesis and are published in reference [126].

Contents

Chapter 1

Colliding nuclei at the LHC

The Large Hadron Collider (LHC) at CERN not only collides protons. So far collisions between lead ions, xenon ions and between protons and lead ions have been provided at multiple energies. At the highest energies the phenomenology of the collisions is enriched by the formation of a phase of matter at high temperature ruled by the strong interaction. In this chapter the mechanisms, the phenomenology and the usefulness of the collisions between heavy ions are introduced.

1.1 Heavy ion beams

The LHC synchrotron operates at the end of a complex chain of injectors which pre-accelerate and prepare the beam for its requirements. Such accelerator complex is schematically illustrated in figure 1.1. The lead ions journey starts from a 2 centimeters long block of lead enriched with the isotope ^{208}Pb. With an Electron Cyclotron Resonance (ECR) multi-charged states are generated with the help of heat, magnetic fields and microwaves [1]. A spectrometer extracts the Pb^{27+} charge state, which is accelerated to 4.2 MeV per nucleon and redirected on a carbon foil which strips off the ions to the Pb^{54+} state. The beam is then accelerated in the LEIR (Low Energy Ion Ring) to 72 MeV per nucleon and sent to the PS (Proton Synchrotron). Here the ion bunches are re-shaped, accelerated to 5.9 GeV/nucleon and sent to the SPS. Another stripper foil in the transfer line removes the remaining electrons, so that ions arriving to SPS are fully ionized. The SPS accelerates to the energy of 450 Z GeV (Z is the electric charge) and the beam is finally injected into the LHC [2].

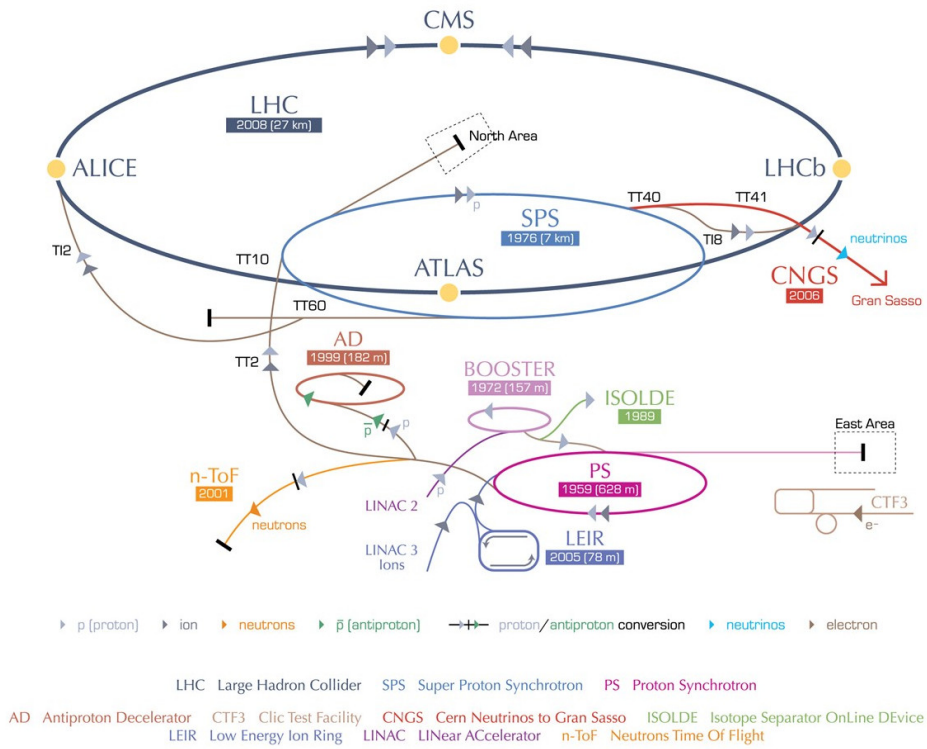

Figure 1.1. The CERN accelerator complex [3].

1.1.1 Heavy ion collisions during LHC Run2

In the period between 2015 and 2018 the Large Hadron Collider operations involved a total of 12 weeks of running time with collisions between protons and heavy ions or between heavy ions. Two main different collision modes were exploited, as summarized in the following table [4]. Together with lead nuclei collisions, a special one-day run with xenon beams, at the nucleon-nucleon center-of-mass energy $\sqrt{s_{\mathrm{NN}}} = 5.44$ TeV , was done in October 2017 [5]. The preparation of LHC for a heavy ion run is a challenging operation, made more complex by the short run time. In contrast to proton-proton operations, when running heavy ion beams almost every fill[1] is run with a variable number of bunches and different configurations. This has been proven to result in steady performance gains (see ref. [6] for a review of some technical details).

[1] A "fill" is a period of activity with stable conditions. At each fill a dose of particles is injected in the accelerator, accelerated to the maximum energy, made to collide and finally dumped. There are hundreds of fills in each year of activity.

Year		Beam energy ($Z = 1$ or $Z = 82$)	Nucleon-nucleon c.m.s. energy, $\sqrt{s_{\mathrm{NN}}}$
2015 (3 weeks)	Pb-Pb	6.37 Z TeV	5.02 TeV
2016 (4 weeks)	p-Pb	4 Z TeV and 6.5 Z TeV	5.02 and 8.16 TeV
2018 (4 weeks)	Pb-Pb	6.37 Z TeV	5.02 TeV

Table 1.1. Heavy ion program during LHC Run2 operations.

If a proton and a nucleus with charge and mass number Z and A are accelerated in the same magnetic configuration, their energies differ by a factor Z: $E_{\mathrm{nucleus}} = Z\,E_p$. In the case of nuclei, the total energy is split among A nucleons. When two ultrarelativistic (negligible mass) nucleons collide with energies E_{N1} and E_{N2} in the laboratory frame, their total center-of-mass (c.m.s.) energy can be expressed as $E_{\mathrm{c.m.s.}} = 2\sqrt{E_{N1}\,E_{N2}}$. It follows that when the accelerator is in a magnetic configuration allowing beams with energy $E = Z\,E_p$, the nucleon-nucleon center-of-mass energy of the colliding hadrons is

$$\sqrt{s_{\mathrm{NN}}} = 2\sqrt{\frac{Z_1 Z_2}{A_1 A_2}}\,E_p$$

In the 2016 proton-lead runs ($Z_1 = A_1 = 1$, $Z_2 = 82$, $A_2 = 208$), the beam energy was tuned according to different LHC experiments requirements. A complex run scheme was used to provide maximum energy beams ($E_p = 6.5$ TeV) to ATLAS, CMS, ALICE and beams with $E_p = 4$ TeV to ALICE which required also low-luminosity operations at the same energy of the data collected in 2013. Because of the asymmetry of the collision, the nucleon-nucleon center of mass system of proton-nucleus collisions is boosted with respect to the laboratory in the direction of the proton beam. Analogously, the acceptance of the detectors is shifted in rapidity with respect to the center of mass of the collision. This allows to investigate different kinematic regions by reversing the directions of the beams, an important fact in view of the results shown in chapter 3.

During the 2015 and 2018 runs, two symmetric lead ion beams with energy 6.37 Z TeV collided, resulting in $\sqrt{s_{\mathrm{NN}}} = 5.02$ TeV . The energy was reduced with respect to the maximum nominal energy $E_p = 6.5$ TeV to match the center-of-mass energy of the proton-lead runs performed during Run1 [7]. The bunch

spacing in these runs ranged from 150 ns in 2015[2] to 75 ns in 2018. The number of bunches circulating in the LHC depends on the fill and is of the order of some hundreds. Few hundreds of millions of ions ($\mathcal{O}(10^8)$) are present in each bunch. The luminosity delivered to each experiment depends on the experiment requests. In 2018 the ALICE and LHCb luminosity was leveled to $10^{27}\,\mathrm{cm}^{-2}\mathrm{s}^{-1}$ (this can be done by separating the beams at the interaction point), while peaks more than six times greater were reached at ATLAS and CMS. The integrated luminosity is displayed in figure 1.2.

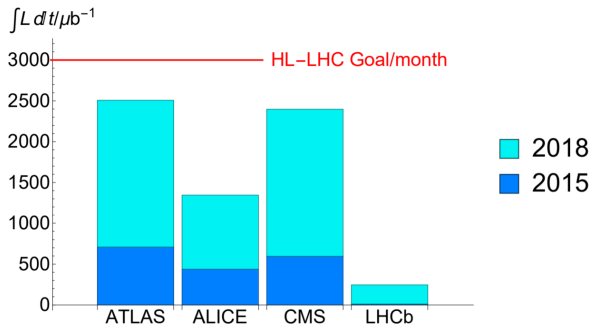

Figure 1.2. Integrated Pb-Pb luminosity delivered to each experiment in 2015 and 2018. The luminosity achieved in Run2 is compared to the goal for High-Luminosity (HL) LHC operation. Figure adapted from [8].

1.2 The geometry of the collision

The description as point-like particles is not suitable for heavy ions, since the nuclei are objects with finite dimension and the relative position between the colliding particles is experimentally sizable.

1.2.1 Glauber Model

The Glauber theory helps to describe the particle production of a collision between heavy ions in terms of an incoherent superposition of an equivalent number of collisions between nucleons. The main assumption is the so-called "eikonal" approximation, which considers the nucleons traveling in straight line trajectories, not changing when passing through the other nucleus [9]. The assumption relies on the fact that the energies are high enough to make the interaction ending before any induced nuclear rearrangement can take place. According to this

[2]More precisely, the bunches were grouped in trains, with an alternating 100/225 ns spacing, then reduced to 100/150 ns, as explained in [7].

picture, two fundamental numbers are defined.

- The number of nucleons participating in the collisions, N_{part} . It counts the total number of nucleons which undergo at least one nucleon-nucleon collision. The nucleons not participating in the collision are called "spectators". If A and B are the mass numbers of the nuclei, it will be $N_{\text{part}} + N_{\text{spec}} = A + B$.

- The number of binary collisions, N_{coll} . Each of the participating nucleon is assumed to collide inelastically with the same $\sigma_{\text{inel}}^{\text{NN}}$ cross section with all the nucleons present on its straight trajectory. This defines the number of nucleon-nucleon binary collisions.

Given the nuclei species, the geometry of the collision is determined by the projection of the distance between the centers of the nuclei on the transverse plane, which is called **impact parameter** and it is named b. The numbers N_{coll} and N_{part} for a collision with a given impact parameter depend on the second assumption of the Glauber model: the density distribution functions $\rho(\vec{r})$ of the nuclei. For nuclei with spherical symmetry, it is usually parameterized by a Fermi distribution with two parameters (also known as Woods-Saxon function [10]):

$$\rho(\vec{r}) = \rho_0 \left[1 + \exp\left(\frac{r - R}{a}\right)\right]^{-1} \tag{1.2.1}$$

We choose to follow the ALICE Collaboration centrality determination paper (reference [11]) choosing ρ_0 such that the density function is normalized to the mass number, $\int d^3\vec{r}\,\rho(\vec{r}) = A$. Another common convention is to normalize it to unity.

A number of variables extracted with the Glauber model are widely used in the impact parameter-dependent studies of the particle production in heavy ion collisions. Among them there are the centrality and the nuclear overlap function T_{AB}. To be able to define them, let's first introduce the transverse density of the nucleus T_{A}. Using the vector $\vec{s}$ to identify the position on the transverse plane, it is defined as

$$T_{\text{A}}(\vec{s}) = \int_{-\infty}^{+\infty} dz\, \rho(\vec{s}, z)$$

$T_{\text{A}}(\vec{s})\, d^2\vec{s}$ is the number of nucleons in the nucleus A in the differential area $d\vec{s}$. Let's now look at figure 1.3 where two flux tubes located at position $\vec{s}$ and $\vec{s} - \vec{b}$ in the respective nuclei are going to collide. The density function

$$T_{\text{A}}(\vec{s})\, T_{\text{B}}(\vec{s} - \vec{b})\, d^2\vec{s}\, d^2\vec{b}$$

represents the product of the number of nucleons in each nucleus which are in

the flux tubes. This is also the number of times two nucleons cross each other's trajectory. Spanning over $\vec{s}$, one obtains the number of such crossings that happens when the distance between the nuclear centers is fixed to $\vec{b}$. This brings to the definition of T_{AB}:

$$T_{\mathrm{AB}}(\vec{b})\, d^2\vec{b} = \left(\int d^2\vec{s}\ \ T_{\mathrm{A}}(\vec{s})\, T_{\mathrm{B}}(\vec{s}-\vec{b}) \right) d^2\vec{b}$$

For non-polarized nuclei the vector impact parameter can be replaced by the scalar value b. Because of the cylindrical symmetry, it holds $d^2\vec{b} = 2\pi b\, db$. $T_{\mathrm{AB}}(b)$, which has the unit of inverse area, is called nuclear overlap function. It can be interpreted as a nucleon-nucleon particle flux or luminosity when the impact parameter is b. The mean number of inelastic collisions is indeed given by the number of crossing nucleons, divided by the flux transverse area $d^2\vec{b}$ and multiplied by the nucleon-nucleon cross section:

$$N_{\mathrm{coll}}(b) = T_{\mathrm{AB}}(b)\, \sigma_{\mathrm{inel}}^{\mathrm{NN}} \tag{1.2.2}$$

The total inelastic nucleus-nucleus cross section is defined as the probability that some interaction occurs at impact parameter b integrated over $\vec{b}$. For $A,\, B \gg 1$ a poissonian distribution can be assumed for N_{coll} so that the probability of no interaction is $\exp\left[-T_{\mathrm{AB}}(b)\, \sigma_{\mathrm{inel}}^{\mathrm{NN}}\right]$. According to this,

$$\sigma_{\mathrm{inel}}^{\mathrm{AB}} = \int d^2\vec{b}\ \ \frac{d^2\sigma_{\mathrm{inel}}^{\mathrm{AB}}}{db^2} \ = \int 2\pi b\, db\ \left[1 - e^{-T_{\mathrm{AB}}(b)\, \sigma_{\mathrm{inel}}^{\mathrm{NN}}}\right] \tag{1.2.3}$$

The mean number of participants $N_{\mathrm{part}}(b)$ can be assessed by thinking of the overlap of the flux tubes from the point of view of each of the nucleons in A. The number of the interactions for each of them follows a binomial distribution with elementary probability given by $(T_{\mathrm{A}}/A) \times \sigma_{\mathrm{inel}}^{\mathrm{NN}}$. From this the number of nucleons experiencing at least one interaction can be computed. More details can be found in [12] but in practice these numbers are calculated with Monte Carlo simulations based on the Glauber Model, as will be explained soon.

1.2.2 Hard processes and nuclear modification factor

Hard collisions are processes where the interaction takes place between partons with a high momentum transfer. Thanks to the high energy scale, the cross section of such processes can be computed with theoretical calculations based on perturbative QCD. From the factorization theorem it follows that the number of hard processes between the point-like partons in a nucleus-nucleus colli-

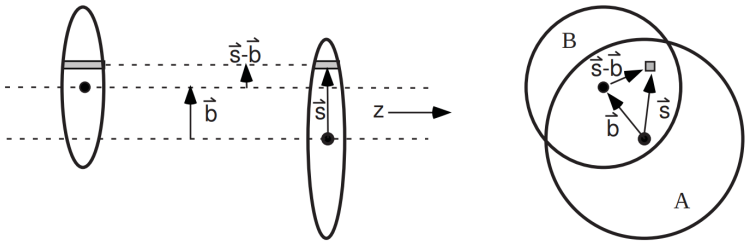

a) Side View b) Beam-line View

Figure 1.3. Picture of the collision between two nuclei A and B. The Glauber Model computations are performed assuming that the nucleons in the flux tube parallel to the beam axis go straight and interact with probability proportional to $\sigma_{\text{inel}}^{\text{NN}}$ with all the nucleons found on their trajectories. Image taken from [12].

sion is proportional to the number of binary collisions, therefore to the nuclear overlap function [13]. This is true if the hypothesis of incoherent sum of many nucleon-nucleon collisions holds. The comparison between the production yields in nucleus-nucleus collisions and in nucleon-nucleon collisions provide clean information on the deviation from this hypothesis, namely on the collective effects happening inside the nucleus. The yield is defined as the number of particle produced of a certain species divided by the number of nucleus-nucleus inelastic interactions. According to the T_{AB} scaling, an expression similar to eq. (1.2.2) can be used for the number of hard processes per collision. The total number of occurring events is then obtained by multiplying by the number of interactions.

$$Yield_{\text{hard}}^{\text{AB}} = \frac{N_{\text{hard}}^{\text{AB}}}{N_{\text{inel}}^{\text{AB}}} = \frac{\langle T_{\text{AB}} \rangle \, \sigma_{\text{hard}}^{\text{NN}} \, N_{\text{inel}}^{\text{AB}}}{N_{\text{inel}}^{\text{AB}}} = \langle T_{\text{AB}} \rangle \, \sigma_{\text{hard}}^{\text{NN}}$$

The average notation "$\langle\rangle$" is used because the counting is generally done on a wide range of impact parameters. The **nuclear modification factor** characterizes the deviations from this benchmark. It is defined as

$$R_{\text{AB}} = \frac{Yield^{\text{AB}}}{\langle T_{\text{AB}} \rangle \, \sigma^{\text{NN}}} \tag{1.2.4}$$

or other equivalent forms obtained by using $\langle N_{\text{coll}} \rangle$ instead of $\langle T_{\text{AB}} \rangle$. For hard processes it is expected to be equal to one in the absence of nuclear effects. The value of R_{AA} for Z boson production in Pb-Pb collisions at the nucleon-nucleon energy of 5.02 TeV will be computed in chapter 3 and will be found to be different from unity because of the nuclear modification to the parton distribution functions of the quarks inside the nucleus.

1.2.3 Centrality determination

In order to extract information on the impact parameter of a collision recorded in the experiment, the model has to be compared to an experimental observable. The multiplicity of the particles produced in the collision is suitable to this purpose. Indeed, the multiplicity spectrum is rather insensitive to nuclear collective effects and to the detailed mechanisms of particle production. This makes it a powerful tool for the characterization of the geometry of the collisions.

Phenomenologically, while the rate of hard processes scales with the number of binary nucleon-nucleon collisions, the soft particle production is found to scale approximately with $\langle N_{\mathrm{part}} \rangle$ over a wide range of energy [14]. The effective number of independently emitting sources of particles (S) can be therefore modeled by mixing the two contributions with a parameter $f \in [0, 1]$:

$$S = f \cdot N_{\mathrm{part}} + (1 - f) \cdot N_{\mathrm{coll}} \tag{1.2.5}$$

The dependence on the impact parameter can be computed with the so-called Glauber Monte Carlo. Its essential ingredients are the parameters of the Fermi distribution $\rho(\vec{r})$ and the nucleon-nucleon inelastic cross section. The simulation used for the results presented in chapter 3 uses the values from [15] and references therein. The colliding nuclei are ^{208}Pb. The radius parameter R is 6.69 ± 0.03 fm, while the skin thickness a which indicates how quickly the nuclear density goes to zero near the edge of the nucleus is 0.52 ± 0.02 fm. The nucleon-nucleon inelastic cross section at the desired energy is obtained by interpolating data from pp and p$\bar{\mathrm{p}}$ colliders, as well as cosmic ray experiments. At $\sqrt{s_{\mathrm{NN}}} = 5.02$ TeV the best choice is 67.6 ± 0.6 mb.

Once the parameters of the model are given, the simulation can be performed in the following way [11]. The coordinates of the nucleons in the nuclei are randomly drawn from the $\rho(\vec{r})$ distribution. The nucleus-nucleus collision is then treated as a sequence of independent interactions between nucleons which face each other along their straight trajectories. The concept of "facing each other" is implemented by assuming that two nucleons collide if their impact parameter is less than $\sqrt{\sigma_{\mathrm{inel}}^{\mathrm{NN}} / \pi}$. This means that the nucleons are treated as solid spheres with transverse area equal to $\sigma_{\mathrm{inel}}^{\mathrm{NN}}$. From here it is easy to count the number of colliding nucleons and the number of collisions they experience. When simulating collisions in the fully inclusive impact parameter range, $\vec{b}$ is drawn uniformly up to a maximum of $b = 20$ fm, large enough to simulate collisions until the point at which there are no more interactions. Following eq. (1.2.2) the nuclear overlap function is calculated as $T_{\mathrm{AA}} = N_{\mathrm{coll}} / \sigma_{\mathrm{inel}}^{\mathrm{NN}}$. The extracted quantities are plotted as a function of the impact parameter (expressed as centrality, described in the

following) in figure 1.4. An example of energy dependence is also reported.

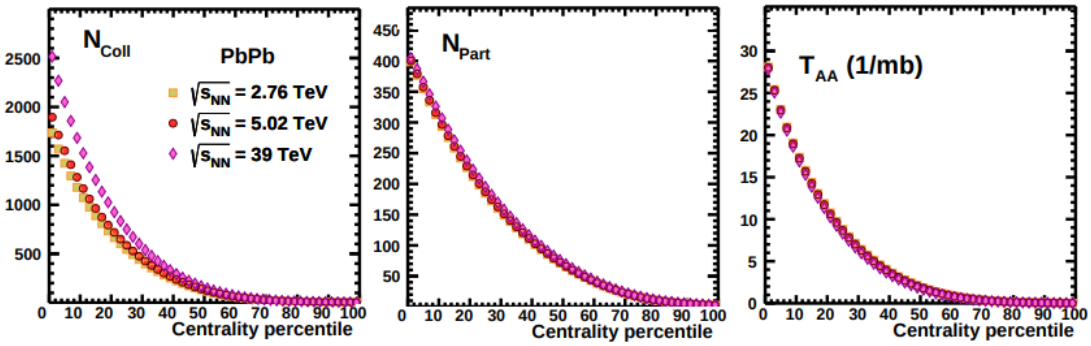

Figure 1.4. Number of binary collisions, number of participants and nuclear overlap function as a function of centrality in Pb-Pb collisions at three different energies. Values computed with Glauber Monte Carlo. Image taken from [12].

What is still missing is the recipe for the experimental determination of the impact parameter... but a precise event-by-event determination is not possible! As explained below, the measurements are done on a statistical basis. Related to the impact parameter is the concept of **centrality**. It is defined as the percentage of the total inelastic cross section that two nuclei colliding within a certain impact parameter experience. The definition is quite simple if referred to formula (1.2.3). The integral written there is performed on any value of b. By limiting the integral to a finite value of b one obtains the corresponding centrality class (cc):

$$\sigma_{\text{inel}}^{\text{AB}} \times cc(b) = \int_0^b 2\pi b'\, db' \left[1 - e^{-T_{\text{AB}}(b')\,\sigma_{\text{inel}}^{\text{NN}}}\right] \tag{1.2.6}$$

cc is expressed as a percentage value. Despite the name "centrality", from the definition follows that events in a centrality class with the highest percentage (let's say from 90% to 100%) are the most peripheral ones, with large impact parameter. Events with centrality close to 0% are the most central ones.

The particle multiplicity[3] is proportional to the nucleus-nucleus cross section and, as we said, it is an experimental observable serving as benchmark for the centrality determination. To do so, it has first to be reproduced by the Glauber Monte Carlo. For each interaction the number of generated particles is extracted from a negative binomial distribution, which has been found to well reproduce the charged particle multiplicity in a wide range of rapidity and collision

[3]To be more precise, the experimental observable is the *charged* particle multiplicity.

energy [16]. The density function is

$$p(n;\mu,k) = \frac{\Gamma(n+k)}{\Gamma(n+1)\,\Gamma(k)} \cdot \frac{(\mu/k)^n}{(\mu/k+1)^{n+k}}$$

where μ is the mean multiplicity for each of the S sources written in equation (1.2.5). $p(n)$ is the probability of producing n particles per source; the parameter k controls the width of the distribution. The multiplicity calculated with this method is compared with the one measured in the experiment. ALICE uses two arrays of scintillator counters called V0 (or VZERO) located at forward and backward rapidity at $\sim$ 330 and $\sim$ 90 cm from the beams interaction point respectively [17]. The measured V0 signal amplitude in Pb-Pb collisions at $\sqrt{s_{\mathrm{NN}}} = 5.02$ TeV is shown in figure 1.5. It is fitted with the multiplicity distribution resulting from the Glauber Monte Carlo. The fit is performed for V0 amplitudes large enough so that the purity of the event sample and the efficiency of the event selection are maximum. The χ^2 value is minimized in order to find the best values for the μ, k and f parameters. The mean values of N_{part} , N_{coll} and T_{AA} are computed by cutting the simulated V0 amplitude in slices corresponding to a percentage of the total amplitude equal to the centrality percentage, as shown in the figure. Since the events under study are unbiased, i.e. without any requirement on the final states (they are actually known as "Minimum Bias" events), this procedure makes the centrality to be uniformly distributed over the recorded events. In other words, **the distribution of the number of Minimum Bias is flat versus centrality**. The uncertainties on $\langle N_{\mathrm{part}} \rangle$, $\langle N_{\mathrm{coll}} \rangle$ and $\langle T_{\mathrm{AA}} \rangle$, as well as on their dispersions, are estimated by varying the input parameters of $\rho(\vec{r})$ and $\sigma_{\mathrm{inel}}^{\mathrm{NN}}$ within their uncertainties and repeating the simulation.

Because of the dispersion of the multiplicity distribution, an event sample at fixed multiplicity will always contain collisions in a finite range of impact parameters. Impact parameter and multiplicity are correlated but the accuracy of an event-by-event determination is not infinite and the precise value of b for a given event cannot be measured.

1.3 Quarks matter

The theory of strong interactions is formulated in terms of color charged quarks and gluons. One of the most exciting features of such theory is that color charged objects are absent in nature. This fact is known as confinement and can be explained by assuming that the energy necessary to separate two quarks increases with their distance. When trying to do so, the potential grows to the point that a new pair of quarks can be created from the vacuum. They combine with the exist-

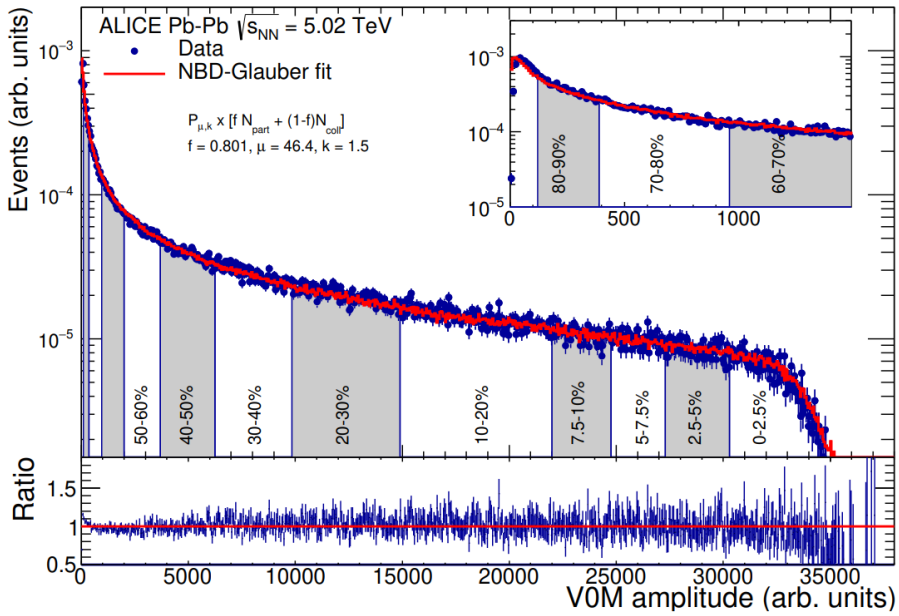

Figure 1.5. Spectrum of the signal amplitude recorded in the V0 detectors by ALICE during the 2018 Pb-Pb data taking, at the energy $\sqrt{s_{\mathrm{NN}}} = 5.02$ TeV . The measurement is fitted with the result of the Monte Carlo simulation based on Glauber model (see text for the meaning of the fitted parameters). Image from [11].

ing ones making again a colourless bound state. In Quantum Chromodynamics (QCD) this is formalized in terms of the asymptotic freedom (Gross, Wilczek [18] and Politzer [19], 1973). Contrary to the confinement, the asymptotic freedom foresees that the strong interaction becomes arbitrarily weak at small distances. The energy dependence of the QCD coupling constant α_s is shown in figure 1.6. This suggests that at high energy (small distances) a phase transition could happen when the strong force becomes weak to the point that gluons and quarks are not bounded in hadrons anymore.

The thermodynamic properties of a system are well summarized in terms of a phase diagram in the space of the thermodynamic parameters. In the case of QCD, the temperature T and the baryochemical potential μ_B can play this role. μ_{B} is the potential associated to the baryon number B (difference between the number of baryon and antibaryons) such that the partition function of the system can be written as the sum

$$Z(T, \mu_B) = \sum_{\alpha} \left[-\frac{E_\alpha - \mu_B B_\alpha}{T} \right]$$

over the eigenstates $\{\alpha\}$ of the QCD Hamiltonian.

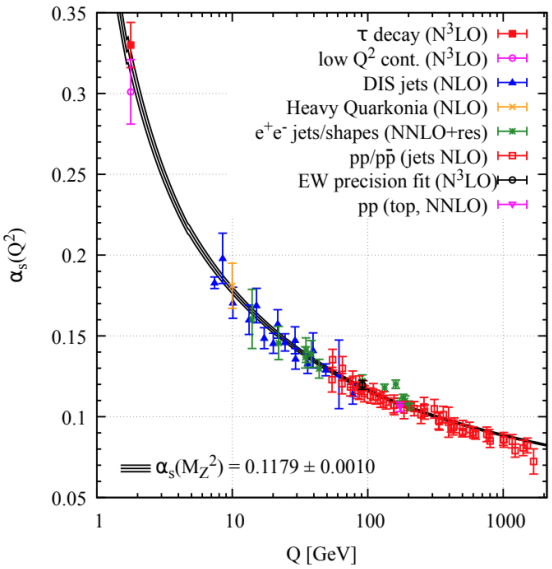

Figure 1.6. Summary of the measurements of α_s. At small distances (large energies) the *strong* interaction becomes *weak*. Figure from [20].

The main theoretical tool to map out the phase diagram consists in numerical simulations of QCD on a discretized space-time. Such lattice QCD calculations show that in the condition of no net baryon density, around the temperature $T_c \simeq 160\,\text{MeV}$, pressure and energy density increase steeply as a consequence of an increased number of degrees of freedom of the system. The change in the degrees of freedom reflects a state transition, and lattice QCD shows that in this regime the confinement-deconfinement transition is a crossover at critical temperature T_c (see left panel of figure 1.7 and [21]). The current understanding about the rest of the phase diagram is sketched in the right panel of the figure. A variety of models indicate a first order phase transition as a function of temperature at finite μ_B. According to this, one expects the phase transition line to end at a critical point, whose existence has not been proved experimentally yet [22]. In addition to the confined state region and the QGP at low density and high temperature, at large density a number of different phases have been conjectured. In particular, the so-called "colour superconducting" phase consists in a diquark condensate with specific excitation spectra and transport properties, in analogy to the formation of Cooper pairs in the ordinary superconductivity [23].

Where is it possible to find the QGP? The asymptotic freedom suggests two methods for the creation of the deconfined state. The first consists in heating the hadronic system above the critical temperature, the second consist in making the quark matter degenerate as a consequence of an high density, far above

the baryon number density of normal nuclear matter ($\simeq 0.16\,\mathrm{fm}^{-1}$) [24]. This means that one should expect the formation of the QGP in three different kind of places: (1) the early universe (at time $\simeq 10\,\mu$s after the Big Bang, with temperature greater than 10^{12} K, 200 MeV); (2) the center of compact stars (where the color superconducting phase is also supposed to exist); (3) at the Brookhaven or at CERN laboratories, where heavy ions are accelerated and collide into the RHIC or LHC accelerators, respectively. The particles colliding during these experiments do not contain antibaryons. Nevertheless, the higher the collision energy the more virtual quark-antiquark pairs can be created, so that the absolute magnitude of the baryon density becomes smaller at higher energies and so does the baryochemical potential. Consequently, nuclear collisions at different energy can investigate different regions of the QCD phase diagram (see figure 1.9). The maximum energy reached at the LHC makes the baryon density approach zero and the energy density high enough to exceed the critical temperature. The evolution of the system formed during such collisions is sketched in the following paragraph.

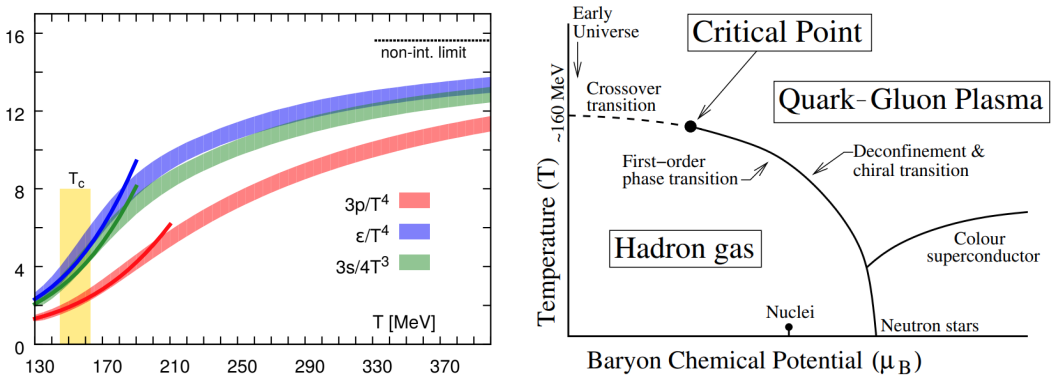

Figure 1.7. **Left:** Lattice QCD calculations at $\mu_B = 0$ showing the crossover regime around the critical temperature. The pressure, energy and entropy densities growth reflect an increase in the number of degrees of freedom of the system, which passes from a hadron gas to the deconfined quark and gluons plasma. Image adapted from [21]. **Right:** QCD phase diagram [22].

1.3.1 The Little Bang

The stopping power of two colliding nuclei strongly depends on the energy. At high energy the colliding ions are highly transparent and can create for a very short period ($\sim \mathcal{O}(10\ \mathrm{fm}/c)$) a strongly interacting medium with very high temperature and vanishing baryon density. Such "fireball" rapidly cools down and only the cold produced particles (hadrons and leptons) can be measured. The

space-time evolution of the system is pictured in figure 1.8, based on the description given by Bjorken [25].

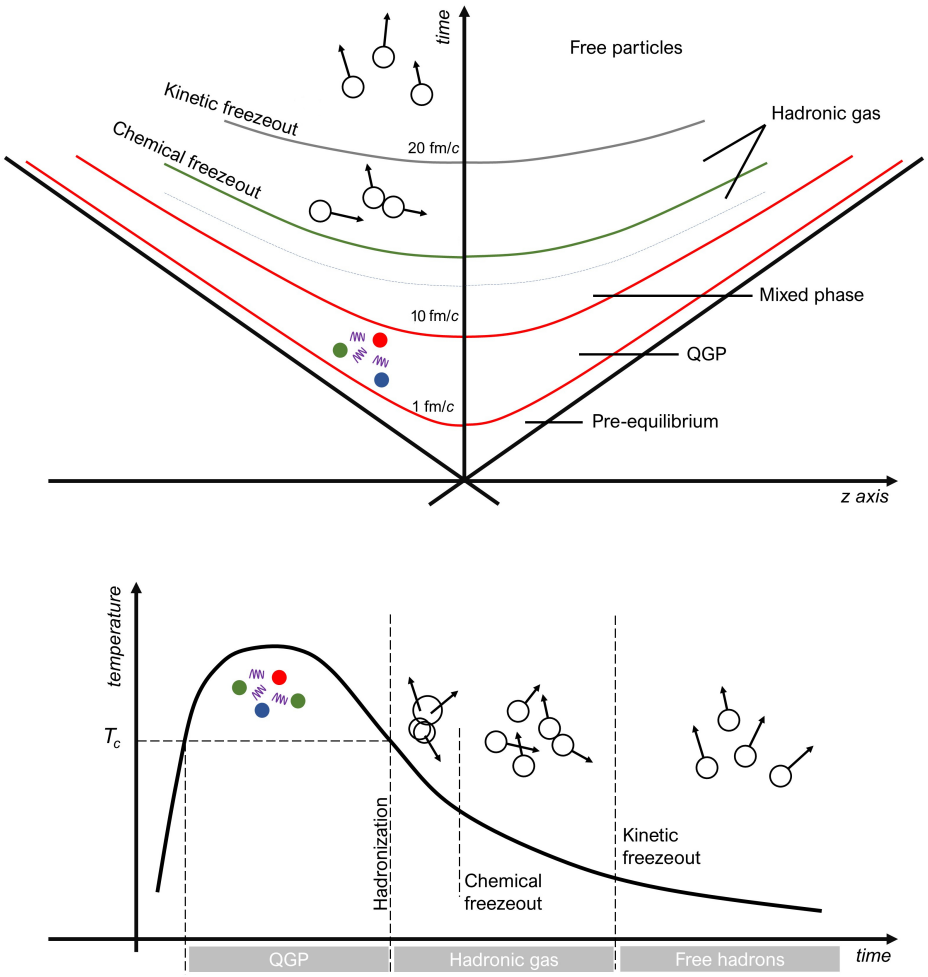

Figure 1.8. Qualitative longitudinal expansion of the fireball, from the interaction to the hadronization and kinetic freezeout.

The main steps of the evolution are qualitatively described in the following ([26] and references therein) in terms of the proper time $\tau = \sqrt{t^2 - z^2}$ which is Lorentz-invariant and parameterizes the hyperbolic curves shown in the figure.

- At $\tau = 0$ the nuclei collide. In the laboratory frame, they are two Lorentz-contracted disks with ratio between the transverse and the longitudinal di-

mensions given by $\gamma = \sqrt{s_{\mathrm{NN}}}/2m_{\mathrm{N}}$ (in case of symmetric collisions). They are mainly composed by gluons which carry a small fraction of the total longitudinal momentum ($x \ll 1$). The hard processes involving large momentum transfer between partons ($Q^2 \gtrsim (10\,\mathrm{GeV}/c)^2$) occur first, in a typical time given by $1/Q^2$. Particles produced by hard processes are important because they experience the whole evolution of the system and can be modified (mainly quenched and suppressed) according to the QGP internal dynamics. Hard probes include hadronic jets, direct photons, dilepton pairs, heavy quarks and electroweak bosons.

- Around $\tau = 0.2\,\mathrm{fm}/c$, the partonic constituents of the colliding nuclei are freed. Most of the hadrons measured by the detector are produced via the fragmentation and the hadronization of the gluons liberated at this stage. The non-equilibrium state of such medium, whose energy density in Pb-Pb collisions at the LHC is estimated to be $\gtrsim 15\,\mathrm{GeV}/\mathrm{fm}^3$, is known as "glasma".

- At $\tau \simeq 1\,\mathrm{fm}/c$ the strong interaction is able to redistribute energy and momentum among the partons in spite of their fast expansion and the medium approaches the thermal equilibrium. We are in the QGP phase. The equilibrium is actually reached only locally, since temperature is space and time dependent.

- The system starts to cool down. Hadronization occurs when the temperature becomes of the order of the critical temperature ($\simeq$ 160 Mev). At the LHC energy this is estimated to happen around $\tau = 10\,\mathrm{fm}/c$. At this point the system is still dense to the point that a thermal equilibrium of the created hadron gas is not possible. Hadrons still collide through inelastic collisions and the hadronic composition changes. This happens until the **chemical freezeout**. From that point on, the relative abundance of hadrons is fixed and no more inelastic collisions take place. The properties of the medium at this stage as achieved in different experiments and different collision energy are shown in figure 1.9 [27].

- Around $\tau \simeq 20\,\mathrm{fm}/c$ also the elastic collisions stop. The system changes finally from a fluid state to a system of free particles which stream freely towards the detector. This is known as **kinetic freezeout**. The momenta of the formed particles are set.

Many observables and many experimental signatures of the QGP formation exist. They rely on the comparison between what is measured in ion collisions and a reference measured where the formation of the hot medium is not expected

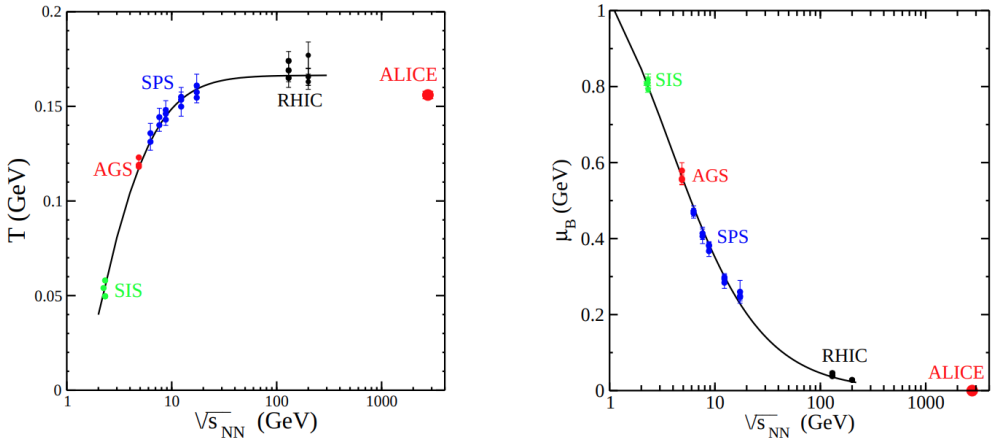

Figure 1.9. Temperature and baryochemical potential at the chemical freezeout as a function of the beam energy, extracted from particle yields using thermal-statistical models. From [27].

(proton-proton or proton-lead collisions). The strangeness enhancement is the first signature proposed as a hint of the QGP formation [28] and has been measured both at RHIC [29] and LHC [30] energies.[4] In any case one should consider that the nuclear environment affects the initial state of the collision independently on the subsequent formation of the hot medium. Such "cold" effects are presented in section 1.4. Once they are under control, the final states observables provide information on the hadronic and QGP phases. They include the modification of the p_T spectra, the relative yield of different hadron species, anisotropy in the particle flow, particle correlations, event-by-event fluctuations, hadronic hard probes (heavy flavour, jets) suppression and quenching [31]. A discussion related to the ALICE results is given at the end of chapter 2.

1.4 Nuclear Parton Distribution Functions

1.4.1 Cold nuclear matter effects

Observables which serve as QGP signature have to show a different behavior when measured in collisions where the QGP formation is not expected. The typical reference are proton-proton (pp) collisions, which LHC can provide at the

[4]The enhancement is with respect to proton-proton collisions, once the yield is normalized by the number of participant nucleons. It is explained as a reduced energy threshold for the $s\bar{s}$ production in the QGP because of the restoration of the chiral symmetry after the deconfinement, which reduces the bare quark mass (let's recall that the thermalization temperature of the QGP is greater than the strange quark mass, so that thermal excitation can actually excite that degree of freedom).

same nucleon-nucleon collision energy probed during ion collisions. The pp results are then scaled with the Glauber Model as if the nucleus-nucleus collision would act as a sum of independent nucleon-nucleon collisions.[5] Collective effects caused by the hot QCD matter would for sure deviate from this scaling. Nevertheless this is not the only case. **Nuclear effects exist even without the presence of the hot medium**. They are called "cold nuclear matter effects", and having them under control is essential to well interpret the complex evolution of the heavy ion collision systems. Some of them affect all the physics processes, while others are related to particular observables.

Isospin effect. This is the most trivial effect. When describing the behavior of partons with different flavour inside the nucleus a combination of protons and neutrons has to be used since the u/d quark content in such nucleons is different. This reflects on the building of nuclear parton distribution function, even if some theoretical works assume isospin/flavour symmetries (see for example table 1.2).

Shadowing and antishadowing of PDFs. The measurement of the nuclear modification to the Parton Distribution Functions (PDFs) is one of the goals of the work presented in chapter 3. The following section, 1.4.2, is dedicated to the description of this nuclear effect.

Cold matter energy loss. Partons propagating in cold nuclear matter suffer multiple scattering and lose energy by gluon emission. The production cross section of a given hard process in nuclear collisions can be suppressed because of this mechanism which can be considered as a shift in the momentum fraction x at the PDFs level [33]. As proposed by some authors, this effect should involve a coherent medium-induced radiation from many partons and between the initial and final state of the process [34].

Saturation effects. Another effect proposed as an intrinsic property of all high-energy strongly interacting collisions is a collective effect of the gluon wave-functions known as Color Glass Condensate. It deals with the non-perturbative behavior of the gluon density which becomes very large in the low-x kinematic region, as shown also in figure 1.10. This is treated by means of weak coupling effective theories [35].

[5] Since the phase transition to QGP requires a certain volume at high energy density, also proton-nucleus and peripheral nucleus-nucleus collisions are experimental handles for the investigation of hadron gas/non-QGP phase. On a side note, we also underline that it has been suggested how ultra high energy pp collisions could produce a system with properties similar to the QGP [32], even if no conclusive evidence has been measured yet.

Nuclear absorption. An effect of nuclear absorption may be considered when quarkonia states ($q\bar{q}$ pairs) propagate through the nuclear matter and is broken by inelastic collisions with the nucleons. This effect is particularly sizable in the case of a resonance time formation which is smaller than the collision time $2R/\gamma c$ (with R the nucleus radius and $\gamma = \sqrt{s_{\rm NN}}/2m_N$ the Lorentz factor)[6] [36].

1.4.2 PDFs and their nuclear modification

The Parton Distribution Functions (PDFs) are the probability density functions of the kinematic distribution of partons (quarks and gluons) inside an hadron. We are actually focused on the collinear PDFs, which do not contain a parameterization of the transverse momentum of the parton. For a given flavour or gluon i, the parton distribution f_i is a function of its longitudinal momentum and of the energy scale Q of the process involving the parton. The momentum is expressed as the fraction x of the momentum of the parent hadron carried by the parton: $f_i = f_i(x, Q^2)$. PDFs are defined in the context of the factorization theorem which states that the cross section for a hard process producing the final state H during the collision between hadrons A and B can be expressed as a sum (convolution) of elementary hard processes cross sections between partons, weighted on the PDFs [37]:

$$d\sigma^{AB\to H+X} = \int dx_1\, dx_2 \sum_{i,j} f_i^A(x_1, Q^2)\, d\sigma^{ij\to H+X}(x_1, x_2)\, f_j^B(x_2, Q^2) + \mathcal{O}(1/Q^2) \tag{1.4.1}$$

The elementary cross sections can be calculated perturbatively in QCD, while the PDFs contain the non-perturbative process-independent part of the calculation. The PDFs are generally extracted from global fits to different experimental data. They are usually parameterized at low scale $Q^2 \sim 1 - 2\,\mathrm{GeV}^2$ then evolved up to the relevant scale thanks to the DGLAP equations [38–40], [41]. Most of the data constraining the proton PDFs comes from Deep Inelastic Scattering (DIS) experiments. A generic form of the parameterization is

$$x\, f_i(x, Q^2) = A_i\, x^{a_i}\, (1-x)^{b_i}\, I_i(x)$$

where I_i is a smoothly varying function (usually a polynomial in $\sqrt{x}$), the x^{a_i} term dominates at low x and $(1-x)^{b_i}$ ensures that the PDF vanishes in the elastic limit $x = 1$. More details on this and a review of the available nucleon PDF sets can be found in [41]. The analysis performed by the CTEQ-TEA group, and in

[6] Let's consider for example J/ψ production ($c\bar{c}$ state): the formation time ranges from 0.5 to 1.2 fm/c [20], while at $\sqrt{s_{\rm NN}} = 5.02$ TeV the collision time is much smaller, below $5 \cdot 10^{-3}$ fm/c.

particular the CT14 PDF set [42], will be systematically used as a reference for the results presented in chapter 3. CT14 is the first analysis of the group including LHC measurements of production of vector bosons and jets, at 7 and 8 TeV. An example of its prediction at the NNLO precision is reported in figure 1.10. It is well known that at high x, where the proton momentum is shared by only few partons, the presence of two u and one d valence quarks is enhanced. At low x the sea (virtual) quarks emerge and the gluon contribution becomes important.

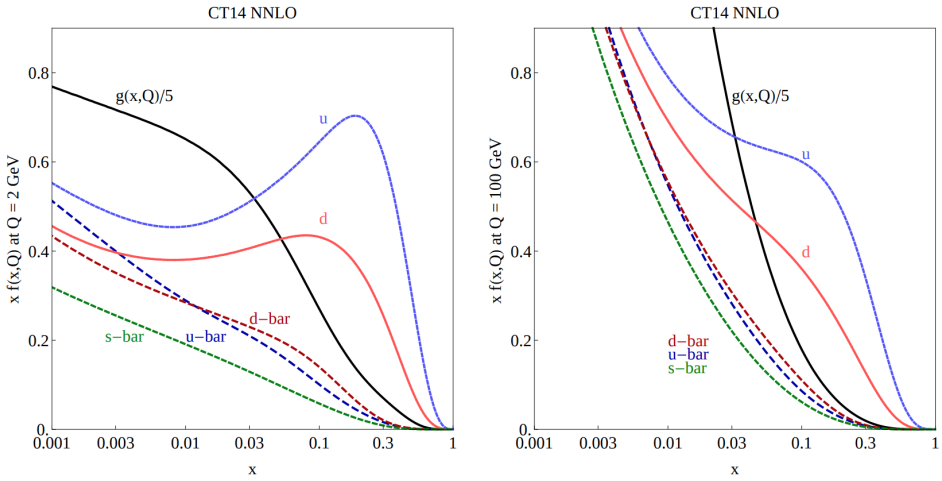

Figure 1.10. Distribution of light quarks and gluons in the proton according to CT14 analysis [42]. The plot on the right is at an energy scale close to the Z boson mass.

Nuclear modification

An analysis on deep inelastic scattering of muons over iron and deuterium published by the European Muon Collaboration in 1983 showed for the first time that the nucleon structure functions were different in the two nuclei [43], leading to the conclusion that the nuclear environment modifies the parton distributions. Although a consistent theoretical framework capable of describing these nuclear structure effects is still missing, several groups up to now attempted a phenomenological parameterization of the nuclear Parton Distribution Functions (nPDFs) (the first fit was EKS98 [44]). The discrepancy between free-nucleon and nuclear PDFs for a given flavour or gluon in a given nucleus A is parameterized by factorizing a free-nucleon PDF baseline and a nuclear modification factor R:

$$f_i^A(x, Q^2) = R_i^A(x, Q^2)\, f_i^{\text{nucleon}}(x, Q^2) \tag{1.4.2}$$

The typical behavior of R is the one reported in figure 1.11. Considering that $R = 1$ means no nuclear modification, four different regions can be identified in the x spectrum. The interval quoted in the following are approximated, our knowledge on their values depending on the parton flavour, the nPDF parameterization and the Q^2 value.

- **Shadowing.** A depletion in the PDF is observed at low x, up to $x \lesssim 3 \cdot 10^{-2}$. In the small x region, gluon bremsstrahlung is dominant and follows a DGLAP evolution. But as we already mentioned, when approaching a very small x regime, the high-parton density effects accounted by the nPDF evolution in the collinear framework of perturbative QCD breaks down. In particular the gluon phase-space density in the finite nucleus volume could saturate to the point that the gluon density can no longer grow, resulting in a parton shadowing. The Color Glass Condensate approach tends to describe such high parton density [35].

- **Antishadowing.** The interaction and "fusion" of nucleons at low x leads to a decrease of the number density of low x partons. The enhancement foreseen in the $0.1 \lesssim x \lesssim 0.3$ region can therefore be interpreted as a consequence of the momentum conservation [45].

- **EMC effect.** We use this name to refer to the depletion region close to $0.3 \lesssim x \lesssim 0.8$. Different models have been developed to describe it. They almost all agree in describing it as a change of scale, could it be a rescaling in x or in Q^2. That has been suggested to come from the separation energy of the nucleon which causes the x variable to be modified, or from a clustering of more than three quarks in the nucleus with a consequent different momentum distribution, or again from other phenomena. A detailed review can be found in [46].

- **Fermi motion.** This term refers to the dynamics of nucleons inside the nucleus, which should be responsible for a steep increase in the nuclear factor in the limit $x \simeq 1$. The Fermi motion and EMC effects can also be described collectively by the so-called Cronin Effect, which produces an enhancement of the particle transverse momentum spectrum in proton-nucleus collisions with respect to proton-proton collisions: as a result of multiple scatterings the partons would acquire a transverse momentum kick, shifting their momenta from lower to higher values and causing the observed depletion (EMC effect) and enhancement (Fermi motion) [47].

Some of the contemporary nPDFs sets are listed in table 1.2, in particular the nCTEQ15 analysis [48] and the EPPS16 analysis [49] (which supersedes the older

EPS09, quoted in the table because it is at the base of the most recent impact-parameter dependent analysis, EPS09s, as will be described soon). Such theoretical works will be used in chapter 3 to discuss our experimental results.

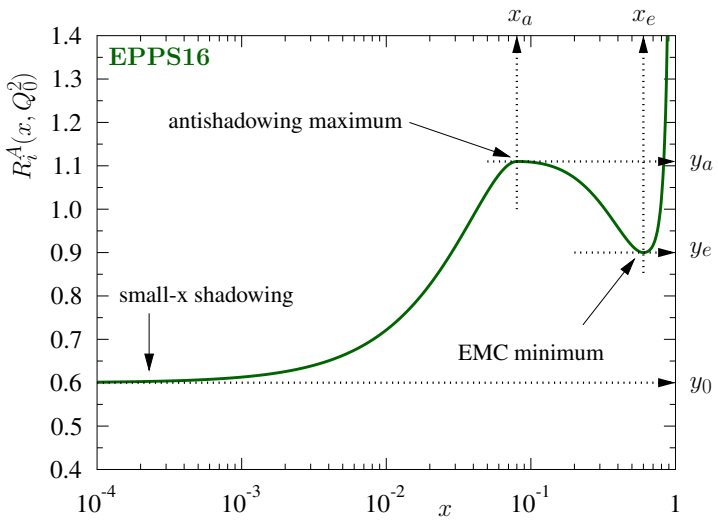

Figure 1.11. Schematic diagram of the typical nuclear modification factor to the PDFs as a function of x. The line is a possible output of the EPPS16 parameterization (see text) [49].

	EPS09 [50]	nCTEQ15 [48]	EPPS16 [49]
Experimental data included:			
DIS in l^-+A	✓	✓	✓
Drell-Yan in p+A	✓	✓	✓
RHIC pions d+Au	✓	✓	✓
ν-nucleus DIS			✓
Drell-Yan in π+A			✓
LHC p+Pb dijets			✓
LHC p+Pb electroweak			✓
Order in α_s	NLO	NLO	NLO
Number of datapoints	929	708	1811
Free parameters	15	16	20
Proton baseline	CTEQ6.1	CTEQ6m-like	CT14 NLO
Flavour separation		valence	valence + sea

Table 1.2. Features of some of the most recent nPDF analyses. See text for details. Adapted from [51].

Parameterizations

The nucleus is made of many protons and neutrons, which, as free particles, have a different quark content. Experimental data can constrain the nuclear PDFs without making this distinction. Nevertheless the effective neutron and proton nuclear PDFs $f_i^{A(n)}$, $f_i^{A(p)}$ are considered. Both nCTEQ and EPPS derive the bound neutron PDFs from the bound proton PDFs by isospin symmetry, i.e. exchanging the u and d quark distributions. From there, the nucleus PDFs are calculated:

$$f_i^A(x,Q^2) = \frac{Z}{A} f_i^{A(p)}(x,Q^2) + \frac{A-Z}{A} f_i^{A(n)}(x,Q^2) \tag{1.4.3}$$

In these analyses the nucleus is characterized only by its mass number A; one of the differences between nCTEQ and EPPS is the implementation of the dependence on A. While in EPPS the nuclear effect is added on top of a free proton PDF in the form of a modification factor, nCTEQ introduces an A dependence on the full nPDF parameterization. The functional form resembles the free proton CTEQ parameterization[7] with coefficients $c_k^A = c_{k,0} + c_{k,1}(1 - A^{-c_{k,2}})$ chosen such that for $A = 1$ one recovers an analysis based on CTEQ6 PDFs [52]. On the other hand, the EPPS16 parameterization is:

$$f_i^{A(p)}(x,Q^2) = R_i^A(x,Q^2)\, f_i^{\mathrm{CT14}}(x,Q^2)$$

where f_i^{CT14} are the CT14 NLO free proton PDFs. The free parameters are contained in the polynomial form of R_i^A and consist in the value for $x \to 0$ and the positions and amplitudes of the antishadowing maximum and EMC minimum.[8] This is shown in figure 1.11. The shadowing and antishadowing/EMC magnitudes contain the dependence on a power of A, in such a way that the effects are larger for heavier nuclei. For both nCTEQ and EPPS the number and momentum sum rules are required to hold:

$$\int_0^1 dx\, f_{u_V}^{A(p)}(x) = 2 \qquad \int_0^1 dx\, f_{d_V}^{A(p)}(x) = 1 \qquad \int_0^1 dx \sum_i x f_i^{A(p)}(x)\, dx = 1$$

[7] More precisely: $x f_i^A(x,Q_0) = c_0^A\, x^{c_1^A}(1-x)^{c_2^A} e^{c_3^A x}(1+e^{c_4^A}x)^{c_5^A}$, for each flavour or gluon i. The input scale chosen is $Q_0 = 1.3\,\mathrm{GeV}$.

[8] More precisely, the polynomial order is also fitted:

$$R_i^A(x,Q_0^2) = \begin{cases} a_0 + a_1(x-x_a)^2 & \text{if } x \le x_a \\ b_0 + b_1 x^\alpha + b_2 x^{2\alpha} + b_3 x^{3\alpha} & \text{if } x_a \le x \le x_e \\ c_0 + (c_1 - c_2 x)(1-x)^{-\beta} & \text{if } x_e \le x \le 1 \end{cases}$$

Datasets, flavour separation, results

The experimental data points and kinematic regions included in the nCTEQ and EPPS16 fits are summarized in table 1.2 and reported in figure 1.12, while an example of the resulting nuclear modification for different flavours and for gluons is in figure 1.13.

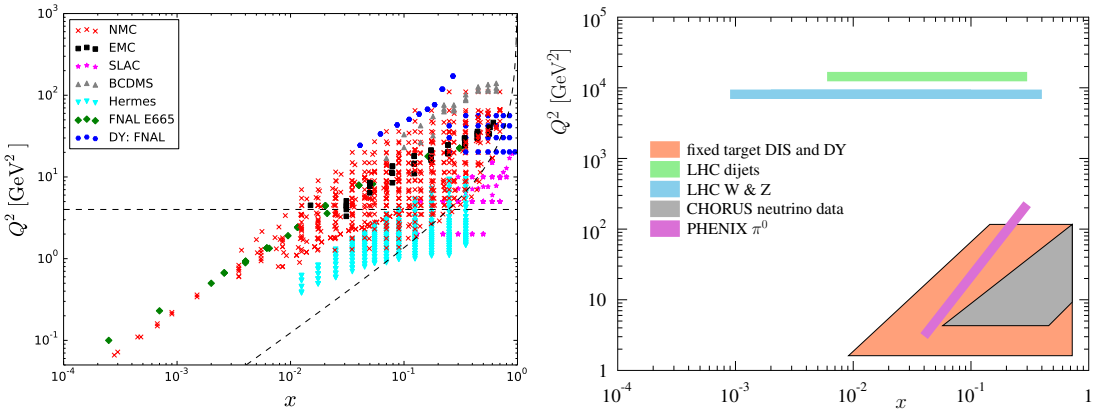

Figure 1.12. **Left:** Summary of the Deep Inelastic Scattering and Drell-Yan datapoints included in the nCTEQ15 fits. The dashed lines represent the cuts employed in the analysis (on Q and on the invariant mass of the final state hadronic system) [48]. **Right:** Kinematic regions at which different data included in the EPPS16 fit can constrain the nPDFs [49].

In both nCTEQ15 and EPPS16 the u and d valence quarks are independently parameterized, while this is not the case for EPS09. As one can see in figure 1.13, nCTEQ15 doesn't have big constraints on the difference between valence quarks, mostly because of the lack of neutrino-nucleus data. EPPS16 is the first fit implementing a parametric freedom of all u, d, s flavours and including data from DIS of neutrinos on ^{208}Pb (more that 800 datapoints from CHORUS [53]). The higher number of degrees of freedom of course implies larger uncertainties of the results, even if they are less biased. Particularly interesting is the inclusion of LHC (Run 1) data on dijets and electroweak boson production in the EPPS analysis. Dijets provide more constraints on the gluon nuclear modification: the reader can compare nCTEQ15 and EPPS16 error bands for the gluon distributions at high x in the figure. The best constraints on the strange quark come from the Z boson at the LHC, since $s\bar{s}$ scattering contributes for $\simeq$ 20% of the cross section production at midrapidity [51]. A total of 23 datapoints from ATLAS (Z boson [54]) and CMS (Z and W bosons [55, 56]) electroweak analyses of proton-lead collisions at $\sqrt{s_{\rm NN}} = 5.02$ TeV have been used.

The nCTEQ15 analysis was recently extended to study the impact of the LHC

W and Z production. A new nPDF set, called nCTEQ15WZ, was extracted after the inclusion of electroweak bosons data from proton-lead collisions recorded by ATLAS and CMS [57]. The improvement in fitting the LHC measurements (including $W^{\pm}$ results by ALICE in p-Pb at $\sqrt{s_{NN}} = 5.02$ TeV) is evident, as one can read in the quoted paper.

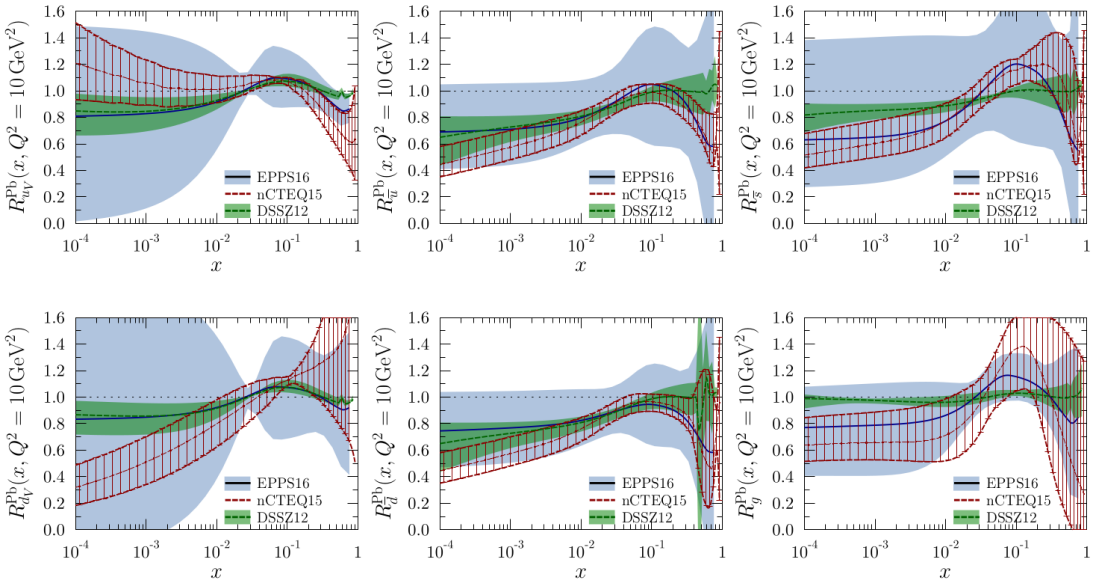

Figure 1.13. Nuclear modification as a function of x for the lead nucleus at $Q^2 = 10\,GeV^2$. nCTEQ and EPPS16 analyses are compared, together with DSSZ12 [58]. Images taken from [51].

EPS09s: impact parameter dependence

Up to now the spatial dependence inside the nucleus has been averaged by means of formula 1.4.3 which sums indistinctly over all the protons and all the neutrons. The EPS09s analysis [59] implements a dependence of the PDFs on the position inside the nucleus. Since such quantity implies a dependence of the cross sections on the centrality of the collision, the key variable in these calculations is the impact parameter b. As in the EPS and EPPS analyses, a free nucleon PDF baseline is used (CTEQ6 in this case) and the parameterization is done on the nuclear factor. This is supposed to depend on b, $r_i^A(x, Q^2, b)$, under the constraint that the spatial average

$$R_i^A(x, Q^2) = \frac{1}{A} \int d^2\vec{b}\, T_A(b)\, r_i^A(x, Q^2, b)$$

coincides with the one provided by the standard EPS09 fit. Further assumption on the spatial dependence is the shadowing mechanisms at small x. In this regime partons may interact with those belonging to other nucleons close enough in the transverse direction; following this idea r_i^A is supposed to be a function of the thickness $T_{\mathrm{A}}(b)$. This has the big advantage of simplifying the implementation of the A dependence, since it is fully contained in T_{A}. The formula is:

$$r_i^A(x, Q^2, b) = 1 + \sum_{j=1}^{n} c_{i,j}(x, Q^2)\ [T_{\mathrm{A}}(b)]^j$$

Very peripheral collisions ($b \to \infty$) are automatically treated as free nucleon collisions, since in this limit $r_i^A(b)$ tends to 1. The coefficients are then fitted minimizing the distance to the A-dependence predicted by EPS09.

In the quoted reference one can see that the EPS09s set well reproduces the nuclear modification factor R_{dAu} measured with π^0 production in deuterium collisions on gold nuclei in different centrality classes by the PHENIX experiment.

1.5 Nuclear shadowing with Z and W bosons: an up-to-date overview

Z and W electroweak vector bosons are useful probes for the investigation of the initial state nuclear effects, and in particular the modification of parton distributions. This is mainly because there are no other major effects that can influence their production. The cleanest way to study them is through their leptonic decay, since leptons don't interact strongly with the hadronic matter. At leading order the production is an electroweak process in which a quark-antiquark pair annihilates into a lepton pair. At higher orders gluon radiation must be accounted for, as shown in figure 1.14. In case of the neutral current Drell-Yan $q\bar{q} \to l^+l^-$ process, the gauge boson can be a Z boson or a photon. The resonant Z region is at $M_Z = 91.2\,\mathrm{GeV}/c^2$ and has a width of $2.5\,\mathrm{GeV}/c^2$ [20].

It is clear that such processes carry direct information on the distribution of the partons inside the colliding hadrons. Both vertexes of the diagram are described by electroweak interaction which is very well known theoretically and has been widely studied experimentally (refer to [60] for a review on Z boson LEP results). Moreover, the large mass (large $Q^2 \simeq M^2_{\mathrm{Z/W}}$) makes perturbative QCD calculations possible and up to now the Next-to-Next-to-Leading Order (NNLO) accuracy has been reached [61].

Concerning the interplay between Z and W production in heavy ion collision and the hot nuclear matter, we should first focus on the time scale of the relevant

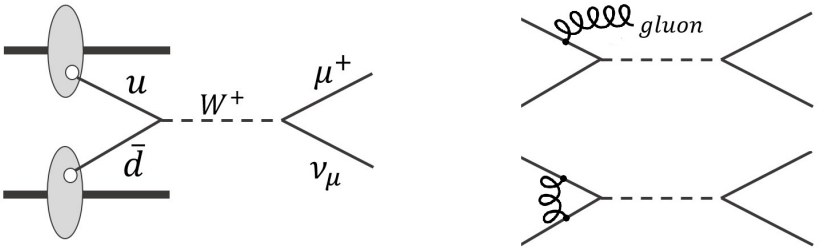

Figure 1.14. **Left:** Tree-Level Feynman diagram for W boson production via annihilation of u and $\bar{d}$ quarks and consequent muonic decay. **Right:** Feynman diagrams contributing at NLO QCD correction.

processes. The vector boson formation happens in a very short time, of the order of $[M_{Z/W}]^{-1} \simeq 10^{-3}\,\mathrm{fm}/c$. As described at page 21, this is much shorter than the typical time scale of the QGP formation. On the other hand, in the muonic decay channel the decay products experience the whole evolution of the system and even if an interaction via strong force is not possible, there are hints that muons undergo electromagnetic interactions with the medium. The signature is a broadening of the transverse momentum muon spectra even if recent works attributes it to photo-production in the initial electromagnetic field [62, 63]. In any case the amount of such modification is much smaller than the average transverse momentum carried by the muons which, for example, for the Z decay is of the order of $45\,\mathrm{GeV}/c$. We quote also the studies reported in [64] on the muon energy loss via elastic scattering with the charges of the medium: in a medium with temperature $\simeq 1\,\mathrm{GeV}$ only one elastic collision per muon is expected and this results in a negligible energy loss. Connected to the transparency of the hadronic matter to the Z boson production and detection, a recent precise measurement on the anisotropy of Z production in Pb-Pb collisions is reported in [65] and shown in figure 1.16. The displayed elliptic flow v_2 is defined as the mean value $\langle\cos[2(\phi_Z - \psi)]\rangle$ (ϕ_Z being the azimuthal angle of the emitted boson and ψ a common reference angle), namely the second term in the Fourier decomposition of the angular distribution of Z bosons. In case of interacting probes, the anisotropic distribution of the colliding matter is transferred to the observed momenta distributions. The quoted v_2 measurement is consistent with zero in different centrality classes; this corroborates the hypothesis that Z bosons are produced at the early stages of the collisions and are not affected by final state effects caused by hydrodynamic flow.

Table 1.3 summarizes the results from ATLAS, CMS, ALICE and LHCb on the production of electroweak bosons in heavy ion collisions. Such results provide a large amount of data points which can be included in the nPDF global fits. The measured yields or cross sections are compared to both free-nucleon and nuclear PDF calculations. Besides the presence of nuclear (anti)shadowing, the scaling with the number of binary collisions is also checked when the results are available as a function of centrality.

System $\sqrt{s_{NN}}$	ATLAS	CMS	LHCb	ALICE
p-Pb 5.02 TeV	[54] (Z)	[55] (Z), [56] (W)	[66] (Z)	[67] (Z,W)
p-Pb 8.16 TeV		[68] (W)		[69] (Z), p* (W)
Pb-Pb 2.76 TeV	[70] (Z), [71] (W)	[72] (Z), [73] (W)		
Pb-Pb 5.02 TeV	[74] (Z), [75] (W)	[65] (Z)		[69,76] (Z), p* (W)

Table 1.3. Available analyses on Z and $W^{\pm}$ production in heavy ion collisions. In the ALICE column, the symbol p* means that preliminary results are available and public. Corresponding plots can be found on ALICE web-page `https://alice-figure.web.cern.ch/` while a nice summary on those results is at the reference [77].

It is important to notice the difference in the kinematic regions accessible by ALICE/LHCb and ATLAS/CMS, sketched in figure 1.15. ATLAS and CMS provide combined measurements in the electronic and muonic decay channels, in the central rapidity region, up to a value of $|\eta| \simeq 2.5$ (or 3.5 as in [54]). On the contrary, ALICE can measure W and Z via their muonic decay in the muon spectrometer which is located in the forward region, with rapidity between 2.5 and 4. LHCb provided precise measurement also at larger rapidity in proton-proton collisions [78], while the Z analysis in p-Pb suffers from lack of statistics. Such different rapidity values cover complementary regions in the Bjorken-x spectrum of the involved partons. **ALICE is the only experiment providing results for Z and W bosons in the very low and very high x regions, where the nuclear PDFs are currently known with the highest uncertainty** because of the lack of experimental constraints. The smaller is x the higher is the contribution from virtual sea quarks and gluons. Data taken in such configuration are sensitive to heavier flavours such as strange and charm quarks which at the moment are poorly considered in the nPDFs parameterizations.

As a general comment on the LHC results, Z and W measurements are well

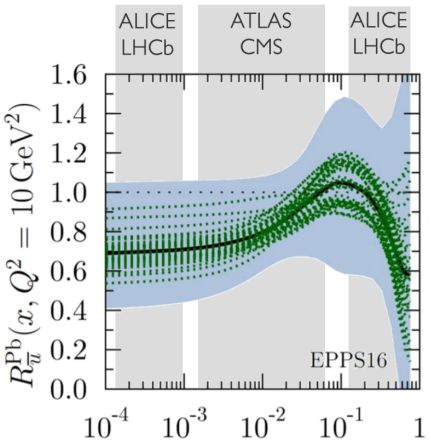

Figure 1.15. Qualitative x ranges probed by the LHC experiments, on top of a nuclear modification factor computed by EPPS16 [49]. See also page 89 and figure 3.26.

described at midrapidity by calculation both with and without the inclusion of nuclear modification to the PDFs. This can be explained at the light of figure 1.15 since at central rapidity the probed x values extend over the shadowing and antishadowing regions. This results in two competing effects which tend to cancel. Of course this is not a strict rule and exceptions are present. It is particularly significant the deviation from free-nucleon PDFs (CT14) predictions found by CMS with W production in p-Pb collisions at $\sqrt{s_{\mathrm{NN}}} = 8.16$ TeV [68], as shown in figure 1.17.[9] The main processes of $\mathrm{W}^{\pm}$ production are $u\bar{d} \to \mathrm{W}^{+}$ and $d\bar{u} \to \mathrm{W}^{-}$ annihilations respectively. The asymmetries of the separate yields of W^{+} and W^{-} is sensitive the u/d content ratio allowing a flavour decomposition of light quarks distributions in the nuclei. The lepton charge asymmetry $((N_l^+ - N_l^-)/(N_l^+ + N_l^-)$, where l means lepton) measured by CMS in p-Pb collisions at $\sqrt{s_{\mathrm{NN}}} = 5.02$ TeV [56] is shown in figure 1.18. At backward rapidity the results deviate from calculations. A possible physical origin of the tension is a different nuclear modification of u and d quarks. Indeed, the measurement is compared with EPS09 nPDFs which, as already said, don't implement flavour separation.

Electroweak bosons are like a standard candle also in probing the binary scaling of hard processes. An unexpected enhancement of the production towards peripheral collisions has been measured by ATLAS in Pb-Pb collisions at $\sqrt{s_{\mathrm{NN}}} = 5.02$ TeV , as shown in figure 1.19 [74, 75]. This suggested to the authors of [79] the idea of recalibrating the Glauber Model in terms of a changed

[9] In the ranking of the (published) larger nuclear modification on the PDFs measured with Z and W bosons, this is at the first place. At the second place there is probably the analysis presented in chapter 3.

nucleon-nucleon inelastic cross section, on which $\langle T_{AA} \rangle$ depends in a non-trivial way. According to this idea, σ_{inel}^{NN} should present a nuclear suppression because of the gluon shadowing and saturation phenomena at small x mentioned above. Disentangling these effects from a pure nuclear modification of the PDFs is not trivial and in any case no definitive conclusions are found in the literature at the moment.

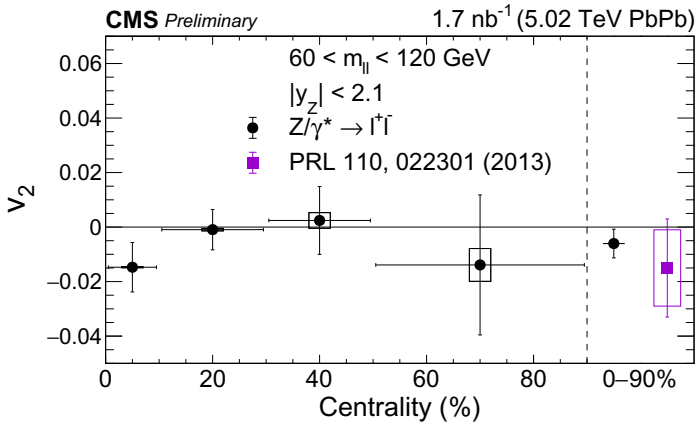

Figure 1.16. Centrality dependence of the Z boson elliptic flow v_2 measured by CMS in Pb-Pb collisions at $\sqrt{s_{NN}} = 5.02$ TeV [65]. No evident anysotropy is measured; the boson and its leptonic decay seem not to be affected by collective hydrodynamics effects of the hot medium.

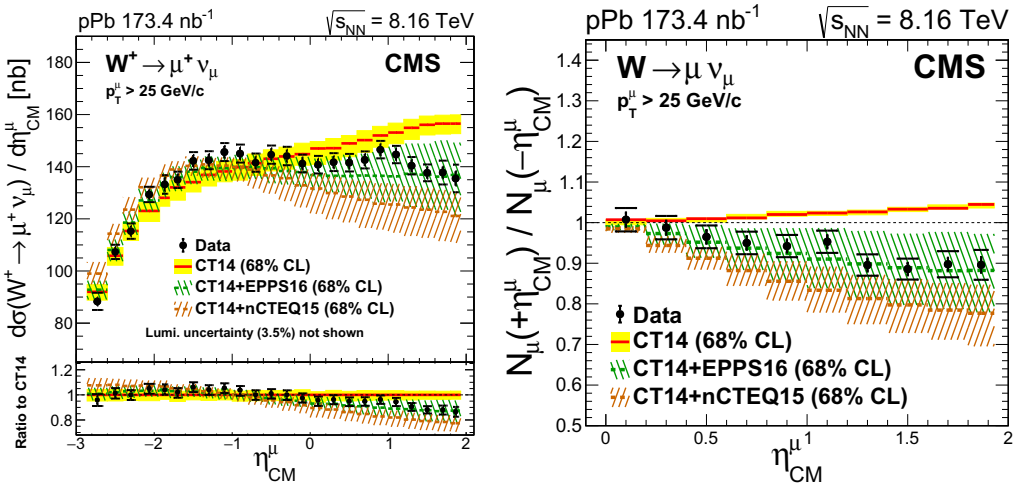

Figure 1.17. Cross section of $W^+ \to \mu^+ \nu_\mu$ production in p-Pb collision at $\sqrt{s_{NN}} = 8.16$ TeV and forward/backward asymmetry in the same data sample, measured by CMS. Results are compared with predictions from CT14 free PDFs and EPPS16, nCTEQ15 nPDFs. The significance of the suppression with respect CT14 has the p-value $2 \cdot 10^{-12}$ [68].

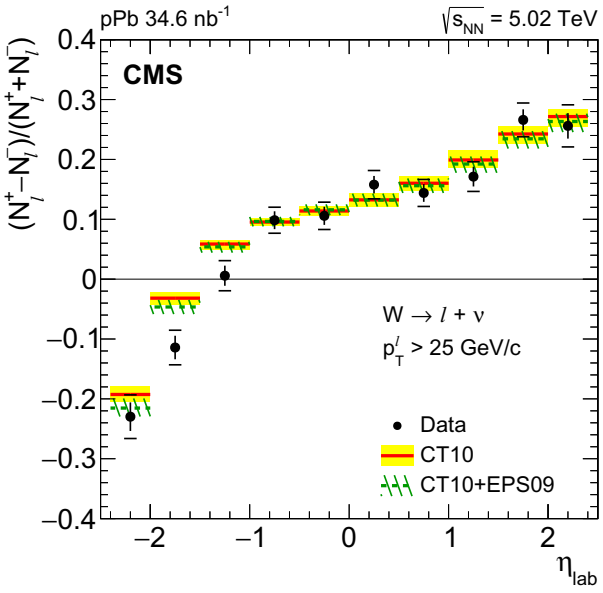

Figure 1.18. Charge asymmetry of muons coming from W boson decay, measured by CMS in p-Pb collisions at $\sqrt{s_{\rm NN}} = 5.02$ TeV [68]. The EPS09 calculations are not flavour-dependent; the deviation from data could be explained as a different nuclear modification of u and d quarks.

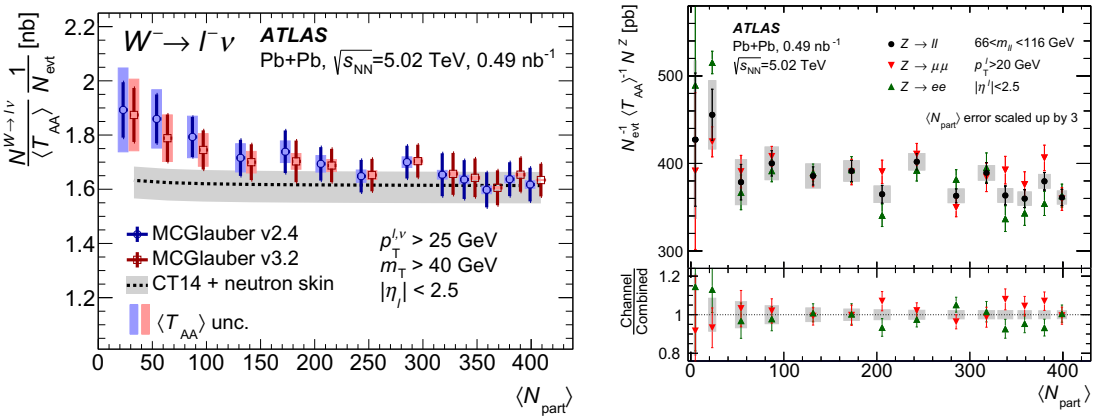

Figure 1.19. W^- (**left**, [75]) and Z (**right**, [74]) production yields normalized to the nuclear overlap function $\langle T_{\rm AA}\rangle$, measured as a function of centrality by ATLAS in Pb-Pb collisions at $\sqrt{s_{\rm NN}} = 5.02$ TeV . The attention should be focused on the enhancement towards more peripheral collisions (lower $\langle N_{\rm part}\rangle$). As shown in the papers, the measurements are also systematically above the corresponding EPPS16 predictions.

Chapter 2

The ALICE Experiment

ALICE (A Large Ion Collider Experiment) is one of the big general purpose experiments at the Large Hadron Collider. Presently in the Collaboration there are more than 1900 members from 39 countries. In this chapter the experimental apparatus will be outlined and the physics program of ALICE will be presented.

The detector is shown in figure 2.1. It is composed of 19 sub-detectors resulting in a very different overall optimization with respect to the other LHC experiments. The apparatus was designed to operate with a particle multiplicity up to $dN/d\eta = 4000$ (we now know that at the energy $\sqrt{s_{\mathrm{NN}}} = 5.02$ TeV it holds $dN/d\eta \simeq 2000$ in the most central collisions [80]). One of the main features of ALICE is its capability of tracking and identifying particles at central rapidity in a very wide range of transverse momentum, that allows studies from collective phenomena to jets' physics (few hundreds of GeV/c). Different particle identification (PID) techniques are used: energy loss measurements, time of flight measurements, Cherenkov and transition radiation, electromagnetic calorimetry and topological studies of particle decays [81]. The sub-detectors can be grouped as follows: (1) the central barrel, covering the central rapidity region and the full azimuth, with 0.5 T magnet field and where hadrons, electrons and photons are detected; (2) the muon spectrometer, covering the forward region (on a single side), dedicated to the detection of muons; (3) other global detectors, for the measurements of observables like the collision centrality, particle multiplicity or collision time. A detailed description of the apparatus can be found in [81].

The pseudorapidity covered by the different detectors is shown in figure 2.2. The ALICE coordinates system has the origin on the interaction point. The z axis is parallel to the beam pipe. Positive and negative z positions are identified as belonging to the A-side and C-side respectively. The axis is oriented such as the muon spectrometer is on the C-side. The x axis points to the center of LHC and the y axis is vertical.

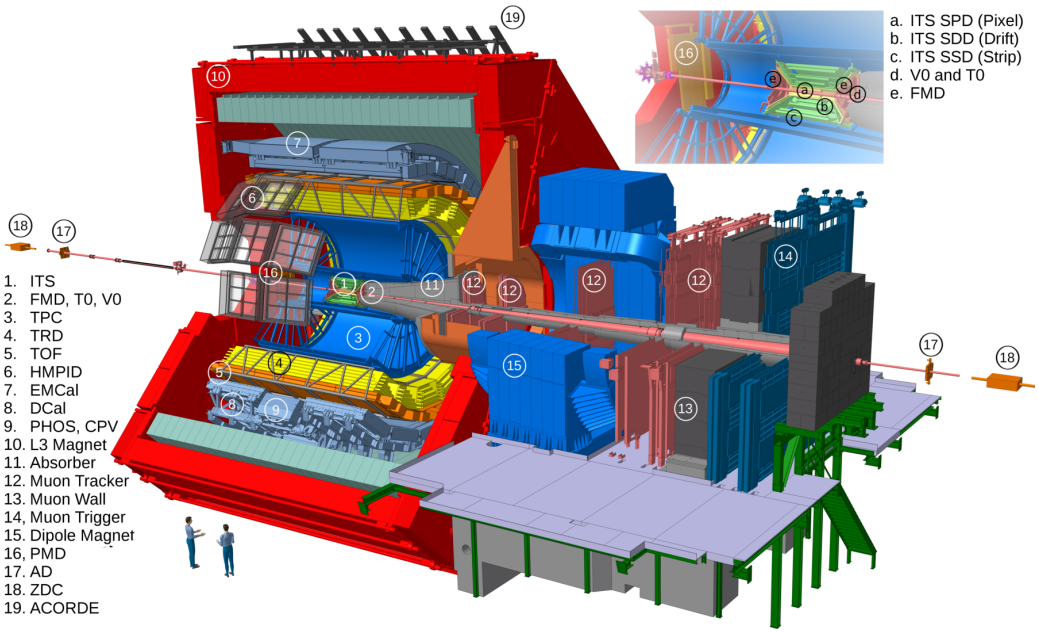

Figure 2.1. The ALICE Detector during LHC Run 2. In the top-right panel, the details of the Inner Tracking System.

Some details on the apparatus are given in the following. Notice that during the ongoing Long LHC Shutdown many detectors undergo a major upgrade and some of them, for instance the inner tracker layers, are being completely replaced. We will talk about this in appendix A. The ALICE setup up to the end of 2018, used to collect the data analyzed in chapter 3, is described in the following.

2.1 Central barrel

The central barrel is embedded in a large solenoidal magnet originally built for the L3 experiment at the LEP accelerator. It provides a relatively low magnetic field (max 0.5 T), designed to be a compromise between a sufficient bending of the tracks and the possibility for low momentum tracks to reach the most external layers of the detector.

The detector closest to the beam line is the **Inner Tracking System (ITS)**, made of six cylindrical layers with radii from 3.9 to 44 cm. Three different silicon technologies are exploited: Silicon Pixel Detector (SPD, for the first and second layers), Silicon Drift Detectors (SDD, third and fourth layers) and double-sided Silicon Strip Detectors (SSD, two outermost layers). A surface of 7 m^2 consisting of almost 13 millions of electronic channels is covered by the full ITS [83]. Neverthe-

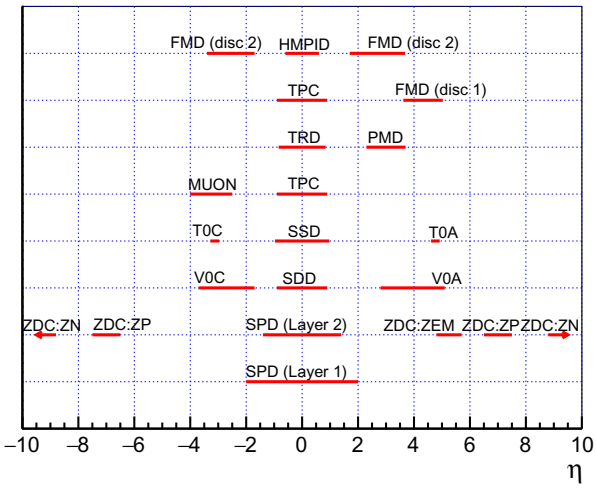

Figure 2.2. Pseudorapidity coverage of the ALICE sub-detectors. Image taken from [82].

less the material budget is very limited, ranging from from 0.83% to 1.26% of the radiation length X_0 per layer. The ITS locates the primary and secondary vertices with a precision of few tens of microns and measures energy loss contributing to the particle identification of low energy particles (in contrast to the SPD, the four outer layers have analogue readout). The number of clusters measured in the SPD can also be used for multiplicity determination, making the ITS detector a centrality estimator [84].

The main tracking detector of ALICE is the **Time-Projection Chamber (TPC)**. It is 5 meters long and 5.6 meters in diameter, the largest TPC in the world. It was originally filled with a $Ne/CO_2/N_2$ gas mixture [85], then changed to Ar/CO_2 to improve the stability of the readout chambers. An electrode at $z = 0$ divides the chamber in two sides, each of them equipped with 18 sectors of multi-wire proportional chambers (MWPC) mounted on the end plate. The ionization produced in the chamber may generate a field comparable with the one used for drifting. To avoid this, the number of tracks crossing the TPC and consequently the interaction rate had to be limited to a value which matches the 2.7 cm/s drift velocity. In spite of its slow recording speed and its huge data volume, the TPC fulfills the need of an efficient and robust device ensuring high performance even with tens of thousands of charged particles. It is responsible for particle identification and vertex determination and it is optimized for track finding and particle dE/dx measurements. It can detect particles of transverse momentum in a range from $\simeq 150\,\mathrm{MeV}/c$ to hundreds of GeV/c .

Around the TPC, from 2.9 m to 3.7 m to the beam pipe, there is the **Transition-Radiation Detector (TRD)**. It consists of six layers made of foam/fibre radiator followed by MWPC filled with a mixture of Xe/CO_2. Transition radiation occurs when a particle crosses the boundary between two media with different dielectric constant. The probability of photon emission is proportional to the Lorentz factor γ. In the TRD electrons can be distinguished from other charged particles (typically, pions) by producing such radiation and having a higher dE/dx. Thanks to a fast readout, the TRD is also used to trigger electrons with high transverse momenta and jets. During Run 3, with a higher interaction rate, the TRD will be a key element to correct for the space distortions expected in the TPC [86].

The **High-Momentum Particle Identification Detector (HMPID)** exploits the Cherenkov radiation. It consists of a single-arm 10 m^2 array of ring imaging Cherenkov (RICH) counters with liquid C_6F_{14} radiator whose radiation is detected by MWPCs. It covers about 10% of the inner barrel solid angle and extends particle identification capabilities toward higher momenta in this region, allowing separation of pions, kaons and protons up to 5 GeV/c .

Charge particle identification at intermediate momenta is the main task of the **Time-Of-Flight Detector (TOF)**, made of Multigap Resistive Plate Chambers (MRPC) arranged in sectors covering the full azimuth. It allows separation of electrons from kaons, pions and protons in the region where the energy loss measurements of TPC and TRD are not efficient ($E/m \lesssim 6$). Thanks to the fast response (time resolution $\simeq$ 40 ps), TOF can provide more than 3σ separation of K/p up to 4 GeV/c and of π/K up to 2.5 GeV/c [87].

ALICE has two electromagnetic calorimeters. The first is the **Photon Spectrometer (PHOS)**. It covers a limited section of the barrel acceptance and is made of $PbWO_4$ crystals. It measures photons spanning from low (thermal emissions) to high p_T (hard QCD processes). A set of multiwire chambers (CPV) in front of PHOS helps to discriminate between charged and neutral particles. The second is the **ElectroMagnetic Calorimeter (EMCal)**, a Pb-scintillator sampling calorimeter installed in 2010 to enhance the capability of measuring jet properties. Similarly to PHOS, it measures photons and neutral mesons but it is optimized to measure jet production rates (up to $p_T \simeq 150\,\mathrm{GeV}/c$) in conjunction with the charged particle tracking of the other detectors. This was improved after Run 1 with the installation of the **Di-jet Calorimeter (DCAL)** which together with EMCal forms now a double-arm system in the rapidity region $|\eta| < 0.70$ [88].

The **ALICE Cosmic Ray Detector (ACORDE)** is an array of 60 plastic scintillators on top of the L3 magnet which triggers on cosmic rays for calibration and alignment purposes.

2.2 Forward detectors

Some small and specialized detectors are used for event selection, triggering and to measure global observables. The **Zero Degree Calorimeter (ZDC)** consists of two sets of very compact hadronic calorimeters (ZN, made of tungsten-quartz, and ZP, made of brass with quartz fibers) and electromagnetic calorimeters (ZEM) placed at $z = \pm 116$ and $z = \pm 7$ m respectively. Neutrons and protons not involved in the collisions (spectators) are separated by the magnetic elements of the LHC beam line and deposit energy in ZN or ZP. As explained in the previous chapter, the particle multiplicity can be linked to the impact parameter to measure the centrality of the collisions. In very peripheral collisions a significant number of spectators stay in the beam pipe, being bound into fragments having a charge-to-mass ratio similar to the one of Pb. In such cases low energy is released into the hadronic ZDCs, similarly to what happens in very central collisions. ZEM helps to distinguish between the two cases measuring the energy of photons from π^0 emitted forward, which increases monotonically with the collision centrality.

The **Photon Multiplicity Detector (PMD)** and the **Forward Multiplicity Detector (FMD)** are dedicated to the measurement of event multiplicities around $\eta \simeq 3$. PMD measures the multiplicity and spatial distribution of photons. Its sensitive element is a large array of gas proportional counters in a honeycomb cellular structure. It detects signal coming from a three-radiation-lengths lead converter. The FMD provides charged-particle multiplicity over an extended region down to very small angles. The particles are counted in rings of silicon strip detectors located at three different positions on the beam pipe [83]. The SPD and the FMD complete each other in terms of pseudorapidity coverage and can provide multiplicity measurements in the full region $-3.4 < \eta < 5.1$.

The collision time is measured by the **T0** detector made of two sets of 12 Cherenkov counters with quartz radiators, mounted around the beam pipe and achieving a time resolution of ~ 20 ps. T0 serves as a minimum bias trigger [17].

The **V0** detectors have already been mentioned in section 1.2.3 since they are used for the centrality estimation. They consist of two arrays of scintillator counters located at $z = 330$ cm and $z = -90$ cm (V0-A and V0-C). Both of them are segmented into 32 individual counters connected via optical fibers to photomultipliers. V0 allows beam-gas background rejection thanks to the time difference between the A and C sides, with a time resolution of 1 ns [17]. Thanks to this and to the multiplicity measurement capability, it serves as minimum bias trigger as well as centrality trigger in Pb-Pb collisions.

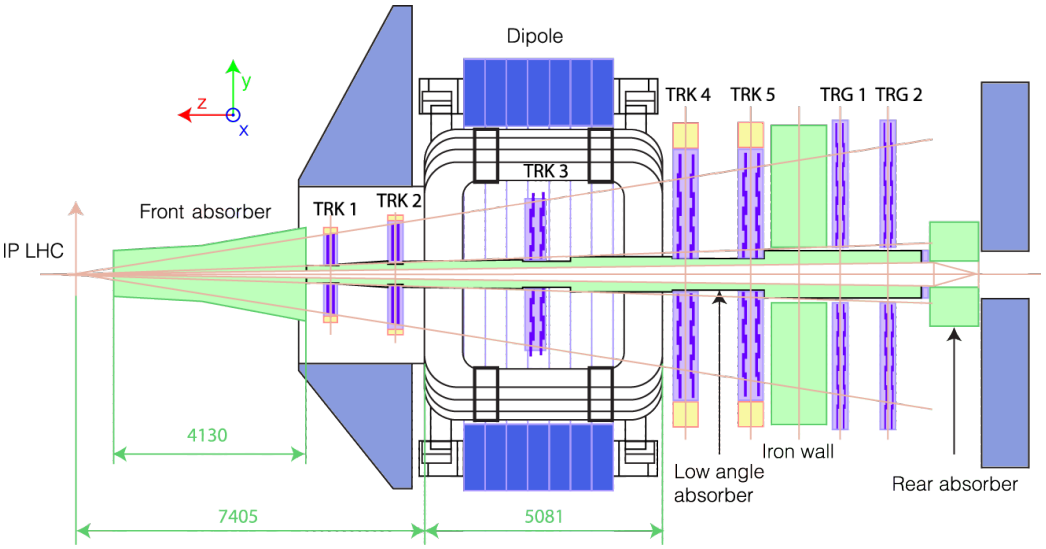

Figure 2.3. The ALICE muon spectrometer. Distances are in millimeters. Image taken from [82].

2.3 The muon spectrometer

A layout of the muon arm is shown in figure 2.3. It was designed to measure the spectra of light vector resonances (ρ, ϕ, ω) or heavy quarkonia states, J/ψ, Y, Y′, Y″ decaying into $\mu^+\mu^-$ as well as high- p_{T} muons coming from vector bosons decay [89]. The muon continuum at LHC energies is dominated by muons from semi-leptonic decay of open charm and beauty, so that it is also possible to perform heavy flavour analyses with the spectrometer. The detector is located only on the C-side, covering the full azimuth and the rapidity region $-4 < \eta < -2.5$. It consists of: (1) an absorbing system in front of the detection elements, (2) ten planes of tracking chambers, (3) a dipole magnet containing two of the chambers and (4) four planes of trigger chambers place beyond an iron wall. Few details on each of them are given below.

2.3.1 The front absorber

The absorber placed in front of the tracking chambers is shown in figure 2.4 in greater detail. It is inside the L3 magnet and is 4 meters long for a total of ~ 10 interaction lengths. It has the crucial role of reducing background from pions and kaons decay in the tracking chambers.

The core is made of carbon, concrete and, at the end part, lead and tungsten. Low Z materials help limiting the multiple Coulomb scattering, while the high

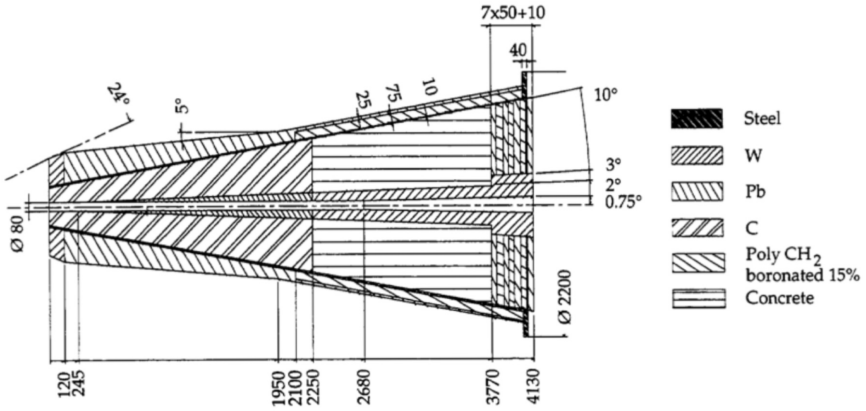

Figure 2.4. The different materials of the front absorber.

Z part absorbs particle showers and secondary particles produced inside the absorber, as well as low energy photons and neutrons. An inner shield surrounds the beam pipe and is made of lead and tungsten to protect from beam particles. Finally, an outer shield protects the central barrel detectors from the absorber recoiling particles.

2.3.2 Tracking stations and the dipole magnet

The tracking system consists of five stations, each of them made by two multiwire proportional chambers (MWPC). The third station, at almost 10 meters from the interaction point, is inside a dipole magnet which allows the tracks bending necessary for the determination of their momenta. The warm dipole is 5 m long and provides a magnetic field almost parallel to the x direction. The total integral field is 3 Tm.

The MWPCs are filled with an Ar/CO_2 mixture and are equipped with readout cathode pads on both planes. The central wires are parallel to the y axis and work at the nominal voltage of 1600 V. The first two stations have to endure higher density particles flux and have an higher granularity (the pad size goes from $4 \times 6.4\,mm^2$ to $5 \times 30\,mm^2$). The readout capability and the granularity of the spectrometer allows a $\simeq 40\,\mu$m position resolution. The information from the cathodes on each chamber provides the x-y hit position, while the z coordinate is given by the chamber position. The chamber material budget is as small as $0.03\,X_0$ to minimize multiple scattering.

2.3.3 The muon trigger system

Two trigger stations are composed by two planes each of 18 single gap Resistive Plate Chambers (RPC). They are used to reduce the probability of triggering on events where there are no interesting muon candidates from quarkonia, heavy-flavour, electroweak bosons, as previously mentioned. They are protected by a 1.2 meters iron muon filter placed behind the last tracking station with the purpose of reducing further the hadronic background and the contamination of secondary particles traversing the front absorber.

The RPC layout is shown in figure 2.5. They are made of two low-resistivity Bakelite electrodes, a gas gap, two graphite layers for the high voltage supply and two planes of segmented readout strips with pitch and length increasing with their distance from the beam. The time resolution is about $1 - 2$ ns and the spatial resolution is better than 1 cm, allowing a proper trigger strategy implementation based on particles transverse momentum. This is described in the following.

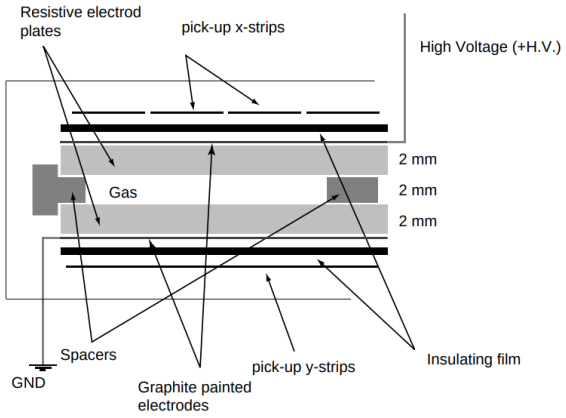

Figure 2.5. Cross section of the RPCs used for the trigger system. Image from [81].

2.3.4 Track reconstruction and trigger decision

The coordinates reconstruction is based on the charge induced on the pads of the multi-wire tracking chambers. The cluster-finding algorithm extracts the coordinates of a given cluster of fired pads by fitting the charge distribution with a two-dimensional Mathieson function [90]. In case of several close particles the number of candidates can be estimated as the number of local maxima in the distribution. Such simple method is not sufficiently accurate in case of significant overlapping of signal and background. In this case a Bayesian unfolding technique is used. An array of pixels is built in the anode plane with size defined by

the overlap of the pads on both cathodes. The intensity of the pixels (released energy) is then computed by iteratively solving the problem of a distribution deconvolution: at each step the pixels intensities are updated by finding the best agreement with the measured signal on the pads. The pixel-to-pad coupling is still given by a Mathieson integral [91].

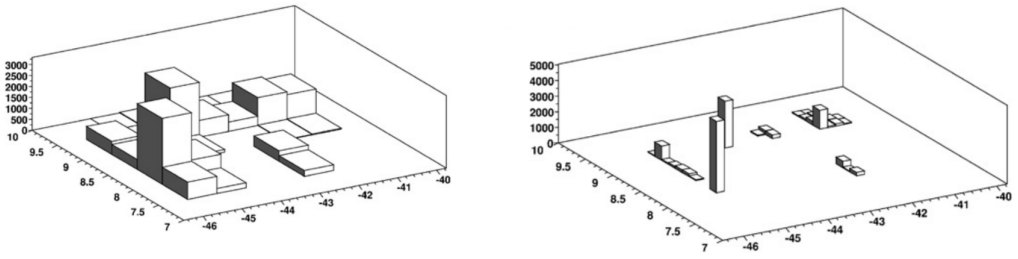

Figure 2.6. **Left:** Example of raw charge distribution on the pads of a single cathode of a MWPC. **Right:** Charge distribution after the Bayesian unfolding. x and y positions are in centimeters. Image from [91].

The ALICE software implements two different tracking algorithms for the muon reconstruction which differ in the way the track parameters are computed from the cluster positions. The first one performs a fit of the track parameters while the second is based on the Kalman filter and compute them analytically [92]. The reconstruction starts from the last chambers: clusters on the chambers of the fourth and fifth stations (individually) are combined and for each combination an initial guess of the track momentum is computed given the averaged magnetic field inside the dipole. A cut is already applied on this guess; if $p < 3\,\mathrm{GeV}/c$ or $p > 3\,\mathrm{TeV}/c$ the track is rejected. On the second step the tracks from station 4 are extrapolated to station 5 and vice-versa. A selection based on a χ^2 cut requires to have at least 3 reconstructed clusters per track out of 4 in the two stations. Finally the tracks are propagated to station 3, 2 and 1 and are validated if at least one cluster over two on each station is found passing the compatibility selection. The connected tracks (those sharing one or more clusters) are removed by keeping the ones with the largest number of clusters or the one with the lowest χ^2 in case of equality. The Kalman tracking recomputes the track parameters and relative covariance at each attached cluster. The reconstructed tracks then can be matched with those reconstructed in the trigger chambers with a χ^2 criterion.

The trigger decision is made on the tracks transverse momentum, strategy which helps to reject low- p_{T} pions and kaons that are expected to be dominant. The measured position on the first trigger station (y_1, as shown in figure 2.7) is extrapolated with a straight line to the interaction vertex. Such line crosses the second station at the position y_∞, corresponding to that of a muon with infinite

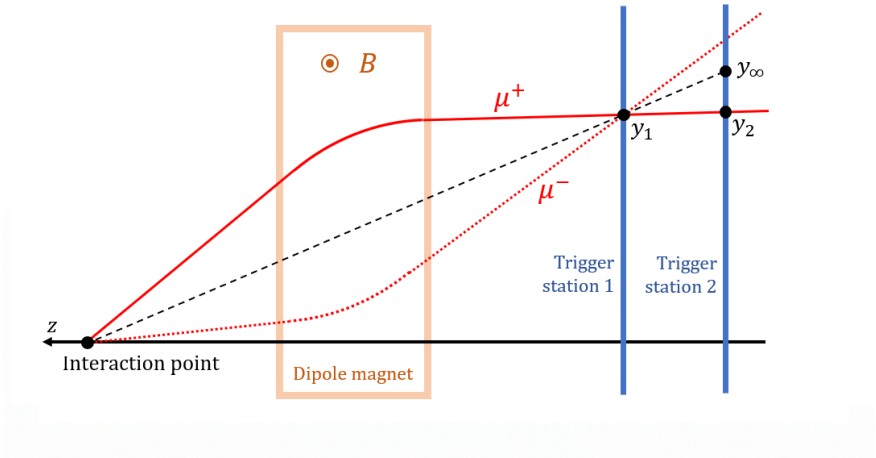

Figure 2.7. The decision on the p_T threshold given by the trigger system is based on the difference between the track positions measured in the two trigger stations. The image is not to scale.

transverse momentum not bent by the magnetic field. The difference between y_∞ and the measured position on the second chamber, $y_2 - y_\infty$, is roughly inverse proportional to the transverse momentum, so that the p_T cut is made by cutting on that difference. Its sign also provides the sign of the charge of the muon. The minimum cut on p_T is about 0.5 GeV/c and is defined by the maximum deviation that the RPCs local boards can measure.

2.4 ALICE physics

The ALICE detector has been thought specifically to study heavy-ion physics, goal achieved thanks to the tracking capability in presence of a very high particle multiplicity. Nevertheless the understanding of the anomalies induced by the hot QCD medium is possible only if a calibration of the various observables is available in systems where the hot matter is not present. This is the main reason why proton-proton collisions have a relevant role in the ALICE physics program. Moreover, as we said, some phenomena observed in p-Pb and pp collisions have blurred the distinction between heavy-ions and non-heavy-ions studies. In the following some recent ALICE measurements on typical ion collision observables are presented, without claiming any completeness on such a vast topic.

Soft processes are those involving a low 4-momentum exchange. More than 99% of the particles produced in heavy-ion collisions have a momentum lower than 2 GeV/c . In Pb-Pb collisions particles with low p_T can be created during

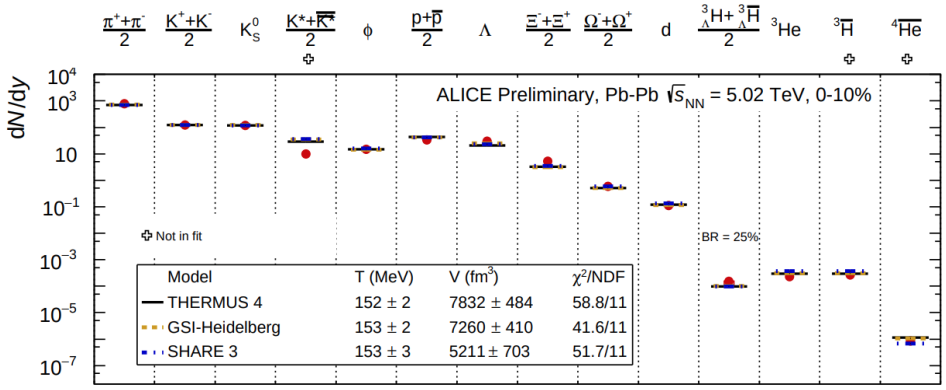

Figure 2.8. Hadron abundances in central Pb-Pb collisions at $\sqrt{s_{\mathrm{NN}}} = 5.02$ TeV fitted with different thermal models. Figure adapted from [94].

the full evolution of the medium and therefore are very important for the characterization of the bulk properties of the QGP in terms of mechanisms of hadron production, statistical and thermal features and collective phenomena. Since the soft probes are produced in a non perturbative regime of the QCD, the interpretation of the result is generally done by means of effective theories and statistical/thermal models.

The various amount of different particle types probes the system freeze-out conditions and the hadronization mechanism [93]. This is shown for example in figure 2.8 where the hadron abundances measured in central Pb-Pb collisions have been fitted with different thermal models showing a chemical freeze-out temperature at $\mu_B \simeq 0$ of 153 MeV, compatible with the crossover transition temperature from lattice QCD.

The initial shape and energy density of the system are given by the overlapping region of the colliding nuclei. For interacting matter, the initial spatial anisotropy as well as the rescattering between constituents reflects on an anisotropy of the measured particles. This observable is sensitive to properties of the system such as its shear viscosity and its entropy. The anisotropy is measured through a Fourier expansion of the azimuthal distribution,

$$\frac{dN}{d\vec{p}} \propto \left[1 + 2\sum_{n=1}^{\infty} v_n(\vec{p})\,\cos\left[n\left(\phi - \psi_n\right)\right]\right]$$

where ψ_n identifies a common symmetry plane. v_2 is known as "elliptic flow". The non-zero value of the first coefficients has been already well established. The left panel of figure 2.9 shows how they are higher in semi-peripheral collisions which have a higher eccentricity. The comparison with hydrodinamics models

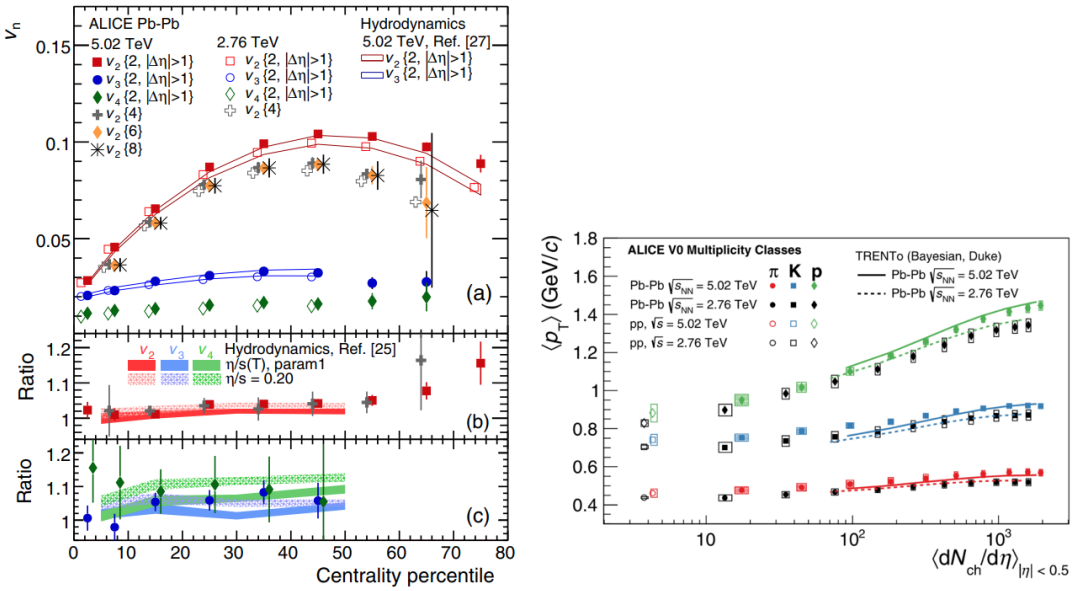

Figure 2.9. Hints on the collective flow. **Left:** Elliptic flow and other v_n coefficients as a function of centrality. The good agreement with hydrodynamics calculations highlights a low value of the shear viscosity to entropy ratio. Figure from [95]. **Right:** Mean transverse momentum of pions, kaons and protons measured as a function of the event multiplicity in proton-proton and lead-lead collisions [96].

can measure the shear viscosity of the medium, as shown in the figure. Together with the anisotropic flow, according to the hydrodynamic picture, the QGP is expected to develop a radial flow which can be measured as a hardening of the particles p_T spectra, as shown in figure 2.9, where one can see that the effect increases with the event multiplicity i.e. the energy density of the collision.

On the other hand, **hard processes** occur at the early stages of the collision and provide a source of coloured probe particles for the QGP created in the later stage. The parton showers interact strongly with the hot medium constituents via elastic and radiative processes before hadronizing into jets. The comparison to jet measurement in pp collisions shows a suppression in heavy ion collision known as jet quenching which can be effectively studied as nuclear suppression R_{AA} . Particularly interesting in light of the binary scaling of the hard processes is the R_{AA} for charged particles measured by ALICE over the full centrality range and reported in figure 2.10 [97]. It shows a counterintuitive strengthening of the suppression for peripheral and ultraperipheral events (the same observables has been measured to be close to unity in p-Pb collisions). As suggested in the paper and in [98], this can be explained looking at the $\langle N_{coll} \rangle$ normalization contained in the R_{AA} definition. The relevant scaling factor for this observable is indeed

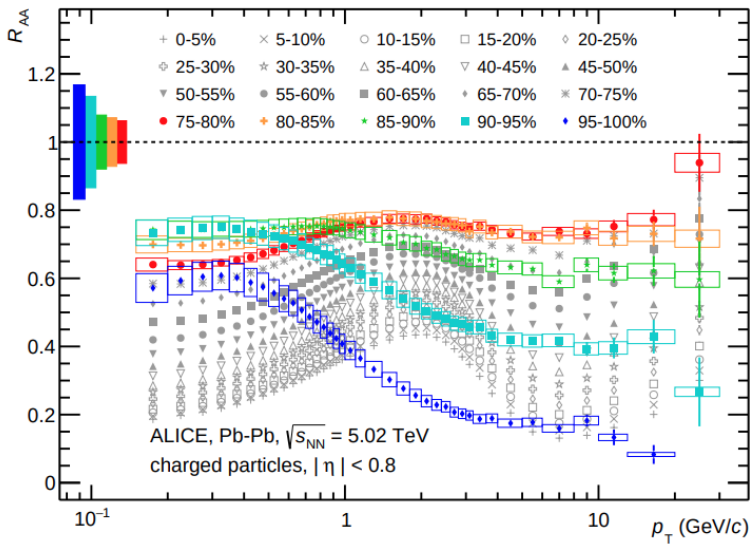

Figure 2.10. Nuclear modification factor for charged particles at midrapidity in Pb-Pb collisions at $\sqrt{s_{\rm NN}} = 5.02$ TeV [97].

the number of *hard* collisions, which depends on the probability of multiple parton interactions. Because of the greater nucleon-nucleon distance, in peripheral collisions the number of multiple parton interactions per $\langle N_{\rm coll} \rangle$ is lower.

Heavy flavour hadrons are another hard probe of the whole phase of the QGP. In the hot medium, quarkonium production is suppressed because of the colour screening of the force binding the $q\bar{q}$ state [99]. Other effects, such as their regeneration by quark recombination at a later stage of the collision has also been studied. Recent studies can be found for example in [100]. Electroweak bosons must be also enumerated among the possible probes of the initial stages of the collisions and the initial nuclear state, but we already have introduced this in the previous chapter and we will dedicate other space to the topic when discussing the results presented in the following chapter. Electroweak bosons are not the only probes sensitive to nuclear modification of the parton distributions. Recent results on heavy flavour and charmonium nuclear suppression factors [101] provide new constraints on this nuclear effect, even if the role of final state effects in these measurements, such as energy loss and radial flow, still needs to be clarified. The advantage of Z and W bosons is that they are not affected by such effects.

Chapter 3

Electroweak analysis

The usefulness of measuring electroweak bosons production in heavy ion collision for the investigation of the cold nuclear matter effects has been presented in section 1.5. We now recap the main points.

1. Z and W boson production is a hard process occurring at a much shorter time scale compared to the one typical of the quark-gluon plasma formation.

2. The leptonic decay products don't have colour charge and don't interact strongly with the hadronic matter. The impact of elastic electromagnetic interactions can be neglected. Z and W bosons leptonic decays bring the information on the initial state of the collision directly to the detector.

3. They are produced by quark-antiquark annihilation, which is well described by perturbative QCD (up to NNLO) and Electroweak theory. The production is sensitive to parton distribution functions and to their modification inside nuclei.

4. Nuclear PDFs (nPDFs) are extracted from global fits to data and currently they suffer from high uncertainties. Electroweak bosons are good opportunities for LHC to provide constraints to the nPDFs at high Q^2 and, in particular, are good opportunities for ALICE to provide constraints at high and low x.

ALICE can measure Z and W bosons by their muonic decay in the forward region, at rapidity between 2.5 and 4. For Z bosons this is done by measuring the $\mu^+\mu^-$ pairs reconstructed in the muon spectrometer. W bosons are measured in the spectrometer by fitting the transverse momentum distribution of single muons. Through this chapter the analysis of Z production in Pb-Pb collision at the

nucleon-nucleon energy $\sqrt{s_{\mathrm{NN}}} = 5.02$ TeV will be presented. In the last sections the results will be shown and the discussion on the nuclear modification to the PDFs will be expanded in light of those measurements. Such results have been presented in several topical conferences and have been published in September 2020 (reference [69]).

3.1 Data sample and event selection

The Z boson production in Pb–Pb collisions at the nucleon–nucleon center-of-mass energy of 5.02 TeV presented in this chapter is based on the full statistics available from LHC at that energy [102]. The data sample can be divided in two main sub-samples, collected in November-December 2015 and in November 2018, respectively.

2015) With the luminosity leveled at $10^{27}\,\mathrm{cm}^{-2}\mathrm{s}^{-1}$, the integrated Pb–Pb luminosity delivered to ALICE in 2015 is about $0.4\,\mathrm{nb}^{-1}$. According to the ALICE standard nomenclature, the period is named LHC15o. About one third of the sample is collected after having switched the polarity of the dipole magnet.

2018) The Pb–Pb luminosity delivered to ALICE in 2018 is about $0.9\,\mathrm{nb}^{-1}$. The dataset is composed of two periods named LHC18q and LHC18r, corresponding to different magnetic field polarities.

The change in the magnetic field polarity has the effect of reversing the trajectory of positive and negative tracks in the detector. As explained later, this has to be taken into account when investigating a possible displacement or misalignment of the apparatus. Due to the long time elapsed between the two periods, a different detector response can be expected. To avoid biases, the LHC15o and LHC18qr samples are first analyzed independently. After having checked the consistency between the results, the full dataset is merged. The analysis based on 2015 data is also systematically compared to the results published in [76].

The data used in this analysis are recorded in the muon spectrometer arm of ALICE. Along with the muon chambers, other detectors are involved in the trigger strategy. In the following some terminology on the trigger classes is explained. It will be used in describing the analysis through the chapter.

- The V0 scintillators serve for the definition of a Minimum Bias trigger (MB). In particular, the trigger class called `CINT` is defined as the logical AND of V0-A and V0-C signals. It can be combined with the ZDC calorimeters to

remove contamination from electromagnetic interactions [103, 104]. In this case the CINT7ZAC trigger class is formed.

- The COVOM trigger class is the sum of V0's discriminated signal. It serves as MB trigger for central and mid-central collisions, up to $\sim$ 60% centrality.

- The trigger class on which the analysis is based is CMUL, which requires a pair of unlike-sign muons with low p_{T} threshold in the muon trigger chambers (greater than $\sim 1\,\mathrm{GeV}/c$), in coincidence with a CINT trigger.

- The CMSL and CMSH classes require a single muon triggered by the muon chambers plus the CINT MB condition. They differ in the muon p_{T} threshold, which is $1\,\mathrm{GeV}/c$ for CMSL (L=Low) or $4.2\,\mathrm{GeV}/c$ for CMSH (H=High).

A first offline event selection, called "Physics Selection", is used to select good collision candidates in the collected sample. According to the V0 and ZDC time information, it rejects beam-gas background events, pile-up events and other events with poor reconstruction quality [103]. In order to reject electromagnetic background which is dominant in (ultra)peripheral collisions, a cut on the event multiplicity is also applied, selecting only events with centrality up to 90%.

3.1.1 Event normalization

The events used to measure the Z boson production are those which triggered a CMUL trigger, therefore containing a pair of opposite sign muons. The number of events in this biased sample must be corrected to obtain a physical number which is independent on the ALICE detector configuration. Such number is the number of recorded Minimum Bias, whose ratio to the number of CMUL triggers is called "normalization factor", F_{norm}:

$$N_{\mathrm{MB}} = F_{norm} \cdot N_{\mathrm{CMUL}}$$

The computation of F_{norm} is done on a run by run basis and is performed using the lowest level trigger counters, before the ALICE Central Trigger Processor (CTP) vetoes, called L0b. The CTP selects events with different features at rates that can be downscaled to cope with the data acquisition system bandwidth. Vetoes at Level 0 can occur for example in case one of the detecors is busy, past-future protection (in a configurable time interval) is required or when L0 inputs arrive during CTP dead time (1.6 μs). Since the CTP inputs don't undergo any Physics Selection, a purity factor $\mathcal{P}$ must be applied to each sample. This is simply computed as the fraction of events firing a trigger class which satisfy also the Physics

Selection.

$$F_{norm} = \frac{\mathrm{L0b_{MB}} \cdot \mathcal{P}_{\mathrm{MB}}}{\mathrm{L0b_{MUL}} \cdot \mathcal{P}_{\mathrm{MUL}}} \tag{3.1.1}$$

where $\mathrm{L0b_{MB}}$ and $\mathrm{L0b_{MUL}}$ are the scaler (trigger rate) values recorded at the L0b level for the V0 (MB) and dimuon triggers.

In Pb-Pb data taking the bunch spacing is 100/150 ns. In the data selection, since the muon trigger has a time resolution of 25 ns, the reconstructed muon events are not sensitive to pile-up from different bunches (out-of-bunch pile-up). Anyway the detector cannot distinguish multiple collisions during a single bunch crossing (the so called in-bunch pile-up) and a correction factor must be applied to account for the number of events in which this happens. For each run, let μ be the mean number of collisions per bunch crossing. Following the poissonian statistics, the probability of having at least one interaction is $1 - e^{-\mu}$. Among those cases where at least one collision occurs, the mean number of collisions is

$$\frac{\mu}{1 - e^{-\mu}} \equiv F_{pile-up}$$

Since ALICE is sensitive to only one of those, this is also the multiplicative factor to apply to the measured number of MB events to have an estimate of the real number of interactions. μ, in turn, is assessed considering that the number of measured MB per unit time ($MBRate$, corrected for the purity of Physics Selection) divided by the bunch crossing frequency is the probability of having at least one collision:

$$1 - e^{-\mu} = \frac{\mathcal{P}_{\mathrm{MB}} \cdot MBRate}{n_b \cdot f_{\mathrm{LHC}}}$$

Here n_b is the number of colliding bunches in LHC and f_{LHC} is the revolution frequency, equal to 11245 Hz. The factor $F_{pile-up}$ turns out to be very small, around 1.004.

Figure 3.1 shows the evolution run by run of the normalization factor F_{norm} for the 2018 data sample. Together with the described computation, other two less precise methods are displayed. They are used as sanity check of the calculation and serve to determine a systematic uncertainty on F_{norm}. They use the recorded triggers stored offline. According to the first method, the factor is computed for each run as

$$F_{norm} = \frac{N_{\mathrm{MB}}}{N_{\mathrm{MB\&0MUL}}} \tag{3.1.2}$$

The `CINT7ZAC` MB trigger is used. The denominator is the number of MB events which also triggered an opposite-sign low- p_{T} trigger.

The second calculation simply aims to improve the statistical precision. The number of `CMSL` triggers is larger than the `CMUL` one, and the normalization factor

can be computed with the following "indirect" method:

$$F_{norm} = \frac{N_{\text{MB}}}{N_{\text{MB\&0MSL}}} \times \frac{N_{\text{CMSL}}}{N_{\text{CMSL\&0MUL}}} \tag{3.1.3}$$

where $N_{\text{CMSL\&0MUL}}$ is the number of `CMSL` events where an opposite-sign low- p_{T} trigger is fired.

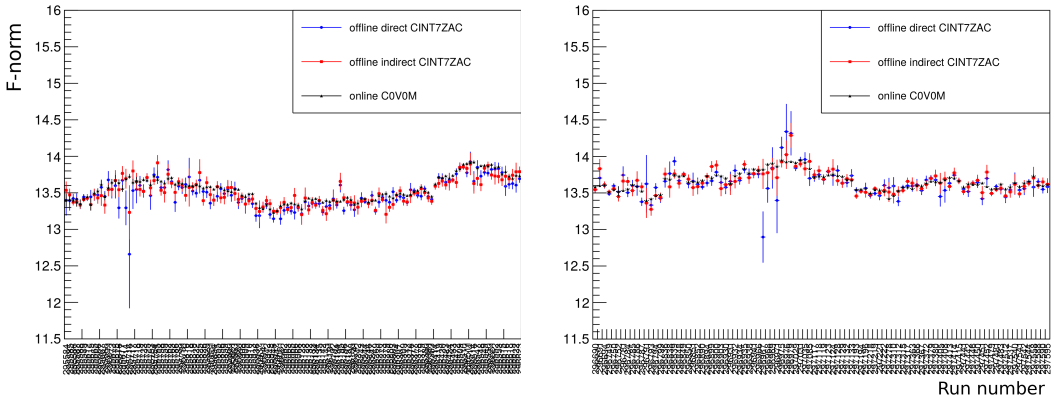

Figure 3.1. Comparison of the results for the normalization factor for each run of the LHC18q (left) and LHC18r (right) periods, computed with the online (equation 3.1.1), offline direct (equation 3.1.2) and offline indirect (equation 3.1.3) methods [105].

Once the run-dependent normalization factor is computed, the total number of MB events can be found by adding the contribution from each run. Equivalently, the averaged normalization factor has the following expression (r is the run index):

$$F^{tot}_{norm} = \frac{\sum_r F^r_{norm} N^r_{\text{CMUL}}}{\sum_r N^r_{\text{CMUL}}}$$

The number of `CMUL` events recorded in 2015 and 2018 is listed in table 3.1. The weighted F_{norm} is 13.06 ± 0.06, computed with the before-CTP scalers. The quoted uncertainty is systematic, assigned as the largest difference between this computation and those performed with the offline methods. Depending on the periods, it ranges from 0.3% to 0.5% of the central value.

3.1.2 Centrality and Minimum Bias

The centrality of an event is determined according to the V0-A and V0-C signals, as described in section 1.2.3. In general, this is contaminated by events without hadronic interactions, where the signal comes from electromagnetic processes.

However, events with only electromagnetic interactions produce a small multiplicity, producing a small V0 amplitude. The effect of this background can be neglected for centralities below 90% but is important in (ultra)peripheral collisions. The centrality classes are defined by cutting on the V0 signal and a hard cut is set to the value corresponding to 90% of the total signal. Events beyond this point are discarded from the analysis. This upper bound is called "anchor point" [80].

The aforementioned computations give a normalization factor referred to all the events in the 0-90% centrality class. To compute the Z boson yield in smaller centrality intervals one should consider that the CMUL distribution highly depends on centrality. This is not the case for the MB events, which are uniformly distributed versus centrality. Such flatness is shown in figure 3.2 where the run-evolution of the number of CINT trigger is computed in the $0-30\%$, $30-60\%$ and $60-90\%$ classes and normalized to the same number in $0-90\%$. The ratio is compatible with the value $1/3$ within uncertainties. The approach used to compute centrality-dependent results is therefore as follows: the number of MB is first computed in the full 0-90% class, then scaled according to the centrality bin width.

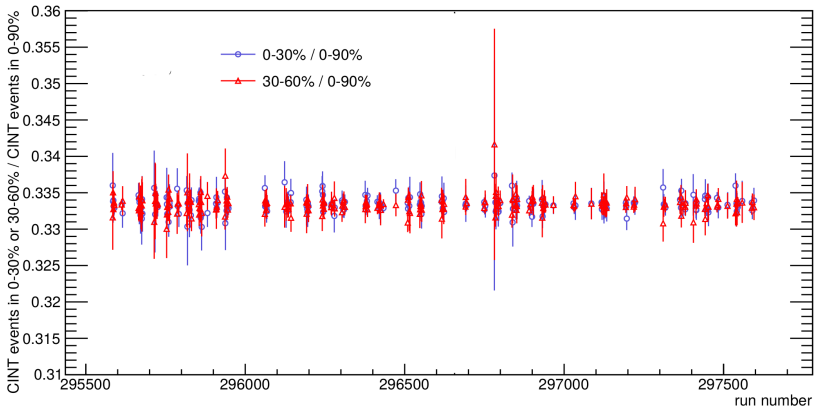

Figure 3.2. Number of CINT events in three centrality classes (0-30, 30-60 and 60-90%) normalized to the number recorded in 0-90%. The V0 signal is stable during time and uniformly distributed over centrality. ⋆THIS THESIS⋆

3.2 Track selection and signal extraction

A high purity of muons in the data sample recorded by the muon chambers is achieved thanks to the presence of the front absorber. It stops the particles with

momentum lower than $\sim 4\,\mathrm{GeV}/c$ as well as most of the hadrons [89]. As shown later in figure 3.5 according to simulation, the muons from Z boson decays have large momentum, with p_{T} peaked at one half of the boson mass ($\sim 45\,\mathrm{GeV}/c$). The selection of muons with high p_{T} allows to obtain an almost background-free sample. Other offline track cuts are further applied:

- *Trigger-tracking matching*. Muon candidates reconstructed in the tracking chambers are rejected if they don't match a track segment reconstructed in the trigger system. Since the trigger stations are placed downstream of the iron wall (more than seven interaction lengths), this requirement reduces the contamination of residual hadrons leaking from the front absorber.

- *Detector acceptance*. The cut $-4 < \eta_\mu < -2.5$ is applied on the single muon pseudorapidity, to reject tracks reconstructed at the edge or outside the geometrical acceptance of the spectrometer.

- *Radial position at the end of the absorber*. As sketched in figure 3.3, the different material regions of the front absorber can be identified by the polar angle at the end of the absorber. This angle is called θ_{abs} and identifies the position of a point on the end face with respect to the laboratory coordinate system. The dispersion of the vertex position along the z axis and the Coulomb multiple scattering make θ_{abs} different from the polar angle at which the particle is emitted. To avoid multiple effects from various materials of the absorber, θ_{abs} is selected to be $2^\circ < \theta_{abs} < 10^\circ$, rejecting tracks crossing the thicker (high-Z) materials.

- *Particles not from the interaction vertex*. The particles crossing the front absorber undergo multiple Coulomb scattering. The root mean square (RMS) of the total scattering angle has the following expression as a function of the particle momentum p, velocity β and charge number z [106]:

$$\mathrm{RMS}_{\Delta\theta} = \frac{13.6\,\mathrm{MeV}}{\beta c\, p}\, z\sqrt{\frac{x}{X_0}}\,\left[1 + 0.038\,\ln\left(x/X_0\right)\right] \qquad (3.2.1)$$

  The thickness of the scattering material in unit of radiation lengths is $x/X_0 \simeq 60$. Its value is larger in the angular region $2^\circ < \theta_{abs} < 3^\circ$ because of the tungsten layer on the end side. The Distance of Closest Approach (DCA) is defined as the distance in the transverse plane between the primary vertex and the straight extrapolation of the trajectory of the track reconstructed in the chambers (figure 3.3). For particles produced close to the vertex with small angles, DCA is proportional to the Coulomb scattering

angle so that, using eq. (3.2.1), it results

$$\sigma\,(p \times \mathrm{DCA}) \simeq p \times \mathrm{RMS}_{\mathrm{DCA}} \propto p \times \mathrm{RMS}_{\Delta\theta} \simeq \text{constant}$$

For tracks coming from the interaction vertex, the dispersion in the distribution of $p \times$ DCA doesn't depend on any other variable. A cut on $p \times$ DCA can therefore reject beam-induced particles and other particles produced inside the front absorber. The cut also affects fake tracks, which are distributed across the DCA plane. The Z boson analysis involves only high-momentum muons; for those tracks, the same $p \times$ DCA cut is an even tighter condition on the distance to the primary vertex. For this analysis, only tracks with $p \times \mathrm{DCA} < 6\sigma$ are considered, the width of the distribution σ being extracted from a Gaussian fit of the data. An example of the $p \times$ DCA distributions is displayed in figure 3.4 for the $2^\circ < \theta_{abs} < 3^\circ$ and $3^\circ < \theta_{abs} < 10^\circ$ regions separately.

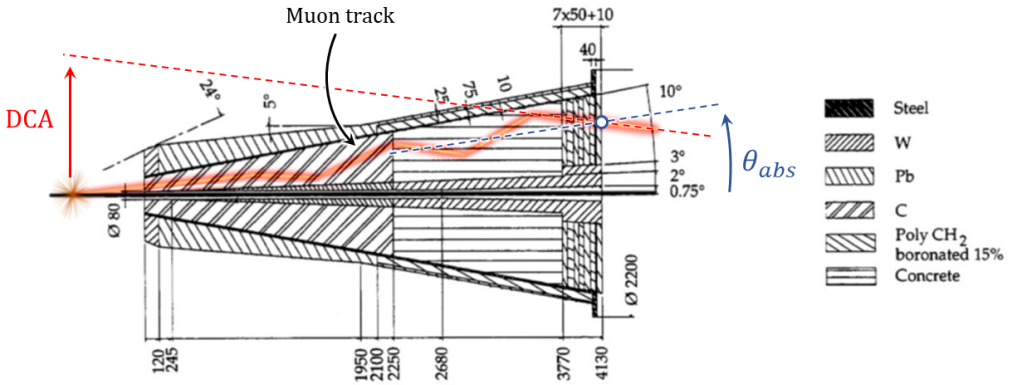

Figure 3.3. Geometry of a track crossing the front absorber.

The influence of these cuts on the number of reconstructed muon candidates is summarized in the first rows of table 3.1.

This analysis aims at measuring the production rate of Drell-Yan muons in a kinematic region close to the Z boson. The production of Z bosons is peaked at central rapidities and the ALICE spectrometer can measure only a small fraction of the total cross section. Measuring an inclusive cross section would require a huge correction factor, which would be necessarily model-dependent. It is preferable to restrict the measurement to the phase space accessible by the detector. This will provide us with unbiased results that will be compared with theoretical

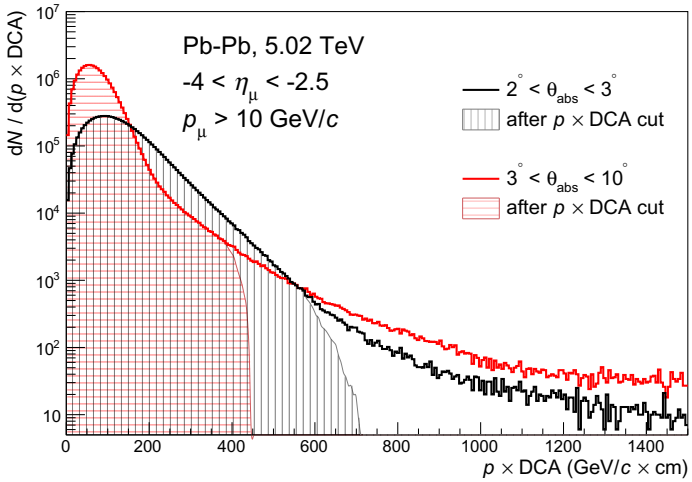

Figure 3.4. Distribution of $p \times$ DCA for tracks reconstructed with $2^\circ < \theta_{abs} < 3^\circ$ and with $3^\circ < \theta_{abs} < 10^\circ$. The choice $p_\mu > 10\,\mathrm{GeV}/c$ removes the major part of fake tracks. The effect of the $p \times \mathrm{DCA} < 6\sigma$ cut is shown; it rejects beam-induced particles as well as fake tracks with anomalous DCA. ⋆THIS THESIS⋆

	LHC15o (M=millions)	**LHC18qr**	
CMUL after physics selection	127 M	274 M	CMUL events
and with centrality 0-90%	1950 M	4210 M	muons
η_μ selection	1260 M	2723 M	muons
η_μ and θ_{abs} selection	1221 M	2643 M	muons
η_μ, θ_{abs}, $p \times DCA$, trigger match	170 M	358 M	muons
	53 M	112 M	unlike-sign pairs
previous + $p_{\mathrm{T},\mu} \geq 20\,\mathrm{GeV}/c$	81	171	unlike-sign pairs
previous + $60 < m_{\mu\mu} < 120\,\mathrm{GeV}/c^2$	66	143	unlike-sign pairs

Table 3.1. Number of triggers and tracks passing the offline selection. The number of CMUL events differs from the number of MB events by a factor 11.9 in LHC15o and by a factor 13.6 in LHC18qr (see the description of F_{norm}, section 3.1.1).

calculations. The fiducial region chosen for the analysis is driven by the considerations detailed above and consists of the following three selections.

- *Rapidity*. The rapidity of the muon pairs (that is, of the boson candidate) is required to be $2.5 < y_{\mu\mu} < 4$. The single-muon pseudorapidity cut, $-4 < \eta_\mu < -2.5$, is also part of the conditions. Notice that although the muon spectrometer is placed at negative rapidity, we adapt our notation to the one found in ALICE papers by writing the dimuon rapidity as positive.

- *Muon* p_T . Only muons with high transverse momentum are used. The cut is set to $p_{T,\mu} \geq 20\,\mathrm{GeV}/c$. This choice reduces the number of dimuons coming from lower mass quarkonia states and the combinatorial background.
- *Invariant mass*. The Z boson region is identified by selecting a dimuon invariant masses close to the Z boson mass. The window should include the full Z peak and exclude the lower invariant mass virtual photons contribution. To be consistent with other ALICE works [67, 76], the chosen region is $60 < m_{\mu\mu} < 120\,\mathrm{GeV}/c^2$, symmetric around $90\,\mathrm{GeV}/c^2 \simeq M_Z$. The width of this interval is about three times the width of the Z peak reconstructed by the detector (see right panel of figure 3.12).

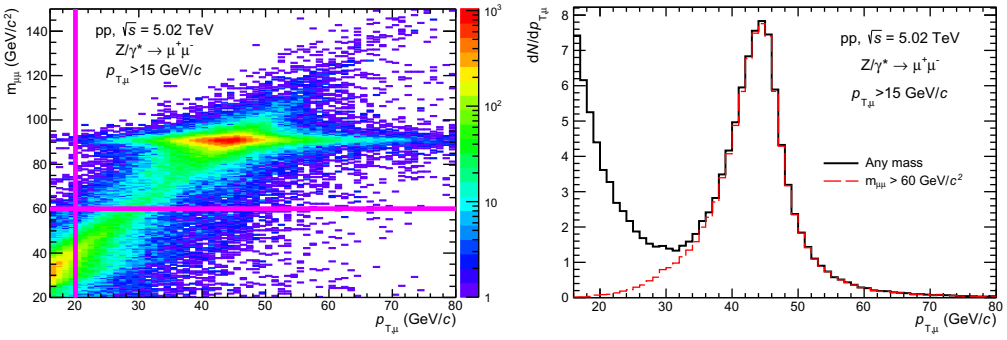

Figure 3.5. Simulation of $q\bar{q} \rightarrow \mu^+\mu^-$ process in pp collision at 5 TeV. The plots show the correlation between the muons invariant mass and the muon transverse momentum. In the left panel the values $p_{T,\mu} = 20\,\mathrm{GeV}/c$ and $m_{\mu\mu} = 60\,\mathrm{GeV}/c^2$ are highlighted with solid lines. In the right panel, the Z and γ contributions are both visible, with the former peaked approximately on $m_Z/2$. The virtual photons tail is drastically reduced when the cuts are applied. The event generator is POWHEG [107] and the particles are generated in the rapidity region of the ALICE muon arm. ⋆THIS THESIS⋆

In a wide region close to invariant mass (IM) of $60\,\mathrm{GeV}/c^2$ (single muon transverse momentum around $30\,\mathrm{GeV}/c$) the lepton pair production proceeds through the interference between virtual photons and Z bosons . The γ^* contribution is more relevant at low p_T and is suppressed by the fiducial cuts. Some information on the kinematics of the produced muons are reported in figure 3.5. The p_T and IM cuts are highly correlated and, given the chosen IM window, the p_T cut has a very small impact on the signal.

3.2.1 Signal extraction and combinatorial background

As a consequence of the p_T cut the number of opposite charge dimuons drops to 81 and 171 in the 2015 and 2018 data samples respectively (table 3.1). At this

point the sample is almost without background. The signal can be extracted by counting the number of unlike-sign muon pairs with invariant mass between 60 and 120 GeV/c^2. For the full dataset, such number is 209 (last line of table 3.1).

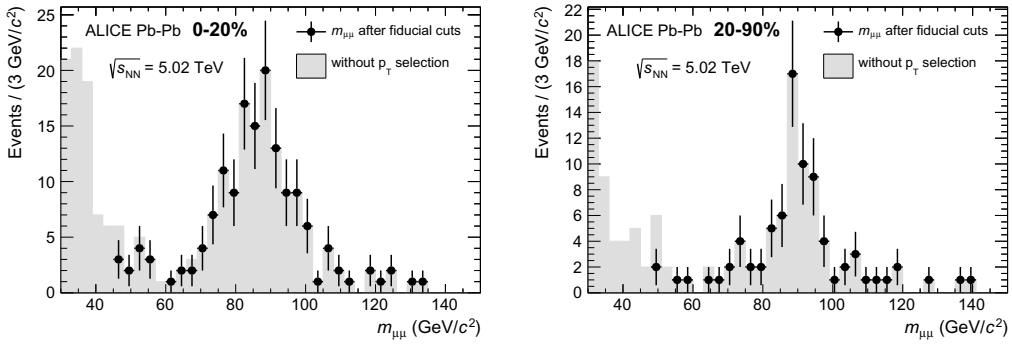

Figure 3.6. Raw invariant mass distribution of opposite-charge muon pairs reconstructed in the full data sample, after full track selection (dots) or without $p_{T,\mu}$ cut (shadowed area). **Left:** 0-20% centrality events. **Right:** 20-90% centrality. ⋆THIS THESIS⋆

The IM spectra of dimuons are shown in figure 3.6 for central (0-20%) and peripheral (20-90%) collisions separately. The distributions resulting from track selection without the $p_{T,\mu}$ cut are drawn in background. Once again, one can notice that the impact of this cut on the signal is negligible. The remaining physical background can be evaluated with Monte Carlo simulations. It turns out to be of the order of 1% and will be included in the systematic uncertainty (section 3.4).

The random combinatorial background is even smaller. Since the probabilities to reconstruct uncorrelated pairs of same or opposite charges are similar, the combinatorial component is estimated by counting the number of like-sign muon pairs reconstructed in the fiducial region of the analysis. On this purpose, the analysis is redone with the event selection requiring a `CMSH` trigger. The reliability of this method was verified since such selection reconstructs the same unlike-sign spectra built with `CMUL` trigger. A total of four like-sign dimuons is found passing the event and track selection. Three of them have invariant mass below 0.5 or above 250 GeV/c^2, while the fourth has invariant mass $m_{\mu\mu} = 92\,\text{GeV}/c^2$ and rapidity $y_{\mu\mu} = 2.95$. We choose to subtract the like-sign IM spectrum (made of a single effective event) to the signal spectrum. Other choices would be equally valid and in any case the uncertainty deriving from this background source does not affect the results, given the total statistical and systematic precision.

Further checks on this point are now described. The probability of a mistake in the sign of the reconstructed muon is sizable. It has been evaluated with the Monte Carlo simulation described in the following section. Given the align-

ment and momentum resolution of the detector, the probability of reconstructing a muon in the Z boson p_{T} region with flipped sign is between 0.4% and 0.5%. In a sample of 209 good candidates, one should expect one or two Z boson dimuons ($\sim$ 0.9% of the total) reconstructed as having the same charge. A further consistency check can be done by studying the IM shape of like-sign random pairs once the $p_{\mathrm{T},\mu}$ cut is released (this is to be conservative). The number of events can be measured in the low mass region and extrapolated in the IM window of the analysis. The plot is shown in figure 3.7. The distribution has been fitted with different functions (power-law functions, double and triple exponential, Crystal Ball function [108]) and in different ranges, both at lower (0 to 15 GeV/c^2) and higher mass ($\geq$ 15 GeV/c^2). The best agreement is obtained with a Crystal Ball function having a gaussian core and a right-hand power-law tail:[1]

$$f_{CB}(m) = \mathcal{N} \times \begin{cases} \exp\left(-\frac{(m-\mu)^2}{2\sigma^2}\right) & \text{if } \frac{m-\mu}{\sigma} < \alpha \\ A\left(B - \frac{m-\mu}{\sigma}\right)^{-n} & \text{if } \frac{m-\mu}{\sigma} \geq \alpha \end{cases} \tag{3.2.2}$$

The best-fit distributions are integrated in the $60 - 120\,\mathrm{GeV}/c^2$ interval to estimate the combinatorial background. The result strongly depends on the chosen function and fit range but it is always below 10^{-2} events. This corroborates the negligibility of this background source.

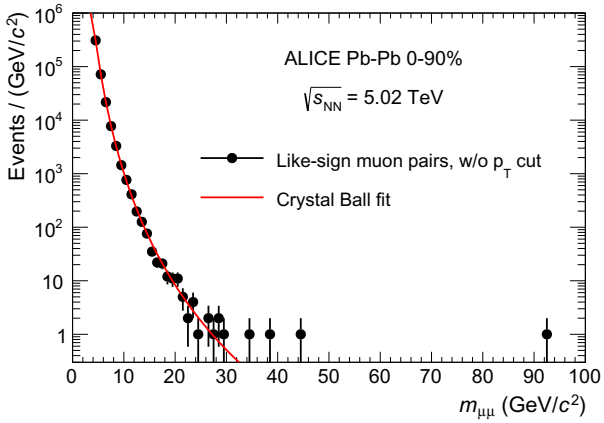

Figure 3.7. Invariant mass distribution of muon pairs with same charge. The best fit with Crystal Ball function (3.2.2) is shown ($\chi^2/\mathrm{ndf}\big|_{15-60\,\mathrm{GeV}/c^2} = 13.4/16$). ⋆THIS THESIS⋆

[1] The fitted parameters are μ, σ, α and n. A and B provide the correct regularity, $\mathcal{N}$ the normalization.

Table 3.2 reports the final raw signal. The number of candidates measured during each LHC period is also specified. The numbers must be corrected for the efficiency of the detector and analysis algorithm. The signal is also split in three centrality classes and four rapidity regions. They are the differential bins chosen for the final results. The numbers are treated as poissonian counts and in the last column the statistical uncertainty of the signal is reported as percentage. The centrality and rapidity intervals are chosen so that the uncertainty is kept below 20%.[2]

	15o	18q+r	Total	$1/\sqrt{\text{Total}}$
Total	65*	143	208*	7%
0-10% centrality	21	51	72	12%
10-20% centrality	18	45	63	13%
20-90% centrality	26*	47	73*	12%
$2.50 < y_{\mu\mu} < 2.75$	15	28	43	15%
$2.75 < y_{\mu\mu} < 3.00$	20*	47	67*	12%
$3.00 < y_{\mu\mu} < 3.25$	16	50	66	12%
$3.25 < y_{\mu\mu} < 4.00$	14	18	32	18%

Table 3.2. Raw number of candidates in the fiducial region. The results versus centrality are integrated over rapidity and vice versa. The values with (*) are after the subtraction of the event found in the like-sign dimuon spectrum.

3.3 Efficiency correction

The errors made in the calculation of the number of events are not limited to the intrinsic poissonian uncertainties. One of the fundamental systematics concerns the reconstruction efficiency. This is in general the product of the intrinsic detectors efficiencies, the efficiency of the analysis algorithm coming from the offline selections and cuts, and the geometrical acceptance of the apparatus. Because of the choice of providing results in the fiducial region described in the previous section, this analysis doesn't require a pure geometrical acceptance correction. This reduces the impact of the kinematic distribution of the simulated generated particles on the efficiency calculation. The Monte Carlo simulation proceeds in the following way.

The process $q\bar{q} \rightarrow Z/\gamma^*$ is generated with POWHEG including the full interference structure between photons and Z bosons . The bosons are then forced

[2]The uncertainty on the difference between unlike-sign ($\mu\mu^{\pm\mp}$) and like-sign ($\mu\mu^{\pm\pm}$) spectra is propagated with the formula $\delta N_Z = \sqrt{N_{\mu\mu^{\pm\mp}} + N_{\mu\mu^{\pm\pm}}}$. Its relevance on this analysis is so small that this comment couldn't be more than a footnote.

to decay into muon pairs with a cut set to $p_{T,\mu} \geq 15\,\mathrm{GeV}/c^2$. POWHEG (POsitive Weight Hardest Emission Generator) is a generator of hard processes (heavy quarks, Higgs and electroweak bosons) with Next-to-Leading-Order precision [107]. CT10 NLO is used as baseline for the parton distributions inside nucleons, and EPS09 nuclear modification [50] is added to describe the lead environment. The output of POWHEG contains the product of the hard parton interactions and needs to be passed to a shower Monte Carlo program. Pythia-6 is used to this purpose [109]. It applies initial and final state radiations, p_{T} kick, boost and the requested cuts on the final state. At this point, the final state particles are passed to the GEANT3 transport code which propagates them through the detector, simulating its geometry and creating the hits in the active elements. The information from the hits are finally merged to reconstruct the particles.

Since the conditions of the detector may change during the data-taking, the simulation is done on a run by run basis, using the information from the ALICE offline conditions database. For each run, one Z/γ^* signal every 500 dimuon triggers (`CMUL`) is generated. The efficiency is estimated as the fraction of the generated dimuons that are actually reconstructed:

$$eff = \frac{N_{reco}(analysis)}{N_{gen}(fiducial\ \ region)} \tag{3.3.1}$$

The generated particles are required to pass the cuts which define the fiducial region chosen for the analysis, while the reconstructed tracks are selected with the same selection described in the previous section. The evolution run by run and the rapidity dependence of *eff* is shown in figure 3.8.

3.3.1 Isospin effects

The generated distributions come from an incoherent sum of nucleon-nucleon collisions where the nuclear effects are eventually parameterized by the chosen nuclear PDF set. To account for the specific quark flavour content in the lead nucleus, one needs to compute *eff* for all the possible binary nucleon-nucleon collisions (proton-proton, neutron-proton, proton-neutron and neutron-neutron). The results are then averaged weighting on the number of protons and neutrons involved in the collision. The weights are given by the following formula (to be read with $A = 208$ and $Z = 82$):

$$d\sigma_{\mathrm{AA}} \propto \frac{Z^2}{A^2}\, d\sigma_{\mathrm{pp}} + \frac{(A-Z)^2}{A^2}\, d\sigma_{\mathrm{nn}} + \frac{Z(A-Z)}{A^2}\, \left(d\sigma_{\mathrm{pn}} + d\sigma_{\mathrm{np}}\right)$$

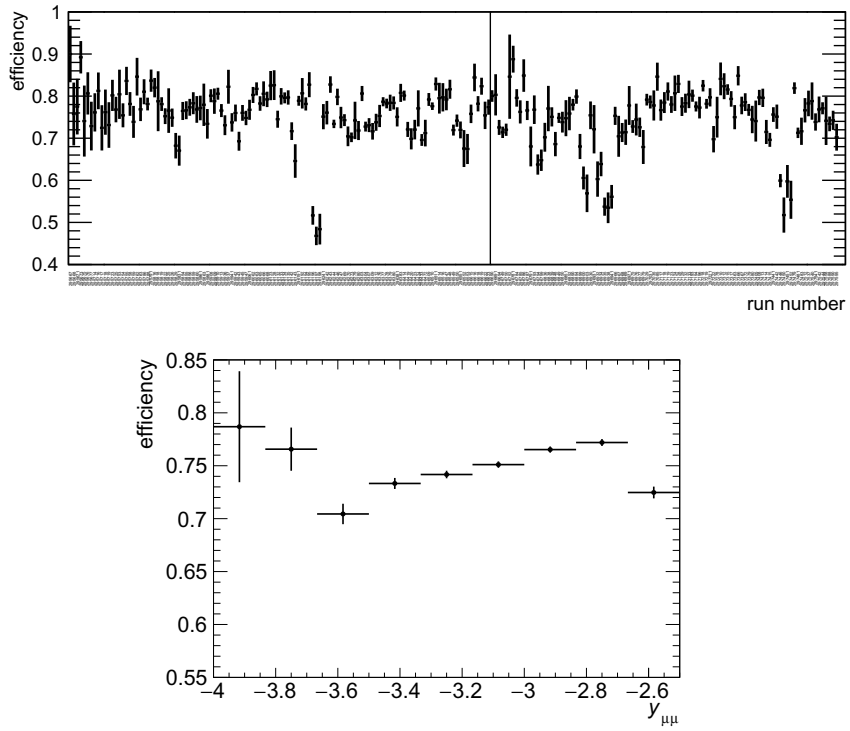

Figure 3.8. **Top:** time dependence of the efficiency from nucleon-nucleon collisions simulated with POWHEG. The vertical line separates the 2018 periods with different B-field polarity. **Bottom:** efficiency as a function of the dimuon rapidity, negative according to ALICE coordinate system. ⋆THIS THESIS⋆

Checks have been performed demonstrating that the isospin effects on the efficiency of this analysis are negligible. An example is shown in table 3.3 where the efficiency for few runs is computed with high statistics and for the different nucleon-nucleon systems. The periods corresponding to the different magnetic field polarity are tested separately to avoid biases due to the detector alignment. As one can see in the table, the values are consistent with each other at the *permille* level.

	pp	pn	np	nn
Run 295788 (LHC18q)	78.77 ± 0.18	78.74 ± 0.17	78.92 ± 0.18	78.74 ± 0.17
Run 296749 (LHC18r)	72.09 ± 0.19	72.43 ± 0.19	72.33 ± 0.20	72.08 ± 0.19

Table 3.3. Comparison of the efficiencies in two runs with opposite magnetic field polarity, for different colliding systems. The generator is POWHEG. The values are expressed as percentage.

As a remark, we want to stress that the flavour content actually has an impact on the Z boson production cross section, which is larger when neutrons are involved (see for example the comments about the R_{AA} results, on section 3.5). Nevertheless the shape of the kinematic distribution is not modified to the point of having an impact on the efficiency, which of course is blind to any constant scale factor in the cross sections. An example of such distributions is reported in figure 3.9. Concerning the dependence on the muon transverse momentum, one has to consider that the detector efficiency doesn't change significantly versus $p_{T,\mu}$ in the high-p_T region of this analysis. On the other hand, figure 3.8 shows that there could be some rapidity dependence. Nevertheless, this is offset by the fact the distributions of Z production versus rapidity doesn't change when different nucleon-nucleon collisions are considered (right panel of figure 3.9).

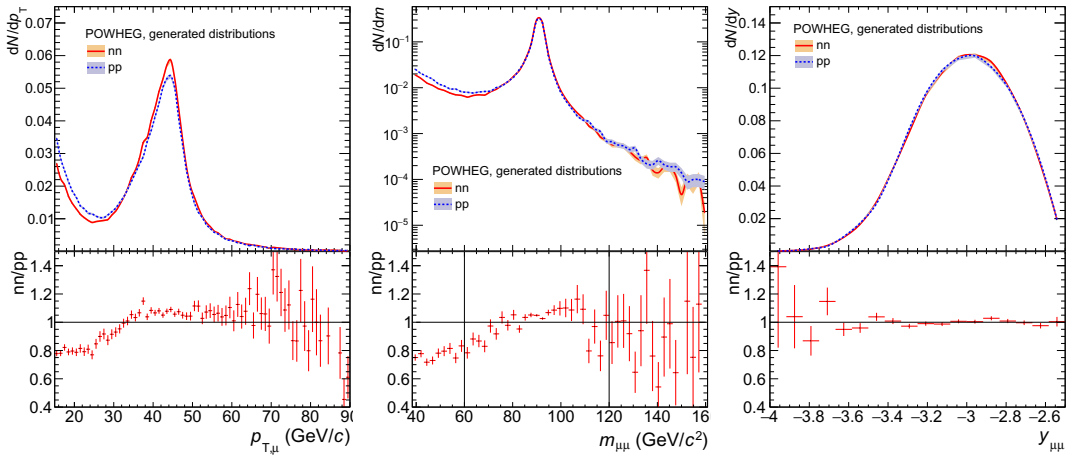

Figure 3.9. Kinematic distributions of Drell-Yan muons generated with POWHEG. Comparison between proton-proton and neutron-neutron collisions at $\sqrt{s_{NN}} = 5.02$ TeV . The distributions are normalized according to the number of simulated signals, so they are insensitive to a multiplicative factor on the integrated cross sections. **Left:** Single muon transverse momentum. **Middle:** Muon pairs invariant mass. **Right:** Muon pairs rapidity (negative, according to ALICE internal conventions). ⋆THIS THESIS⋆

3.3.2 Centrality dependence

The number of binary interactions in a lead-lead collision at $\sqrt{s_{NN}} = 5$ TeV increases from few unities to two thousands as the collision becomes more central. The multiplicity of produced particles increases in turn (not linearly, as explained in chapter 1). The increase in the occupancy of the detector produces a sizable decrease of the efficiency for the events of our interest; this has to be properly taken

into account in the simulation. To this end, an embedding technique is used; before running the reconstruction, the hits produced by the detector response for the simulated signal are merged with those of Minimum Bias raw data recorded in a real event. This allows the reproduction of realistic background conditions. Because of technical difficulties (more CPU time and resources), this simulation contains the following (non-crucial) approximations. First, only collisions between protons are simulated. This is actually not an issue, since section 3.3.1 demonstrates that the efficiency from proton-proton collisions can be used independently on the real isospin dependence of the "nucleon-nucleon $\to \mu^+\mu^-$" cross section. Second, Pythia-8 is used as standalone generator. Pythia is a LO (Leading-Order) generator and it is expected to reproduce the Drell-Yan distribution worse than POWHEG. A comparison of the generated muon p_{T}, dimuon rapidity and dimuon invariant mass provided by Pythia and POWHEG is proposed in figure 3.10. Such distributions are relevant for the efficiency calculation because they provide the number of particles falling in the fiducial region.

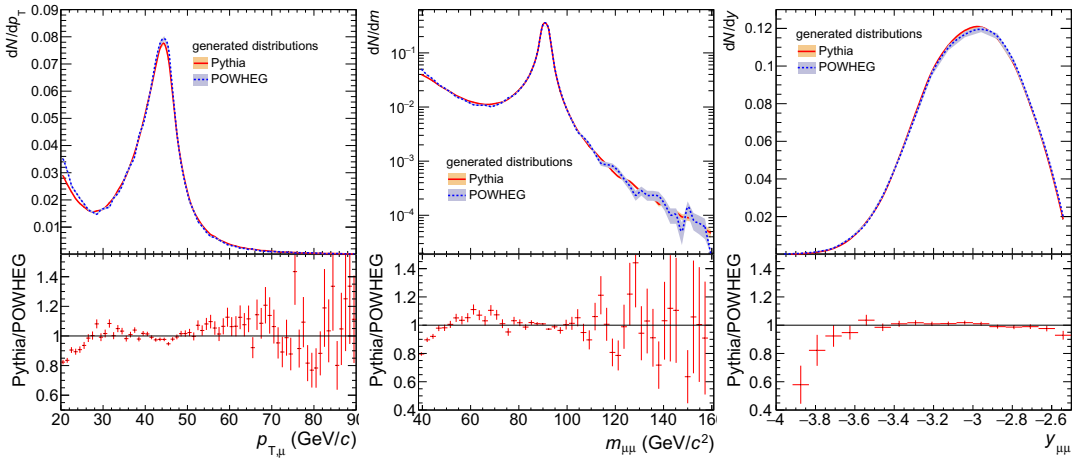

Figure 3.10. Kinematic distributions of generated Drell-Yan muons. Comparison between Pythia and POWHEG (interfaced with Pythia) generators. **Left:** Single muon transverse momentum. **Middle:** Muon pairs invariant mass. **Right:** Muon pairs rapidity (negative, according to ALICE internal conventions). ⋆THIS THESIS⋆

Figure 3.11 reports the centrality dependence of the efficiency. The drop of efficiency in central collision amounts to $\sim 9.5\%$ of the peripheral value, mainly because of the lower muon trigger efficiency at higher multiplicity. Further evidence is that according to simulations the occupancy plays a negligible role in peripheral events, where the interaction tends to a nucleon-nucleon collision. For this reason, the embedded simulation and the POWHEG one provide consistent

values for centrality classes above $\sim 70\%$.

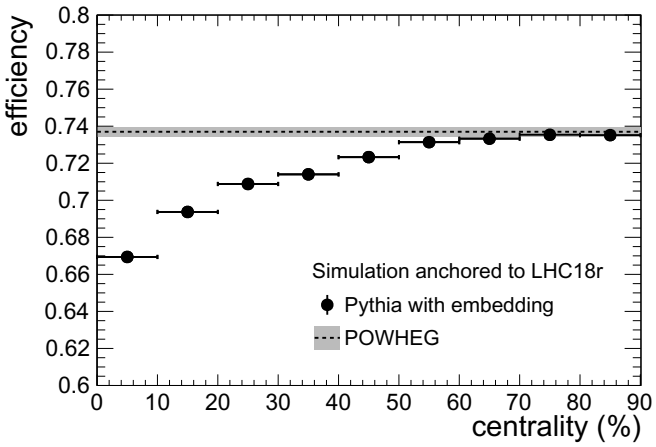

Figure 3.11. Efficiency from embedded proton-proton Pythia-8 simulation as a function of centrality. The comparison with the POWHEG simulation without embedding is added. ⋆THIS THESIS⋆

To compute the final efficiency, the embedded simulation is taken as a reference to assess its centrality dependence. A second order correction is then implemented thanks to the POWHEG simulation. For each bin Δ in the kinematic variables and each centrality class cc, the efficiency is computed as

$$eff(\Delta, cc) = eff(\text{POWHEG};\, \Delta, cc) \times \frac{eff(embedding;\, \Delta, cc)}{eff(embedding;\, \Delta, \text{peripheral})} \tag{3.3.2}$$

The fraction accounts for the efficiency loss in the mid-central and central collisions, while the NLO POWHEG simulation drives the underlying kinematic distributions. The embedded-simulation efficiency is calculated in 10% wide centrality bins, from 0 to 90%. In the formula, "peripheral" refers to the efficiency computed in the most peripheral centrality bin. Mixing two independent simulations leads to an increase in the uncertainty of the combined value. Another strategy would be to use POWHEG only as a sanity check of the Pythia embedded simulation. Nevertheless we prefer to keep POWHEG as a baseline since, at the end, the smaller is our uncertainty on the agreement between POWHEG and peripheral-Pythia the smaller is the uncertainty that we add in the final result by means of formula (3.3.2).

3.3.3 Alignment and resolution correction

The alignment of the muon chambers is an essential ingredient for a good reconstruction resolution during data taking. The spatial position of the detection elements being well reproduced in the Monte Carlo is equally important. Any detector misalignment leads to a worsening of the Z boson peak resolution as well as to a bad efficiency estimation. This is mainly true because of the invariant mass selection. If the simulation doesn't reproduce the width and the tails of the distribution (the Drell-Yan shape on the left-hand side in particularly important), the number of reconstructed dimuons falling in the $60 < m_{\mu\mu} < 120\,\mathrm{GeV}/c^2$ window is improperly estimated, leading to a wrong value of the efficiency according to formula (3.3.1). During data taking, dedicated runs are taken with and without the presence of the magnetic field to correct the position of the detector elements in the ALICE condition database.[3] Thanks to the alignment procedure, a set of parameters is obtained and tuned such that the χ^2 of the fitted tracks is minimized. In principle, the procedure should involve the six degrees of freedom of each of the 156 detector elements. To face the problem, some approximations are used through an iterative procedure. The measured misalignment after each iteration is used to update the geometry of the detector that becomes the input for the following iteration [82]. The best-fit alignment parameters are finally saved for each period in the ALICE condition database and the MC simulations are anchored to them.

Together with the alignment, the parameterization of the track residuals resolution of the tracking chambers (distance between the cluster position and the track to which the cluster is attached during the reconstruction) is important to reproduce the Z boson invariant mass peak well and, consequently, to properly compute the efficiency. During the periods here analyzed, a mismatch between the resolution measured in the data and the one reproduced by the Monte Carlo has been measured. This is due to both a bad cluster resolution parameterization (more precisely, a better resolution of the MC than the real data) and a residual misalignment problem. To account for them a procedure was implemented and used to correct the standard GEANT reconstruction.

Cluster resolution During the reconstruction, the detector response is simulated with a Mathieson-function-based expression [90] as sketched in section 2.3.4. The resulting distribution for the cluster-track residuals has a bell shape which turns out to be different from the measured one. To correct this, a smearing of the

[3] Data taken without magnetic field allow the alignment of the tracking chambers with straight tracks based on the MILLEPEDE algorithm [110]. An array of optical sensors also monitors the relative displacements of the chambers.

tracks is implemented which replaces the response of the detector. The smearing task includes an estimate of the energy loss and Coulomb scattering in the front absorber, of the scattering in the tracking chambers and of the spatial chamber resolution. It uses a parameterization of the cluster resolution obtained by fitting the cluster residuals from data. This parameterization is used to smear the track kinematics: the task loops over the reconstructed tracks, recovers the corresponding MC particles, computes the smeared variables and replaces the reconstructed kinematics with the smeared one. The set of smearing parameters is tuned on the data cluster resolution, which is mimicked with a Crystal Ball function (eq. 3.2.2). The resulting invariant mass shape of the reconstructed Z boson muons is shown in figure 3.12. In the left panel the distribution is compared with the one provided by the standard reconstruction, while on the right the measured distribution is also shown and quantitatively compared to the Monte Carlo predictions.

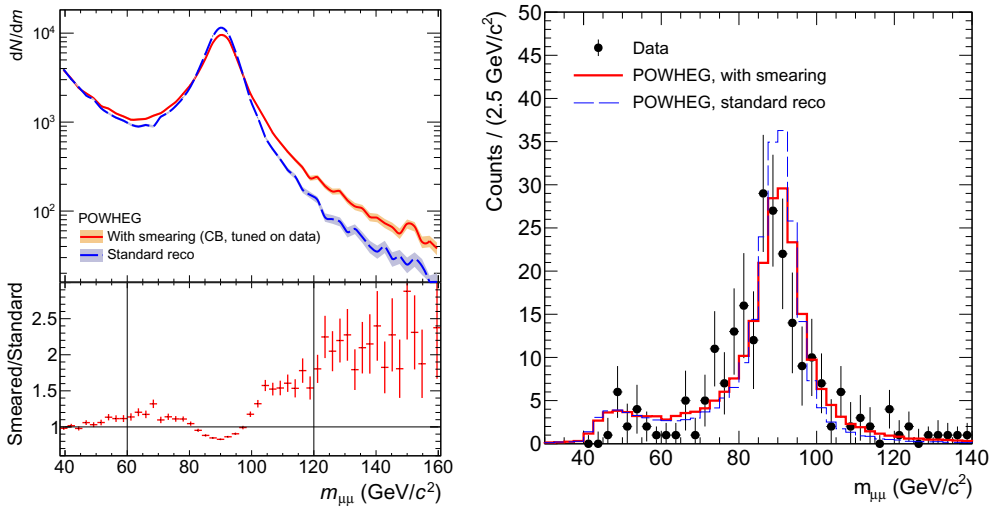

Figure 3.12. Left: Comparison between the reconstructed Z boson peak with the standard reconstruction and with the smeared Monte Carlo. In the latter, the cluster resolution is parameterized by a Crystal Ball function tuned on data. **Right:** Both simulations are compared with the measured invariant mass distribution. The $p_{T,\mu}$ and η_μ fiducial cuts are applied. The Monte Carlo is normalized to the number of candidates in the interval $m_{\mu\mu} \in [60, 120\,\mathrm{GeV}/c^2]$. The reduced χ^2 between data and Monte Carlo is $\chi^2/\mathrm{ndf} = 47.9/13$ for the standard reconstruction simulation and $\chi^2/\mathrm{ndf} = 19.3/13$ for the smeared simulation (p-value $\simeq 0.12$). ⋆THIS THESIS⋆

The smearing task is only an approximate solution to correct for the Monte Carlo inaccuracy. Even if it provides good results, the related systematic uncertainty is the one driving the full systematic of the analysis, as will be detailed in section 3.4.4.

Misalignment The alignment parameters stored offline account for the relative displacement between the chamber elements. Nevertheless, during data taking a global displacement has to be taken into account. This is actually proved to be necessary for the 2018 periods, as it results from figure 3.13. For each unlike-sign muon pair (without $p_{T,\mu}$ and $m_{\mu\mu}$ selections), it shows the correlation between the invariant mass and the transverse momentum of each muon, split in the two periods with different B-field polarity. The projections on the $p_{T,\mu}$ axes are drawn in the bottom panels. It is clear that for events at higher mass (namely, at higher p_T) positive and negative muons are reconstructed on average with different transverse momentum.

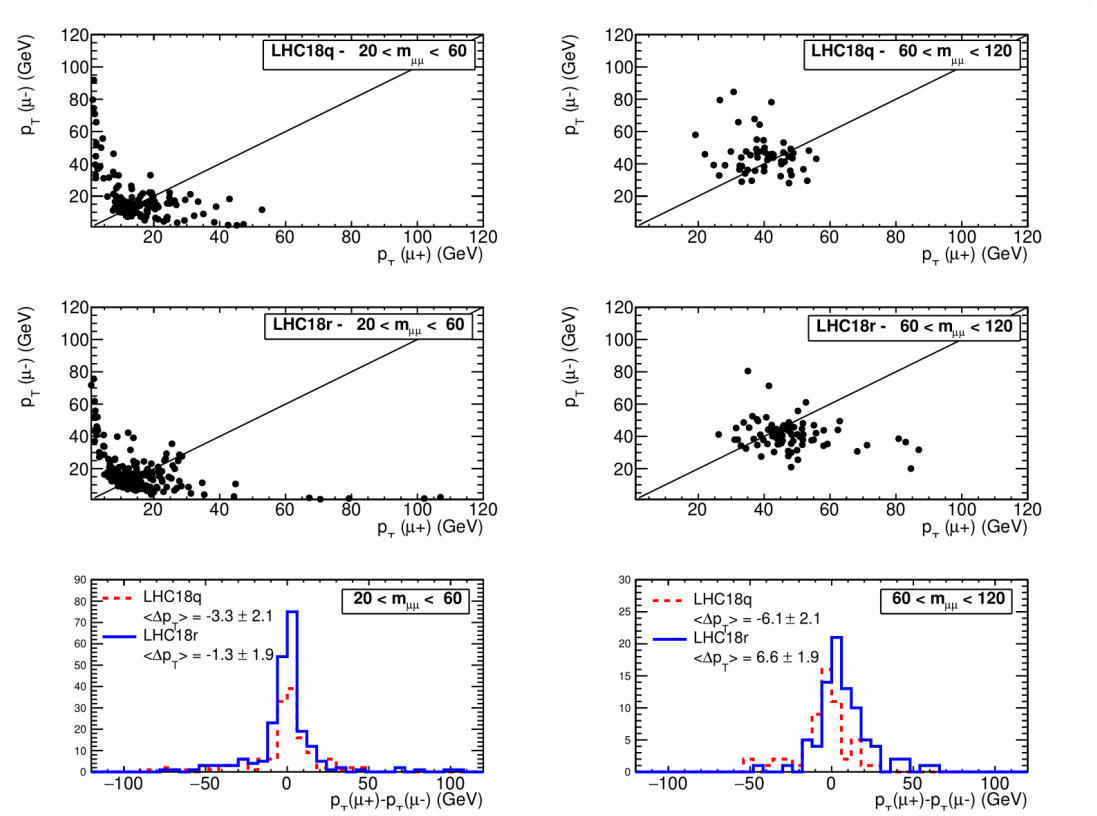

Figure 3.13. **First row:** p_T of negative and positive tracks for the muon pairs with invariant mass below (on the left) and above (on the right) $60\,\mathrm{GeV}/c^2$, reconstructed in the 2018 sub-period with given magnetic field polarity. **Second row:** The same, for the period with opposite magnetic field. The diagonal line is drawn to highlight the asymmetry between positive and negative tracks. **Last row:** Distribution of the difference between transverse momentum of positive and negative tracks. The distributions from the two periods are overlapped. A sizable shift for high-p_T muons is measured and found to be consistent between the two periods. ⋆THIS THESIS⋆

Similarly, figure 3.14 displays the p_{T} dependence of the double ratio

$$\frac{\mu^+(B+)/\mu^-(B+)}{\mu^+(B-)/\mu^-(B-)} \tag{3.3.3}$$

where $B+$ and $B-$ correspond to the opposite B-field polarity periods LHC18q and LHC18r. Independently on the source of the muons, this quantity should be equal to one. A deviation from unity is caused by the detector, in particular through (i) a different efficiency for μ^+ and μ^- or (ii) a misalignment of the detector. Given the high transverse momentum of the muons of this analysis, option (ii) is preferred.

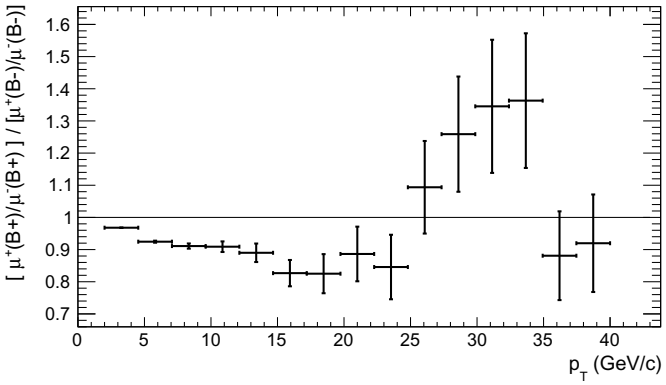

Figure 3.14. The observable described in eq. (3.3.3) as a function of $p_{\mathrm{T},\mu}$. The figure shows that the asymmetry between positive and negative muons depends on the direction of the magnetic field. To account for this in the simulation, a systematic shift on the bending angle of the tracks is added. ⋆THIS THESIS⋆

Such shifts justify the introduction of a correction in the analysis of the tracks position. The correction consists in a systematic shift on the inverse of the muon momentum or equivalently on the deviation angle θ of the tracks, which is proportional to $1/p_\mu$. The shift is parameterized by

$$\Delta\theta = q \cdot n_\sigma \cdot \sigma_\theta \tag{3.3.4}$$

where q is the charge of the track, σ_θ is the resolution on the deviation angle (about 8×10^{-5}) and n_σ is the parameter to be tuned. The parameter is tuned on the mean value of $p_{\mathrm{T},\mu}$ shift presented before, only for the muons reconstructed as coming from the Z boson . The measured values are reported below, also for

the 2015 period to show that in such case the correction is unnecessary.

$$\begin{aligned} &2015: && \langle \Delta p_{\mathrm{T}} \rangle = 0.8 \pm 2.2\,\mathrm{GeV}/c && \langle \Delta p \rangle = 66 \pm 47\,\mathrm{GeV}/c \\ &2018: && \langle \Delta p_{\mathrm{T}} \rangle = 6.1 \pm 1.3\,\mathrm{GeV}/c && \langle \Delta p \rangle = 60 \pm 27\,\mathrm{GeV}/c \end{aligned}$$

$$\text{with } \langle \Delta p_{\mathrm{T}} \rangle \equiv \langle\, \mathrm{sign}(B_x)\, [\, p_{\mathrm{T}}(\mu^+) - p_{\mathrm{T}}(\mu^-)\,]\,\rangle$$

The absolute value of the shift is found to be consistent between LHC18q and LHC18r and the two periods are merged to increase the statistical precision. The comparison between data and simulation with different tuning parameters is shown in figure 3.15. The best value is the one that makes the Monte Carlo $p_{\mathrm{T},\mu}$ shift equal to 6.1 GeV/c.

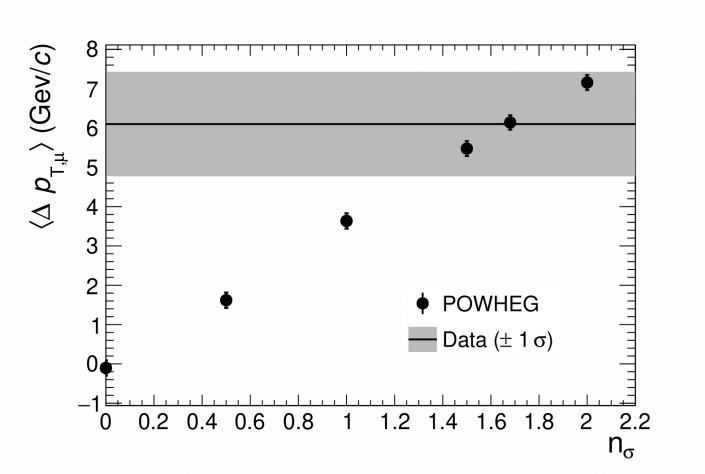

Figure 3.15. Difference between the mean value of $p_{\mathrm{T}}(\mu^+)$ and $p_{\mathrm{T}}(\mu^-)$ distributions measured in data and reconstructed with POWHEG simulation with different values of the shift parameter n_σ (eq. 3.3.4). The measurement and the simulation refer to the full 2018 data sample. Only muons used for the Z boson signal extraction are considered. The best value is $n_\sigma = 1.68$. ⋆THIS THESIS⋆

3.3.4 Final weighting

The procedure described so far provides the efficiency values as a function of the run number and the centrality class. The goal is to find an effective value $eff_{\,tot}$ which corrects the total number of reconstructed candidates N_{tot}^{raw}:

$$N_{tot}^{real} = \frac{N_{tot}^{raw}}{eff_{\,tot}}$$

Let's identify the i-th run or the i-th centrality bin by the subscript i. The real number of produced particles in each bin is linked to the measured (raw) number by $N_i^{real} = N_i^{raw}/eff_i$. The weighted efficiency can be expressed as follows.

$$N_{tot}^{real} = \sum_i N_i^{real} = \sum_i \frac{N_i^{raw}}{eff_i} = \frac{\sum_i N_i^{raw}}{eff_{tot}}$$

$$\frac{1}{eff_{tot}} = \frac{\sum_i \frac{1}{eff_i} N_i^{raw}}{\sum_i N_i^{raw}} \tag{3.3.5}$$

On the other hand, assuming to know the real number of produced particles, it is possible to weight on them.

$$N_{tot}^{raw} = \sum_i N_i^{real}\, eff_i = N_{tot}^{real}\, eff_{tot}$$

$$eff_{tot} = \frac{\sum_i eff_i\, N_i^{real}}{\sum_i N_i^{real}} \tag{3.3.6}$$

Computing the average according to N^{real} forces to rely on a model or an approximation, but the usage of formula (3.3.5) is impossible when the signal in some bins is so weak that only few (or even less than one) candidates are expected in each of them.

Run weighting The number of Z bosons per run is on average below unity and the weighted efficiency is computed assuming the production rate proportional to the number of triggered `CMUL` (opposite sign dimuons) events:

$$eff_{tot} = \frac{\sum_{r=run} eff_r\, N_r^{\texttt{CMUL}}}{\sum_r N_r^{\texttt{CMUL}}}$$

Centrality weighting The centrality distribution of the efficiency has to be averaged to compute eff for the 0-90% and 20-90% integrated bins. The number of reconstructed candidates in each centrality bin is quite small (two candidates in each of the most peripheral bins) and the theoretical number of binary nucleon-nucleon collisions N_{coll} is more reliable to this purpose. Apart from corrections due to centrality-dependent cold nuclear effects, such number is expected to be proportional to the number of produced Z bosons .

$$eff_{0-90\%} = \frac{\sum_{c=0-10\%}^{80-90\%} eff_c \langle N_{\text{coll}} \rangle_c}{\sum_{c=0-10\%}^{80-90\%} \langle N_{\text{coll}} \rangle_c} \tag{3.3.7}$$

$cc(\%)$	0-10	10-20	20-30	30-40	40-50	50-60	60-70	70-80	80-90
$\langle N_{\rm coll}\rangle$	1572	973.4	592.7	343.8	185.7	91.41	40.5	16.12	5.67

Table 3.4. Average number of nucleon-nucleon collisions in nine centrality classes from 0 to 90% according to Glauber Monte Carlo [11].

Formula (3.3.5) has also been tested, using the number of reconstructed candidates. The statistical error has been propagated in the following way. Nine poissonian distributions centered on the measured values have been assumed for N_i^{raw} (i = 0-10% to 10-90%) and the resulting probability densities for eff_{tot} have been simulated. Expressed as percentage, they have gaussian shape with mean and standard deviation given by $(68.96 \pm 0.25)\%$ and $(70.76 \pm 0.28)\%$ for the 0-90% and 20-90% centrality classes respectively. Such uncertainties are highly correlated to the statistical uncertainty on the raw number of candidates, so using these values to compute the final results is not trivial. Nevertheless, they serve as a check for formula (3.3.7) which provides the values $(68.83 \pm 0.20)\%$ and $(70.77 \pm 0.20)\%$ for 0-90% and 20-90% centrality classes. Therefore, we assume that the uncertainty related to the weighting formula is fully included in the systematics of the experiment and no other errors have to be added.

Rapidity dependence The embedding correction factor computed with the Pythia simulation depends on the rapidity, in the way displayed in figure 3.16. The efficiency in each rapidity bin is computed independently according to formula (3.3.2), with only the tracks reconstructed in that bin. In order to increase the statistical precision, the embedded-simulation peripheral efficiency is taken with all the collisions between 70% and 90% of centrality, instead of 80-90%. The efficiency in a large interval Δy depends on the shape of the production cross section according to

$$N^{real} = \int_{\Delta y} \frac{dN^{raw}}{dy} \frac{1}{eff(y)}\, dy$$

where, for analyses with a low number of events, dN/dy is necessarily taken from the Monte Carlo.[4] To improve the accuracy of the measurement, the efficiency for the integrated result ($2.5 < y_{\mu\mu} < 4$) has been computed by averaging the rapidity-dependence of formula (3.3.2) on the rapidity distribution generated by POWHEG.

The final integrated and differential efficiency values are reported in table 3.5.

[4] In case of very fine fully differential bins −if possible− the efficiency can be weighted according to formula (3.3.5) and the calculation is independent on the MC generator.

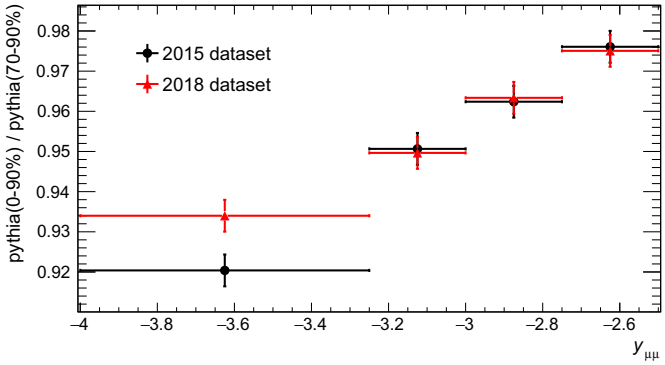

Figure 3.16. Rapidity dependence of the ratio between the efficiencies for the 0-90% centrality class and the 70-90% centrality class, computed with the embedded Pythia simulation. The rapidity is negative according to ALICE coordinate system. ⋆THIS THESIS⋆

Dimuon Rapidity	Centrality class	*eff* (%)
$2.5 < y < 4$	0-10%	67.10 ± 0.27
	10-20%	69.08 ± 0.27
	20-90%	70.77 ± 0.20
$2.5 < y < 4$	0-90%	68.83 ± 0.20
$2.50 < y < 2.75$	0-90%	72.21 ± 0.42
$2.75 < y < 3.00$		71.68 ± 0.27
$3.00 < y < 3.25$		67.19 ± 0.29
$3.25 < y < 4.00$		65.25 ± 0.38

Table 3.5. Final efficiencies. The quoted errors are partially correlated versus centrality by formula 3.3.2.

3.4 Systematic uncertainties

3.4.1 Background sources

The Z boson signal is extracted by counting the number of candidates in the fiducial region. This is justified by the very low amount of background. The invariant mass region $[60, 120\,\mathrm{GeV}/c^2]$ is chosen to reject most of virtual photon contribution even though it is still present and interferes with the Z production. This is not considered as background. The possible physical background sources are listed in the following.

- $Z \to \tau\tau \to \mu\mu$. The Feynman diagram at the tree-level of the process is drawn in figure 3.17. The branching ratios of Z boson decay into muons and tau leptons differ by 1‰, while the probability of $\tau \to \mu\,\nu_\mu\nu_\tau$ decay

is $\simeq$ 17% [20]. Nevertheless the background induced by this process is far below 17% because of the different kinematics of the final state muons, caused mainly by the energy-momentum carried by the unreconstructed neutrinos. In particular, muons are not produced back-to-back in the Z boson frame and the $p_{T,\mu}$ cut is more effective than on direct decay muons.

- $t\bar{t} \rightarrow \mu\mu$. The Feynman diagram at the tree-level of the semileptonic decay of top quarks is drawn in the right part of the same figure. The rapidity distribution of such lepton pairs is narrower than that of Z boson muons and this background source is suppressed at the rapidity covered by the ALICE spectrometer.

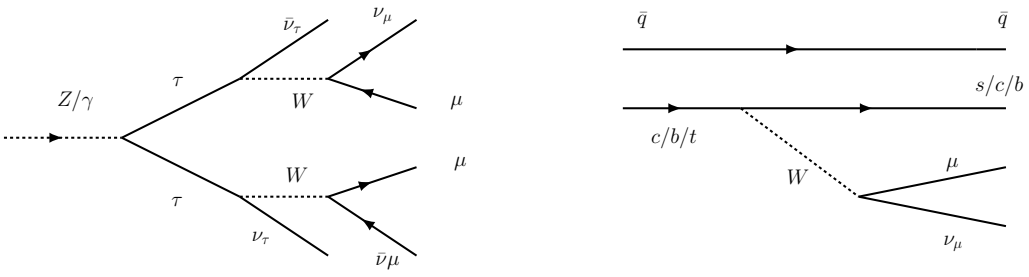

Figure 3.17. Feynman diagrams for the background processes. **Left:** Double lepton chain decay of Z boson , $Z \rightarrow \tau\tau \rightarrow \mu\mu$. **Right:** Semileptonic decay of top quark or heavy flavour (c, b) states.

The contamination of the processes described so far is estimated by the ratio between their cross sections in the fiducial region and the cross section of the $Z \rightarrow \mu\mu$ production. Both $Z \rightarrow \tau\tau \rightarrow \mu\mu$ and $t\bar{t} \rightarrow \mu\mu$ are simulated with POWHEG generator (see previous section) interfaced with Pythia. The simulations are normalized to the total cross section provided by POWHEG; the corresponding invariant mass distributions after the $-4 < \eta_\mu < -2.5$ and $p_{T,\mu} > 20\,\mathrm{GeV}/c$ selections are shown in figure 3.18. The number of muon pairs in the $[60, 120\,\mathrm{GeV}/c^2]$ invariant mass window is about 0.5% of the signal.

- D or $B \rightarrow X\mu\nu_\mu$. Finally, the semileptonic decay of heavy flavour bound states can contribute to the unlike-sign muon pairs spectrum. This contribution has been estimated in other analyses through simulations based on Pythia and on FONLL calculations [111]. When simulating nucleon-nucleon collisions, the background in the fiducial region of this analysis is below 1% of the signal. The corresponding contamination in lead-lead collisions at $\sqrt{s_{NN}} = 5$ TeV is expected to be even smaller due to the energy loss of heavy flavour hadrons in the hot medium [101].

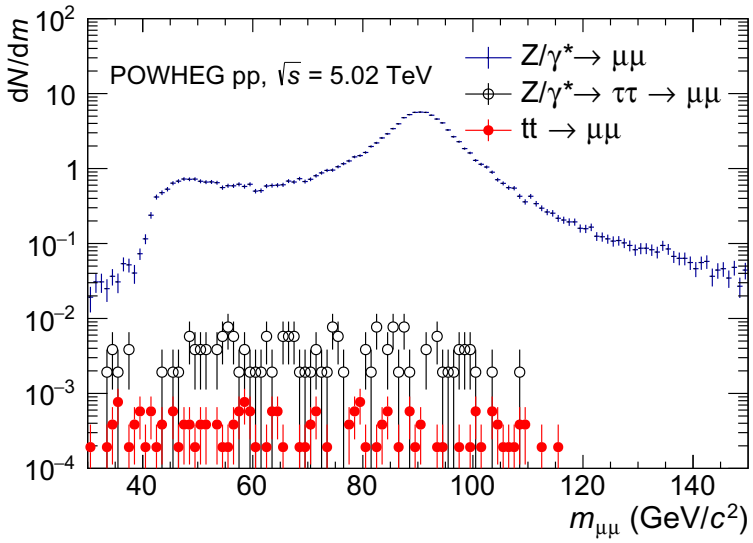

Figure 3.18. Invariant mass spectra of dimuons coming from $Z \to \mu\mu$, $Z \to \tau\tau \to \mu\mu$ and $t\bar{t} \to \mu\mu$ processes, in proton-proton collisions at 5.02 TeV. The $p_{T,\mu} > 20\,\mathrm{GeV}/c$ cut is applied. The signal distribution ($Z \to \mu\mu$) is normalized to have integral in $[60, 120\,\mathrm{GeV}/c^2]$ equal to 100. The other simulations are scaled according to the ratios of their cross sections. ⋆THIS THESIS⋆

To account for the background caused by such processes, a systematic uncertainty of 1% will be added to the signal extraction result.

3.4.2 Tracking efficiency

The reconstruction of tracks in the tracking system requires at least one reconstructed cluster in each of the first three stations, and at least three reconstructed clusters in the other two stations. The algorithm used to evaluate the efficiency of each station is quite simple and relies on the redundancy of the Multi-Wire-Proportional chambers. Each station contains two chambers; assuming the efficiency of each independent on the other, one can use the subset of events where the second chamber has fired to assess the efficiency of the first chamber, and vice-versa. Let's call n_1, n_2 and n_{12} the number of tracks which have a cluster reconstructed only in the first chamber, only in the second or in both chambers, respectively. Then, for each station the efficiency of the two chambers are

$$\epsilon_{st,1} = \frac{n_{12}}{n_{12} + n_2} \qquad \epsilon_{st,2} = \frac{n_{12}}{n_1 + n_{12}}$$

Consequently, the efficiency of each of the first tree stations is

$$\epsilon_{st=1,2,3} = 1 - (1 - \epsilon_{st,1})(1 - \epsilon_{st,2})$$

while the efficiency of the fourth+fifth stations, which are considered as a whole, is the sum of the probabilities of having exactly three or exactly four clusters in the four chambers (now we will use the chamber index $i = 1$ to $i = 4$ to group the two stations).

$$\epsilon_{st=45} = \sum_{i=1}^{4} \left[(1 - \epsilon_{st,i}) \prod_{j \neq i} \epsilon_{st,j} \right] + \prod_{i=1}^{4} \epsilon_{st,i}$$

Finally the efficiency of the tracking system is the product

$$\epsilon_{trk} = \prod_{st=1,2,3,45} \epsilon_{st}$$

The efficiency measured during 2018 datataking is above 90% for most of the runs. High voltage trips, electronic noise or other problems make the efficiency during some other runs lower, down to $\sim 80\%$. The simulation has to reproduce the correct efficiency. To assign an uncertainty to this factor, the efficiency is computed for the experimental data and for a MC data sample, and the difference is taken as systematic uncertainty. In figure 3.19 the rapidity dependence of ϵ_{trk} computed from a single-muon simulation is compared to that measured in the datataking period [112]. The non-constant shape indicates the presence of low efficient regions in the detector. In general, the shape of the measured efficiency in data is well reproduced by the simulation. Looking at the relative difference in the magnitude, a systematic of 1.5% is estimated. For the dimuon event-topology, considering the muons as independent, this leads to $1 - (98.5\%)^2 \simeq 3\%$ systematic uncertainty. No correlation has been found among the values measured in different rapidity intervals.

3.4.3 Trigger efficiency

The trigger response function, which is the probability of triggering on a given muon, depends on its transverse momentum in a non-trivial way since the muon p_{T} cut on which the trigger is based is not sharp (see section 2.3.4). Independently on the trigger threshold, the response function reaches a *plateau* for muons with p_{T} beyond $\sim 6\,\mathrm{GeV}/c$. The kinematic region of this analysis is fully included in this range.

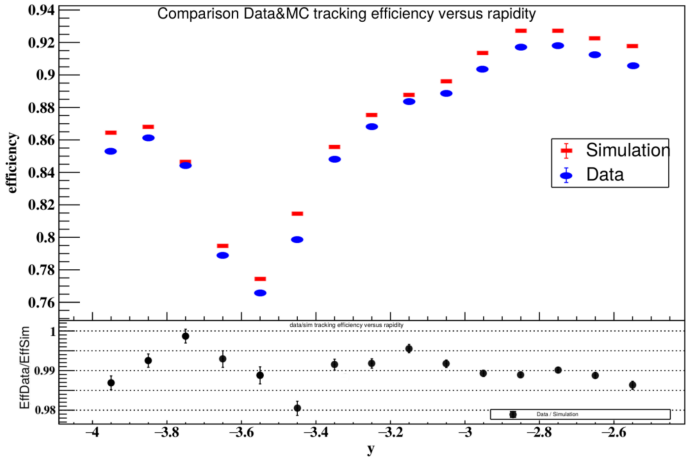

Figure 3.19. Tracking efficiency from single muons computed with the method described in the text, as a function of rapidity (negative according to ALICE coordinate system). Comparison between real and simulated data [112].

The value of the *plateau* depends on the intrinsic efficiency of the RPCs, which is calculated from the data in a similar way as described for the tracking chambers. There are 72 RPC planes; 234 boards on each plane can produce a trigger signal. The efficiency algorithm provides a map of the efficiencies associated to each of the local boards. The map is then stored offline and used in the Monte Carlo to simulate the detector's response. To evaluate the uncertainty on these values, the efficiencies are computed with different sets of tracks, which are obtained by changing their selection (the muon p_{T} cut, the tracker/trigger matching criteria, ...). A new efficiency map is then built by using the track selection that provides the largest difference with the standard map, local board by local board. The modified map is finally used in the Monte Carlo to evaluate a new global efficiency, whose difference w.r.t. the standard one is taken as systematic uncertainty. The discrepancy between the integrated efficiencies computed with the standard and modified maps amounts to $\sim$ 1% for the 2018 dataset and to 1.5% for 2015. The value 1.5% is taken as global systematic associated to the trigger efficiency uncertainty.

Finally, the efficiency of the matching algorithm between trigger and tracking systems is source of uncertainty. This is done during the quality assurance of the recorded data by varying the χ^2 cut of the matching criteria. This brings to a 0.5% uncertainty at the single muon level, meaning 1% on the dimuons.

3.4.4 Monte Carlo resolution and alignment

The procedure (named "smearing task") which addresses to the mismatch between data and MC resolution is described at page 69. It exploits an approximation which replaces the simulation of the particle propagation through the detector. In particular, the resolution of clusters in the chambers is parameterized with a Crystal Ball (CB) function fitted on the measured cluster-track residual distribution. To evaluate the reliability of this method, it can be tested on the simulation itself. Furthermore, different shapes for the residuals can be used.

Figure 3.20 shows the effect of changing the CB parameterization with a gaussian one. To produce the plot shown in the left panel, the resolution has been fitted with a gaussian function tuned on the residual distribution reproduced by the Monte Carlo. The resulting invariant mass peak is too narrow, meaning that the gaussian parameterization introduces a significant bias. The parameterization with CB tails is much more reliable, as one can see in the right panel of the figure. Here the smearing task uses a CB function; if it is fitted on the Monte Carlo cluster-track residuals, the outcome is very close to the full reconstruction result. On the efficiency level, the simulations with full reconstruction and with smearing task (CB tuned on MC) differ by 4‰ (figure 3.23).

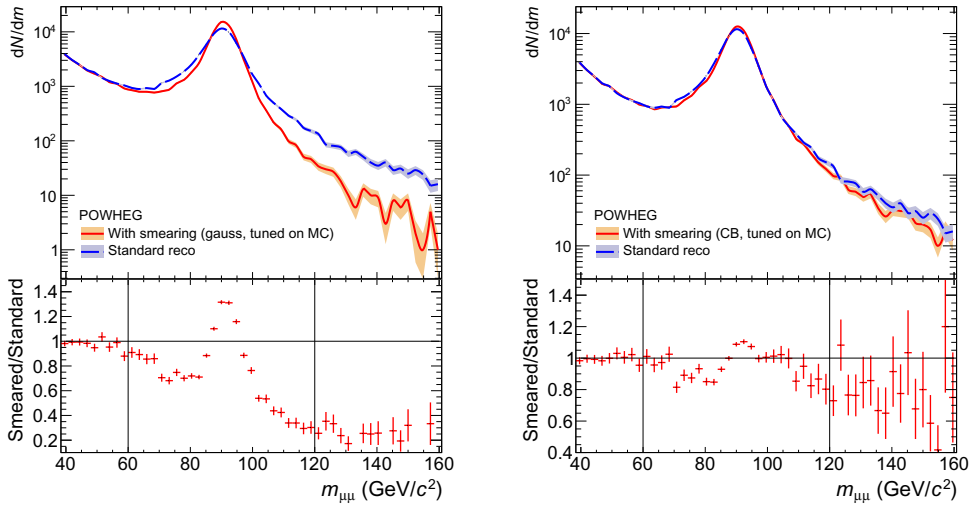

Figure 3.20. Effect of different cluster resolution tuning on the invariant mass spectrum of reconstructed dimuons. **Left:** Comparison between standard reconstruction and smeared simulation with cluster resolution parameterized with a gaussian function tuned on the Monte Carlo. **Right:** Comparison between standard reconstruction and smeared simulation with Crystal Ball parameterization tuned on Monte Carlo. ⋆THIS THESIS⋆

Also the error induced by the shift in $1/p_\mu$ must be evaluated. In the simulation of the 2018 dataset the deviation angle θ inside the magnetic field of each track has been shifted by a quantity equal to $n_\sigma = 1.68$ times the resolution on θ. The best fit has been obtained as explained at page 71. The uncertainty related to the fit can be assessed with figure 3.15, by varying the parameter n_σ in a range covering a 68% confidence level interval on the measured p_T shift. The efficiencies computed with $n_\sigma = 1.2$ and $n_\sigma = 2.1$ are reported in figure 3.23. The third bin of the figure displays also the efficiency obtained without shift ($n_\sigma = 0$). The impact of the shift tuning on the efficiency turns out to be negligible with respect to the smearing of the resolution. The invariant mass peaks reproduced with and without shift are drawn and compared in figure 3.21.

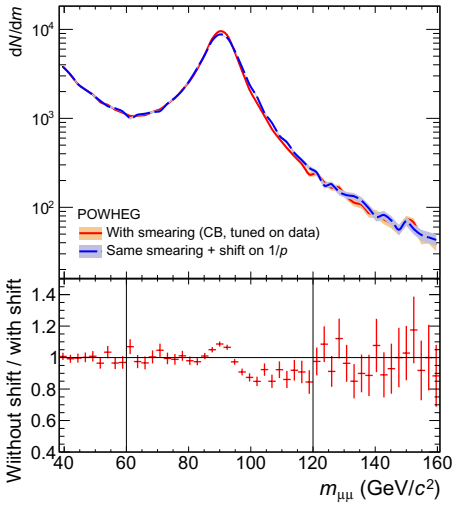

Figure 3.21. Effect of the shift on $1/p_\mu$ (or on the bending angle) on the invariant mass spectrum. In both cases the simulation is smeared with Crystal Ball tails tuned on data. ⋆THIS THESIS⋆

The good outcome of the comparison between full reconstruction and MC-tuned smearing task (once the Crystal Ball is chosen, as in the right panel of figure 3.20), validates the strategy of using the smeared simulation to compute central values of the efficiency. Nevertheless it remains an *ad hoc* correction to the MC inefficiency. The input cluster resolution is one of the main sources of error. For example, the method uses a cluster-residual distribution integrated over all clusters, not taking into account the variations of the resolution among chambers or among the detection elements in the chambers, which is exemplified in figure 3.22 [113]. In particular, we should consider that elements at different distances from the beam affect the results at different rapidities. Since an averaged resolu-

tion is used, the precision of the smearing task is worse on the rapidity-dependent results than on the integrated ones.

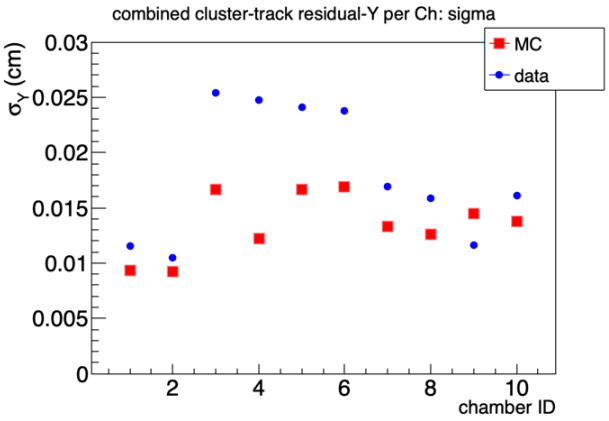

Figure 3.22. Cluster resolution along y measured on the different tracking chambers. The values are extracted by fitting both the data and MC distributions. The discrepancy between data and MC justifies the introduction of the smearing task. [113].

A reliable estimate of the error induced by the smearing is achieved by comparing the full reconstruction and the smeared one fitted on data. Such discrepancy quantifies the uncertainties inside the simulation. Figure 3.23 summarizes the situation. The impact of the shift on $1/p_\mu$ is almost negligible, while the discrepancy between full reconstruction and smeared data-tuned simulation (with the best-fit shift) is 5%. The plot shows the 2018 period only to highlight the effect of the shift, but the same conclusion holds for the full dataset. This value will be taken as systematic uncertainty.

3.4.5 Centrality determination

The centrality is determined by slicing the V0 amplitude spectrum as explained in sections 1.2.3 and 3.1.2. The anchor point in Pb-Pb collisions is set to the detector pulse height corresponding to the 90% of the total hadronic cross section and it is known with a 0.5% uncertainty. For systematic studies, other two centrality estimators are implemented, called V0Mplus05 and V0Mminus05. They are obtained by moving the anchor point by $\pm 0.5\%$ and recalculating the centrality intervals boundaries accordingly. Table 3.6 shows the signal extraction and the number of Minimum Bias (MB) events computed with the two estimators.

The Z boson yield is computed by dividing the Z signal by the number of MB. The number of MB is obtained as the number of `CMUL` triggered events multiplied by the normalization factor F_{norm}. Because of the flatness of the MB distribution

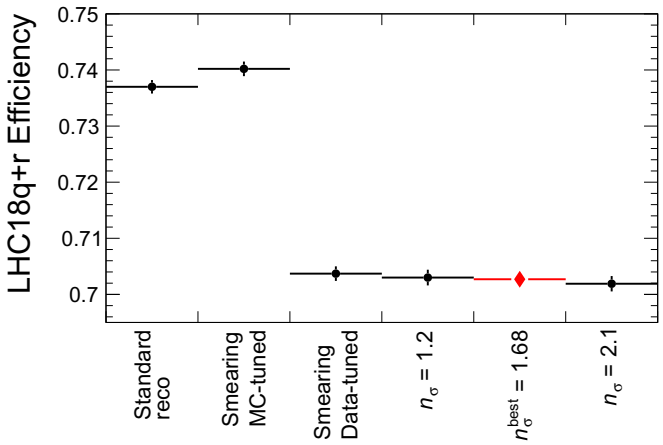

Figure 3.23. Effect of the smearing task and of the $1/p$ shift on the efficiency. The configuration chosen as central value for the final results is highlighted with a diamond. The difference between its value and the *eff* from simulation without smearing (first bin) amounts to 5% and is chosen as systematic uncertainty. ⋆THIS THESIS⋆

versus centrality, the yield in finer intervals can be calculated using the number of MB in 0-90% scaled proportionally to the bin width. According to this scaling, the relative uncertainty on the number of MB in each bin is equal to that in 0-90%. The magnitude of such error ($\sim$ 0.6%) is comparable with the relative error on the signal extracted using different centrality estimators. For this reason as well as to obtain a systematic fully uncorrelated versus centrality, the normalization factor is re-computed in each bin when comparing V0Mplus05 and V0Mminus05. The procedure differs from that described in section 3.1.1 only by the selection of the events which are required to belong to the centrality class under study.

The final systematic uncertainty is defined, for each bin, as half of the difference between the yields (N_Z/N_{MB}) extracted with V0Mplus05 and V0Mminus05. The full difference is reported in the last column of table 3.6.

Centrality	Z raw signal		Million of MB		Rel. diff. in N_Z/N_{MB}
	V0M+05	V0M−05	V0M+05	V0M−05	
0-90%	208	208	5157.58	5190.43	-0.6%
0-10%	71	72	572.72	579.12	0.3%
10-20%	63	63	573.00	579.39	-1.1%
20-90%	74	73	4012.37	4032.40	-1.8%

Table 3.6. Comparison of the signal and number of MB events measured with the V0Mplus05 and V0Mminus05 centrality estimators.

3.4.6 Other (negligible) systematic uncertainties and summary

Fiducial cuts

The error on the single muon p_{T} selection is driven by the resolution of the detector, which at 20 GeV/c is 4% [81]. The systematic on this selection is evaluated by studying the variation of the quantity

$$\frac{N_Z^{raw}(\mathrm{cut} = p_{\mathrm{T}}^{cut})}{eff(p_{\mathrm{T}}^{cut})} \tag{3.4.1}$$

in a range of p_{T}^{cut} covering the experimental resolution, i.e. between 19 and 21 GeV/c. Here, $eff(p_{\mathrm{T}}^{cut})$ is the efficiency for an analysis where the $p_{\mathrm{T},\mu}$ cut is set to p_{T}^{cut}:

$$eff(p_{\mathrm{T}}^{cut}) = \left.\frac{N_{reco}(\mathrm{cut} = p_{\mathrm{T}}^{cut})}{N_{gen}(\mathrm{cut} = 20\,\mathrm{GeV}/c)}\right|_{\text{Monte Carlo}}$$

The influence of the $p_{\mathrm{T},\mu}$ cut on the signal extraction is shown in the left panel of figure 3.24, while the right panel displays the number of candidates corrected for the efficiency computed with the smeared simulation (formula 3.4.1). The RMSE of the values between 19 and 21 GeV/c^2 is less than 0.5% of the central value and the fluctuations are driven by the low statistics. Similar conclusions hold for the invariant mass selection. According to these studies, the effect of the resolution on the fiducial cuts is neglected.

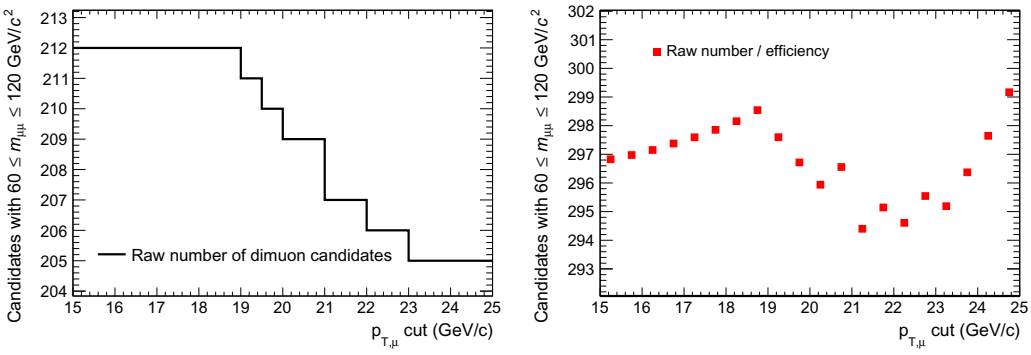

Figure 3.24. Signal extraction as a function of the single muon p_{T} cut. **Left:** Raw signal. **Right:** Signal corrected for the corresponding efficiency (the fiducial cut is always set to $p_{\mathrm{T},\mu} > 20\,\mathrm{GeV}/c$). ⋆THIS THESIS⋆

Monte Carlo inputs

When the PDF/nPDF set used for the particle generation is changed, the shapes of the lepton transverse momentum and rapidity change. This in principle would lead to a different efficiency, giving a non-negligible systematic uncertainty. This happens when the analysis is performed in a kinematic regime sensitive to this change but not in the case discussed here. First of all, the efficiency of this analysis doesn't depend strongly on the muon p_{T}. Secondly, it has been proved that the modification of the shape is small in the rather limited fiducial region. As a consequence, no effect on the efficiency calculation by changing the PDF sets is measured. This is confirmed by the other published weak boson analyses [67, 69, 76]. Similarly, the efficiency doesn't change when simulations exploiting GEANT3 and GEANT4 are compared. No systematic uncertainty has to be added related to the Monte Carlo inputs and transport code.

Summary

Source	Relative uncertainty (%)	
Background contamination	1.0	
Tracking efficiency	3.0	ⓒ
Trigger efficiency	1.5	ⓒ
Trigger/tracker matching	1.0	ⓒ
Alignment (simulation smearing)	5.0	ⓒ
Normalization factor	0.5	ⓨⓒ
Centrality estimation	0.2 – 0.9	ⓨ
$\langle T_{\mathrm{AA}} \rangle$	0.7 – 1.5	ⓨ
pp cross section	3.5 – 5.0	ⓒ
Total (normalized yield)	6.3	
Total (R_{AA})	7.4	

Table 3.7. Components of the relative systematic uncertainties on the Z boson yield and R_{AA} . The symbols indicate that the uncertainty is correlated versus rapidity (ⓨ) or centrality (ⓒ) . The total lines report the cumulative systematic uncertainty on the rapidity- and centrality-integrated result, taken as the quadratic sum of all the sources.

Table 3.7 summarizes the systematic uncertainties of the analysis, discussed in this section. The correlation versus rapidity or event centrality is highlighted. A certain degree of correlation can be assumed between the alignment uncertainty and the Z boson rapidity, even if a precise estimate has not been possible. The table includes also uncertainties on $\langle T_{\mathrm{AA}} \rangle$ and proton-proton cross section, which are actually a source of uncertainty on the yield and R_{AA} results. T_{AA} is computed as a function of the collision impact parameter with a Glauber MC, as explained

in section 1.2.1. The computation relies on many input parameters, namely the parameters of the Fermi distribution describing the nucleus density profile, the nucleon-nucleon cross section, and the parameters of the negative binomial distribution used to simulate the event multiplicity. The latter uncertainties are directly obtained by fitting the distribution on the measured V0 signal. The uncertainties on the Glauber MC values (in particular, $\langle T_{\mathrm{AA}} \rangle$) are then derived by varying the parameters of the model within their uncertainty and repeating the fit for each variation. Finally, the 0.5% uncertainty assigned to the normalization factor is explained at page 55.

3.5 Results of Z boson production in Pb-Pb collisions at $\sqrt{s_{\mathrm{NN}}} = 5.02$ TeV

In this section the production rate of the process $Z/\gamma^* \rightarrow \mu\mu$ in the fiducial volume is presented in the form of normalized yield. The yield is defined as the average number of events produced in each lead-lead inelastic interaction. Experimentally, the number of interactions is counted as the number of minimum bias (MB) events. The raw number of events must be corrected for the averaged efficiency reported on page 76.

$$Yield = \frac{N_{\mathrm{Z}}}{eff \times N_{\mathrm{MB}}}$$

We summarize the fiducial cuts chosen for this analysis:

$$\begin{cases} -4 < \eta_{\mu} < -2.5 \\ p_{\mathrm{T},\mu} > 20\,\mathrm{GeV}/c \\ 60 < m_{\mu\mu} < 120\,\mathrm{GeV}/c^2 \end{cases} \tag{3.5.1}$$

The results are both integrated and differential versus rapidity. The collected statistics allow us to compute meaningful results in four dimuon rapidity bins. The following ones are chosen.[5]

$$\begin{aligned} 2.50 < y_{\mu\mu} < 2.75 \\ 2.75 < y_{\mu\mu} < 3 \\ 3 < y_{\mu\mu} < 3.25 \\ 3.25 < y_{\mu\mu} < 4 \end{aligned}$$

[5] Remember that the dimuon rapidity is given as positive by convention.

The production is then studied versus centrality and the yield is computed in the three intervals 0-10%, 10-20% and 20-90%. The number of candidates measured in each bin can be read in the table at page 63. To account for the centrality dependence, the yield is normalized by the average nuclear overlap function $\langle T_{AA} \rangle$. Being it proportional to the average number of binary nucleon-nucleon collisions $\langle N_{coll} \rangle$, normalizing an hard-process rate by $\langle T_{AA} \rangle$ almost removes its centrality dependence. Any further remaining shape is due to a non-exact N_{coll} scaling and in particular to a possible dependence of the nuclear PDFs on the radial position inside the nucleus. To summarize, the following plots will show the rapidity- or centrality-dependence of the normalized yield

$$\boxed{\frac{dN/dy}{\langle T_{AA} \rangle} = \frac{N_Z}{\langle T_{AA} \rangle \, eff \, N_{MB} \, \Delta y}} \tag{3.5.2}$$

The values of the average nuclear overlap function, the average number of participant nucleons and of binary collisions are listed for the relevant centrality classes in table 3.8. They are extracted with a Glauber MC as described in section 1.2.3.

centrality	$\langle T_{AA} \rangle (\mathrm{mb}^{-1})$	$\langle N_{coll} \rangle$	$\langle N_{part} \rangle$
0-90%	6.28 ± 0.07 (1.0%)	424.6 ± 5.5	125.9
0-10%	23.26 ± 0.17 (0.7%)	1572 ± 17.4	357.3
10-20%	14.40 ± 0.13 (0.9%)	973.4 ± 11.3	262
20-90%	2.70 ± 0.04 (1.5%)	182.3 ± 3.0	73.4

Table 3.8. Mean values for nuclear overlap function T_{AA}, number of nucleon-nucleon collisions N_{coll} and number of participants N_{part}. The uncertainty on $\langle N_{part} \rangle$ is less than 1% and is not reported.

The normalized yield may be thought of as an average nucleon-nucleon cross section. Dividing it by the proton-proton cross section of the same process at the same nucleon-nucleon center-of-mass energy one can assess the nuclear modification factor. It is defined as

$$\boxed{R_{AA} = \frac{dN/dy}{\langle T_{AA} \rangle \, d\sigma_{pp}/dy}} \tag{3.5.3}$$

It should be noticed the mismatch of the averaged flavour content (isospin) between the lead nucleus and the proton. Because of the different proton-proton, neutron-neutron and proton-neutron cross sections, R_{AA} is supposed to differ from unity even in the absence of nuclear modifications. This can be taken into account when computing theoretical predictions which are compared to the experimental values of eq. (3.5.3). ALICE didn't collect enough proton-proton lumi-

nosity to measure the Z boson production cross section. Using results from other experiments would require extrapolations that cause significant biases because of the different kinematic fiducial regions. For these reasons, our σ_{pp} reference is computed using a pQCD calculation based on CT14 NLO PDFs [42]. The resulting values are listed for the relevant rapidity intervals in table 3.9.

Δy	$\int_{\Delta y}(d\sigma_{pp}/dy)\,dy$ (pb)
$2.5 < y_{\mu\mu} < 4$	11.92 ± 0.46 (3.9%)
$2.50 < y_{\mu\mu} < 2.75$	1.69 ± 0.06 (3.5%)
$2.75 < y_{\mu\mu} < 3.00$	3.86 ± 0.14 (3.7%)
$3.00 < y_{\mu\mu} < 3.25$	3.99 ± 0.16 (4.0%)
$3.25 < y_{\mu\mu} < 4.00$	2.38 ± 0.12 (5.0%)

Table 3.9. Values for the $Z/\gamma^* \rightarrow \mu\mu$ production cross in proton-proton collisions at $\sqrt{s}$ =5.02 TeV.

The main goal of the analysis is to provide data points that can be included in the nPDFs global fits. Parton distributions are usually studied versus an energy scale Q^2 and the Bjorken variable x. Drell-Yan production in the resonant Z boson region can provide constraint at $Q^2 = M_Z^2$ ($\simeq 8.3 \cdot 10^3\,\mathrm{GeV}^2$). The Bjorken-$x$ ranges investigated by ALICE are close to the boundaries of the spectrum. The relation between the x value of the partons which annihilate and the rapidity y of the dimuons can be obtained at the leading order in the parton collinear approximation in the following way (figure 3.25). Let's call x_1 and x_2 the fraction of momenta of the colliding hadrons carried by the partons, and let E be the energy of each hadron. In the symmetric collision under study, $E = \sqrt{s_{\mathrm{NN}}}/2 = 2.51$ TeV. The nucleon mass can be neglected. The four-momentum carried by the gauge boson is

$$q \equiv (q_0, 0, 0, q_z) = ((x_1 + x_2)E, 0, 0, (x_1 - x_2)E)$$

For on-shell Z bosons , the kinematic of the process is fixed by the boson rapidity:

$$y = \frac{1}{2}\log\frac{q_0 + q_z}{q_0 - q_z} = \frac{1}{2}\log\frac{x_1}{x_2} \qquad \text{and} \qquad q^2 = M_Z^2 = x_1 x_2\,(2E)^2$$

So that the Bjorken-x of the involved partons are:

$$x_1 = \frac{M_Z}{\sqrt{s_{\mathrm{NN}}}}\,e^{y} \quad , \quad x_2 = \frac{M_Z}{\sqrt{s_{\mathrm{NN}}}}\,e^{-y} \tag{3.5.4}$$

At the energy of 5.02 TeV, $M_Z/\sqrt{s_{\mathrm{NN}}} \simeq 0.018$. The conversion between $y \equiv y_{\mu\mu}$ and $x_{1,2}$ is displayed in figure 3.26, still according to the leading order calcula-

tion. The forward Z boson production requires an interaction between a high-x parton and a low-x parton. Two completely different regions are involved simultaneously, one dominated by valence quarks (high x) and one by sea quarks (low x).

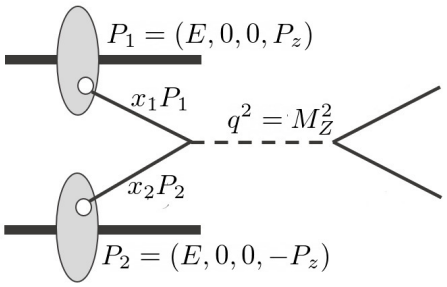

Figure 3.25. Tree-level diagram for the Drell-Yan process $q\bar{q} \rightarrow \mu^+\mu^-$.

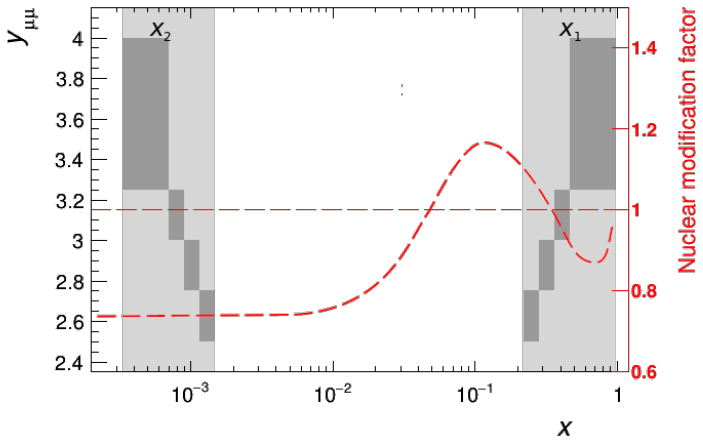

Figure 3.26. Qualitative relation between dimuon rapidity, Bjorken-x of the parton in the nucleus and nuclear effect. The vertical grey bands highlight the x regions accessible by ALICE with Z boson production in Pb-Pb collisions at 5.02 TeV. They are split further in the four rapidity bins chosen for this analysis (dark grey boxes, referring to the left vertical axis). The relation between x and $y_{\mu\mu}$ is a leading-order approximation. The superimposed dashed red line (referring to the right vertical axis) displays the typical behavior of the nuclear modification factor to the PDFs of a quark.

3.5.1 Integrated results

The differential Z boson normalized yield (eq. 3.5.2) measured in the 0-90% centrality class and averaged in the full $2.5 < y_{\mu\mu} < 4$ rapidity interval is

$$\frac{dN/dy}{\langle T_{\rm AA}\rangle} = 6.1 \pm 0.4\,(\text{stat.}) \pm 0.4\,(\text{syst.})\ \text{pb}$$

The statistical uncertainty, which amounts to 7%, is due to the poissonian error on the 209 measured candidates (see page 63). In figure 3.27 the result is compared with another analysis published by ALICE [76] which is based on less than a third of the statistics analyzed here. The measurements are fully compatible with each other. The figure displays also the comparison with several pQCD calculations including or not including nuclear modification to the PDFs. CT14 [42], EPPS16 [49] and nCTEQ15 [48] are taken into account. The first and the second calculations utilize the MCFM (Monte Carlo for FeMtobarn processes) code [114], while nCTEQ15 uses the NNLO FEWZ (Fully Exclusive W and Z production) code [115]. An overview of the (n)PDF sets is given in section 1.4.2. The calculation without nuclear modification (CT14) predicts the value 8.36 ± 0.32 pb. Its deviation from the experiment,

$$\frac{\text{Norm.Yield}|_{\rm CT14} - \text{Norm.Yield}|_{data}}{\sqrt{(\text{stat.})^2 + (\text{syst.})^2 + \delta^2_{\rm CT14}}} = 3.4\,, \tag{3.5.5}$$

shows that a net nuclear effect is measured. Even if the real significance doesn't amount to 3.4σ, as will be discussed at page 99, **this is a strong evidence of nuclear modification, the strongest ever measured by ALICE with gauge bosons**. The measured suppression is a convolution between the shadowing effect carried by a low-x parton and the net nuclear effect probed by an high-x quark. The latter is in a kinematic region close to the boundary between antishadowing and EMC effects as sketched in figure 3.26 (the Fermi region is also not excluded, depending on the parton flavour and on the nPDF parameterization). The comparison with the Z boson results measured in p-Pb collisions at $\sqrt{s_{\rm NN}} = 8.16$ TeV allows to partially disentangle the high- and low-x regions. This is discussed in section 3.6.

On the other hand, all the nuclear PDF models agree with data within uncertainties. The error bands on the predictions include the uncertainties on the NLO calculation, as well as the uncertainties on the PDFs which are larger for those including nuclear effects. The EPPS16 parameterization is the one including the largest number of flavor degrees of freedom and this results in a large uncertainty. Together with EPPS16 the prediction from EPS09s nPDFs [59] is shown in

the figure (again with CT14 as baseline). Although this is an older parton distribution set, it is used here because it contains a centrality dependence, which is not provided by EPPS16. To better describe the comparison between data and the other nPDF predictions, one should consider that the normalized invariant yield measured in the 0-90% centrality class can be well considered as fully inclusive in centrality. The difference between 0-90% and 0-100% normalized yields is of the order of 1‰, therefore fully included in the experimental uncertainties (this is also discussed in section 3.5.3).

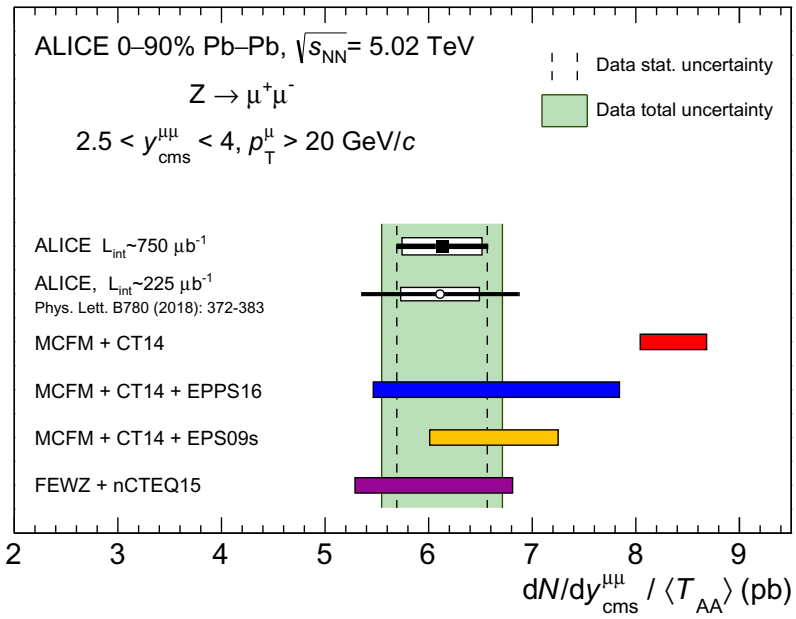

Figure 3.27. Yield of $Z/\gamma^* \rightarrow \mu^+\mu^-$ normalized by $\langle T_{AA} \rangle$ measured in Pb-Pb collisions at $\sqrt{s_{NN}} = 5.02$ TeV . The measurement presented in this work is the first data point on the top. The width of vertical dashed band corresponds to the statistical uncertainty, while the filled band is the sum in quadrature of statistical and systematic uncertainties. The colored filled boxes are different theoretical pQCD calculations. The first one (MCFM+CT14) doesn't include nuclear modification to the PDFs and shows a significant deviation from the measurement. (Figure published on [69].)

Finally, in figure 3.28, the normalized yield is divided further by the NLO pQCD CT14-based proton-proton cross section to compute the R_{AA} . The result is compared with the same theoretical calculations. Here, the measurement deviates from unity because of the nuclear suppression to the PDFs and because of the isospin content on the lead nucleus. For this observable, the uncertainties on the free-nucleon PDFs are factored out and the remaining uncertainty is on the

nuclear PDFs only. This is why the CT14 prediction is shown as a point without error.

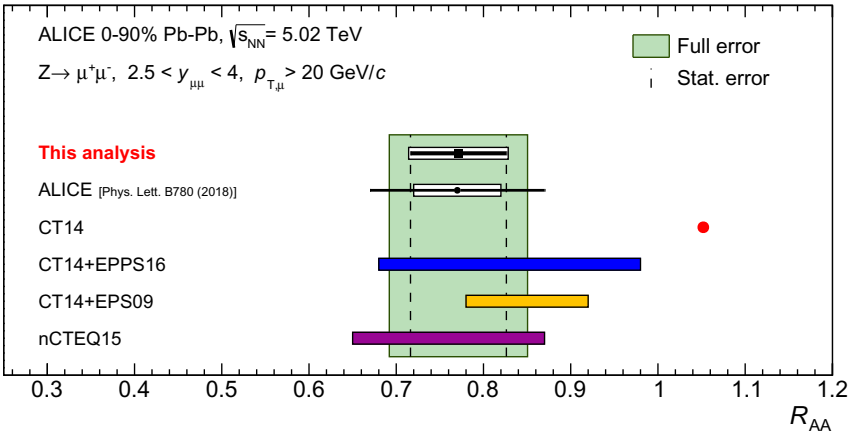

Figure 3.28. R_{AA} for $Z/\gamma^* \rightarrow \mu^+\mu^-$ in Pb-Pb collisions at $\sqrt{s_{NN}} = 5.02$ TeV . A NLO pQCD calculation with CT14 PDFs is used as proton-proton reference. The corresponding R_{AA} prediction (red point) is without uncertainty. Its deviation from unity is due to isospin. Style and colors are the same as in figure 3.27. ⋆THIS THESIS⋆

3.5.2 Results versus centrality and rapidity

The measured normalized yield in the three centrality classes 0-10%, 10-20% and 20-90% is shown in figure 3.29. The centrality is expressed as the average number of nucleons participating the collision. The uncertainty on $\langle N_{\text{part}} \rangle$ is not relevant. The boxes around datapoints distinguish between uncorrelated and total systematic uncertainties, the correlated part being equal to 6.1%. Here the results are compared to NLO calculation based on CT14 free-nucleon PDFs and to NLO calculation with CT14 plus EPS09s nuclear modification. Free-nucleon PDFs by definition don't carry a centrality dependence, while EPS09s do implement a dependence on the position inside the nucleus.[6] EPS09s actually shows a decrease in the invariant yield towards more central collisions, but the effect is very weak. For each bin its prediction is consistent with the more recent EPPS16 prediction, whose value is shown only in figure 3.27 not to overcrowd the plot. Data show a systematic suppression of the production with respect to the one

[6]Talking about centrality-dependence is actually inexact. The PDFs describe the properties of the nucleus independently on the fact that it collides. Nevertheless the *spatial-dependence of PDFs* is accessible only through the *centrality-dependence of the results*, and we are confident that the reader will forgive us.

predicted by free PDFs, while they are consistent with the quoted nuclear PDF sets in each centrality bin. No statistically significant trend versus centrality is measured. The Z boson production according to this result is consistent with a $\langle N_{\mathrm{coll}} \rangle$ scaling. The centrality dependence of R_{AA} would not add information to the already discussed 0-90% result.

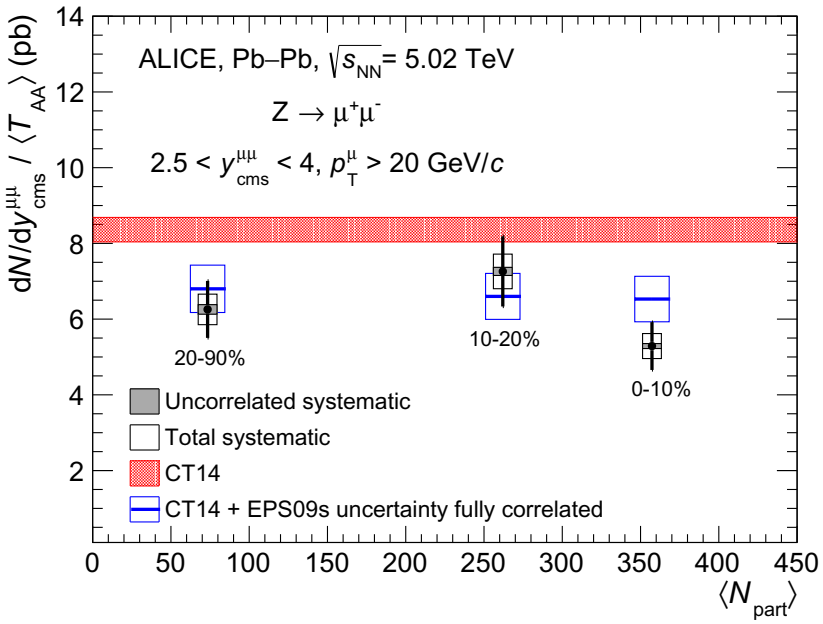

Figure 3.29. Yield of $Z/\gamma^* \rightarrow \mu^+\mu^-$ normalized by $\langle T_{\mathrm{AA}} \rangle$ measured in Pb-Pb collisions at $\sqrt{s_{\mathrm{NN}}} = 5.02$ TeV in different centrality classes. The open boxes correspond to the quadratic sum of correlated (6.1%) and uncorrelated systematic uncertainties. The results are compared with NLO pQCD calculations based on CT14 PDFs, with and without the addition of the centrality-dependent EPS09s nuclear modification. (Figure published on [69].)

The behavior of the fiducial production rate as a function of rapidity is shown in figure 3.30. Systematic uncertainties are not shown while the statistical error bars are made asymmetric to have a confidence level of 68% according to the poissonian distribution of the measured number of dimuons. The shape results from the convolution of the Z boson production cross section and geometrical acceptance of the fiducial cuts. The first is peaked at $y = 0$ and goes to zero at large rapidities. To explain the fast decrease of the observed yield at the boundaries of the ALICE acceptance, one has to consider that the opening angle between the Z decay muons prevent at least one of them to have rapidity above 2.5 or below 4 if the dimuon rapidity is 2.5 or 4 respectively. Therefore the cut on η_μ suppresses the fiducial production cross section at the boundaries.

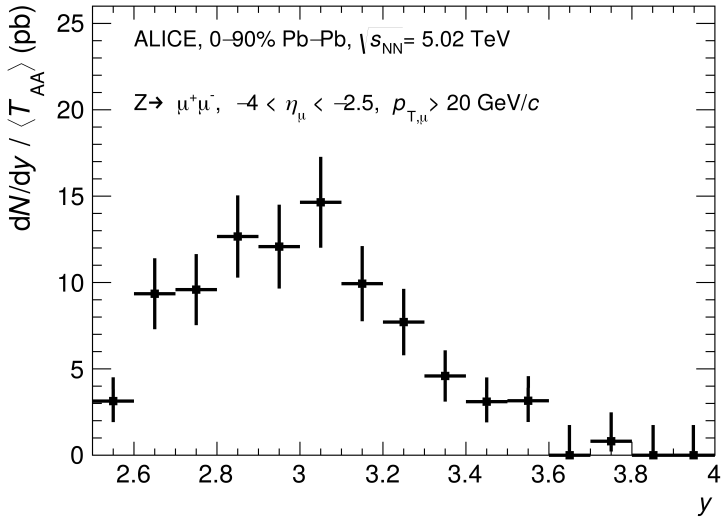

Figure 3.30. Behavior of the yield of $Z/\gamma^* \to \mu^+\mu^-$ (normalized by $\langle T_{\rm AA} \rangle$) measured in Pb-Pb collisions at $\sqrt{s_{\rm NN}} = 5.02$ TeV as a function of rapidity. Systematic uncertainties are not shown. ⋆THIS THESIS⋆

Figure 3.31 displays the differential normalized yield and the $R_{\rm AA}$ in the dimuon rapidity intervals $2.5 < y_{\mu\mu} < 2.75$, $2.75 < y_{\mu\mu} < 3$, $3 < y_{\mu\mu} < 3.25$ and $3.25 < y_{\mu\mu} < 4$. As usual, results are compared to free-nucleon PDFs predictions (CT14) and to calculations with nuclear PDFs (EPPS16). Nuclear shadowing is foreseen by EPPS16 in the whole rapidity range, with an increasing trend towards higher rapidity which is highlighted by the $R_{\rm AA}$ plot. Such behavior is consistent with the measured one; the deviation of data from CT14 predictions seems to be more evident in the last bin where the discrepancy amounts to 3.5 standard deviations. The higher $y_{\mu\mu}$ the higher the Bjorken-x of one of the high-x quark. Therefore the effect described can be interpreted as a transition of the high-x quark from the antishadowing to the EMC effect region, which enhances the suppression of the production rate. Figure 3.26, although qualitative, luckily represent this fact: the $3.25 < y_{\mu\mu} < 4$ interval makes the x values laying in the deepest part of the depletion region. However, the collected statistics is not enough to draw firm conclusions on this point.

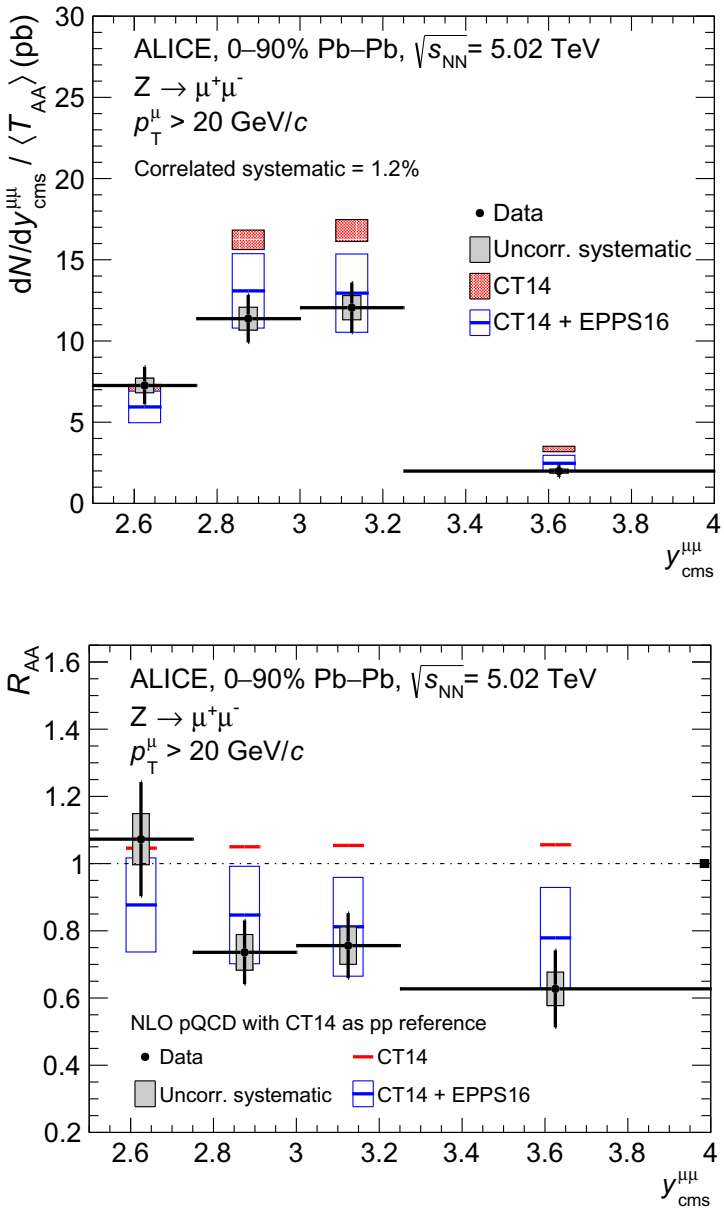

Figure 3.31. Yield of $Z/\gamma^* \rightarrow \mu^+\mu^-$ normalized by $\langle T_{AA} \rangle$ and corresponding R_{AA} measured in Pb-Pb collisions at $\sqrt{s_{NN}} = 5.02$ TeV in different rapidity intervals. The horizontal extensions of the bars correspond to the width of the rapidity bins. For the R_{AA} , a NLO pQCD calculation with CT14 free-nucleon PDFs is used as proton-proton reference. Results are compared to CT14 prediction, with and without EPPS16 nuclear modification. The R_{AA} correlated systematics is displayed as a box on the unity line. Deviation from unity of free PDF prediction is an isospin effect. (Figures published on [69].)

3.5.3 Remarks

1. On the extension to 0-100% centrality class

Most of the existing nPDF sets describe an average effect over all the nucleons, neglecting a possible dependence on the position inside the nucleus. The centrality dependence of the experimental yields or cross sections is at a first approximation canceled out by the normalization to $\langle N_{\rm coll}\rangle$ or $\langle T_{\rm AA}\rangle$. Nevertheless, results which are fully inclusive in centrality are more suited to be included in the nPDFs global fits. We prove now that **our normalized yield computed with events with centrality up to 90% can be regarded as fully inclusive in centrality**. In the following there is no need to propagate the uncertainties on the measurement and the other quantities, since at the end a very conservative estimation will be given. The Glauber MC results are taken from [11].

The measured yield not normalized by $\langle T_{\rm AA}\rangle$ and the one predicted by CT14 free-nucleon PDFs, in 0-90% centrality, in the $2.5 < y_{\mu\mu} < 4$ interval, are

$$\Upsilon^{\rm Data}_{\text{0-90}} = 57.7 \cdot 10^{-9} \qquad \text{and} \qquad \Upsilon^{\rm CT14}_{\text{0-90}} = 78.8 \cdot 10^{-9}$$

From them, the predicted yield in $90-100\%$ can be computed assuming the proportionality with $\langle N_{\rm coll}\rangle$:

$$\Upsilon^{\text{Data-scaled}}_{\text{90-100}} = \Upsilon^{\rm Data}_{\text{0-90}} \frac{\langle N_{\rm coll}\rangle_{\text{90-100}}}{\langle N_{\rm coll}\rangle_{\text{0-90}}} = 0.231 \cdot 10^{-9}$$
$$\Upsilon^{\text{CT14-scaled}}_{\text{90-100}} = \Upsilon^{\rm CT14}_{\text{0-90}} \frac{\langle N_{\rm coll}\rangle_{\text{90-100}}}{\langle N_{\rm coll}\rangle_{\text{0-90}}} = 0.315 \cdot 10^{-9}$$

The idea is to point out that even if we don't know how big is the nuclear modification for the 90-100% events, the normalized extrapolated yield is in any case compatible with the one measured in 0-90%. The extrapolated yield is

$$\Upsilon_{\text{0-100}} = \frac{9 \cdot \Upsilon_{\text{0-90}} + \Upsilon_{\text{90-100}}}{10}$$

The formula relies on the fact that the distribution of minimum bias events over centrality is uniform and the average over centrality coincides with an arithmetic mean. We can first compute $\Upsilon_{\text{0-100}}$ assuming a nuclear modification in the 90-100% class which is on average the one measured in 0-90%,

$$\Upsilon^{\text{Data+data}}_{\text{0-100}} = \frac{9 \cdot \Upsilon^{\rm Data}_{\text{0-90}} + \Upsilon^{\text{Data-scaled}}_{\text{90-100}}}{10}$$

and then assuming no nuclear modification in 90-100%, i.e. relying on free PDFs

calculation:

$$\Upsilon_{0\text{-}100}^{\text{CT14+data}} = \frac{9 \cdot \Upsilon_{0\text{-}90}^{\text{Data}} + \Upsilon_{90\text{-}100}^{\text{CT14-scaled}}}{10} \simeq \Upsilon_{0\text{-}100}^{\text{Data+data}} = 52.0 \cdot 10^{-9}$$

Going up to the fourth digit, we notice that these values differ by 0.02%, completely negligible if compared to the experimental uncertainty. In principle one should test also the extreme case of a huge modification in the 90-100% centrality class. In general, we can parameterize the $\langle N_{\text{coll}} \rangle$ scaling in peripheral events with a factor $f \geq 0$ as follows:

$$\Upsilon_{90\text{-}100}(f) = f \cdot \Upsilon_{0\text{-}90}^{\text{Data}} \frac{\langle N_{\text{coll}} \rangle_{90\text{-}100}}{\langle N_{\text{coll}} \rangle_{0\text{-}90}}$$

We can now express the relative discrepancy between the extrapolated normalized yield and the measured one in terms of f:

$$\begin{aligned} \frac{\Upsilon_{0\text{-}100}}{\langle T_{\text{AA}} \rangle_{0\text{-}100}} &= \frac{\left(9 \cdot \Upsilon_{0\text{-}90}^{\text{Data}} + \Upsilon_{90\text{-}100}(f)\right)/10}{\langle T_{\text{AA}} \rangle_{0\text{-}90} \langle N_{\text{coll}} \rangle_{0\text{-}100} / \langle N_{\text{coll}} \rangle_{0\text{-}90}} \\ &= \frac{\Upsilon_{0\text{-}90}^{\text{Data}}}{\langle T_{\text{AA}} \rangle_{0\text{-}90}} \frac{9 \cdot \langle N_{\text{coll}} \rangle_{0\text{-}90} + f \cdot \langle N_{\text{coll}} \rangle_{90\text{-}100}}{10 \cdot \langle N_{\text{coll}} \rangle_{0\text{-}100}} \end{aligned}$$

Numerically, it results,

$$\frac{\text{Normalized yield (0-100\%)}}{\text{Measured norm. yield (0-90\%)}} - 1 = (f-1) \cdot 4.4 \cdot 10^{-4}$$

$f = 1$ means a perfect $\langle N_{\text{coll}} \rangle$ scaling of the measured yield, while $f = 0$ is the extreme case where there is no Z boson production at all in the 90-100% centrality class. To neglect any nuclear modification in 90-100% according to CT14 prediction, one has to choose $f = 1.4$ which results in the already mentioned 0.02% of relative difference. Even in the case of a huge nuclear enhancement of the production in 90-100%, the numbers are fully under control.[7]

To summarize, the extrapolation of the yield divided by $\langle T_{\text{AA}} \rangle$ in the 0-100% centrality class depends on how the nuclear effects are modeled in the 90-100% interval. Nevertheless the systematics induced by this operation are fully included in the uncertainties of the experiment.

[7] There is no need to be more precise. For example, with $f = 14$ (ten times the yield predicted by CT14), the relative difference between scaled and measured normalized yields is below 0.5%.

2. On the significance of the measured nuclear modification

The results show a nuclear suppression of the Z boson production. To be quantitative on its significance, a simple hypothesis test can be done. We evaluate the p-value associated to the measured yield under the hypothesis of no nuclear modification to the PDFs [116]. The CT14 calculation will be used as null hypothesis and we will consider the integrated measurement. Apart from the systematic uncertainty, the measured yield follows a poissonian distribution scaled by a factor whose fluctuations can be neglected (the factor is the product of N_{MB}, eff , $\langle T_{\mathrm{AA}} \rangle$, Δy). The statistical fluctuations on the measured number of Z bosons under the null hypothesis follow a poissonian statistics centered on a value given by the CT14 yield. When computing the aforementioned p-value, the experimental uncertainty expressed as $N_{\mathrm{Z}}^{raw} \pm \sqrt{N_{\mathrm{Z}}^{raw}}$ doesn't play any role.

Knowing the central value of the CT14 normalized yield, the predicted raw signal in the conditions of the experiment described in this chapter is:

$$N_{\mathrm{Z}}{}^{\star} = \left.\frac{dN/dy}{\langle T_{\mathrm{AA}} \rangle}\right|_{\mathrm{CT14}} \times [\langle T_{\mathrm{AA}} \rangle \, eff \, N_{\mathrm{MB}} \, \Delta y] = N_{\mathrm{Z}}^{raw} \cdot \frac{\left.\frac{dN/dy}{\langle T_{\mathrm{AA}} \rangle}\right|_{\mathrm{CT14}}}{\left.\frac{dN/dy}{\langle T_{\mathrm{AA}} \rangle}\right|_{\mathrm{Measured}}} = 283.8 \tag{3.5.6}$$

This follows directly from formula (3.5.2) and the star (*) identifies the expected value under the null hypothesis. 208 Z bosons have been measured instead. Numbers are high enough to have gaussian confidence levels; without any systematic or theoretical uncertainty, the significance of the measured nuclear effect would be $(283.8 - 208)/\sqrt{283.8} = 4.5$. To account for those uncertainties, the poissonian distribution with mean 283.8 must be convoluted with a gaussian having a width equal to the experimental systematic uncertainty and with another distribution addressing the theoretical CT14 error. Both the cases corresponding to gaussian and uniform confidence levels for the CT14 uncertainty are shown in figure 3.32. The requested p-value is the area under the tail of the distribution below $N_{\mathrm{Z}} = 208$, which amounts to $1.5 \cdot 10^{-3}$ (gaussian core) or $0.9 \cdot 10^{-3}$ (uniform core). The corresponding Z-scores (quantiles of the standard gaussian distribution) are 2.96 and 3.12 respectively. We can conclude that the significance of the measured suppression with respect to free-nucleon PDFs predictions amounts to 3σ.

Sometimes the significance of an enhancement or suppression is quantified with the formula (3.5.5). If the statistical error is dominated by the poissonian particle production, this is wrong. In those cases, a simple but efficient correction to the quoted Z-score is obtained by scaling the standard deviation as explained

in this section:

$$\frac{\text{Data} - \text{Theory}}{\sigma(\text{Data})} \quad \rightarrow \quad \frac{\text{Data} - \text{Theory}}{\sigma(\text{Data})} \sqrt{\frac{\text{Data}}{\text{Theory}}}$$

This doesn't require to know the details of the experiment.

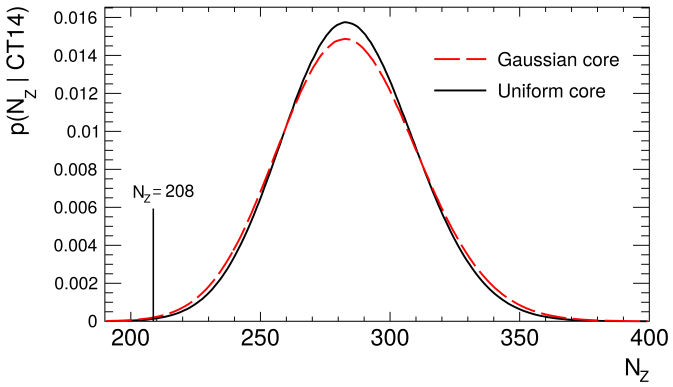

Figure 3.32. Simulated probability density function of the measured number of Z bosons in a replica of the experiment under study, under the hypothesis that the expected yield is the one foreseen by CT14 pQCD calculations. The theoretical uncertainty is associated to gaussian (red dashed line) or uniform (black solid line) confidence levels.

3.6 Comparison with other measurements

The ALICE Collaboration has published results or presented preliminary results on Z and $W^{\pm}$ production in all the collision systems involving lead ions tested during the LHC Run2. The results in p-Pb collisions at $\sqrt{s_{\rm NN}} = 8.16$ TeV are especially suitable for a comparison with the conclusions presented in the previous section. Because of the asymmetry of the collision, the geometrical acceptance of the spectrometer in the nucleon-nucleon center-of-mass frame is shifted with respect to the laboratory frame by the quantity

$$\Delta y = \pm \frac{1}{2} \ln \left(\frac{Z}{A} \right)$$

With $Z = 82$ and $A = 208$, it results $\Delta y = \pm 0.456$. The sign of the shift is given by the direction of the proton beam. At 8.16 TeV the shift in rapidity is partially compensated by the higher energy and the resulting Bjorken-x values of the involved partons are very close to those of Pb-Pb collisions at 5.02 TeV

(by means of formula (3.5.4), $e^{0.456} \times [5.02\,\text{TeV}/8.16\,\text{TeV}] \simeq 1$). A peculiarity of the p-Pb collisions is that depending on the direction of the beams, the muon spectrometer is in the forward or backward position with respect to the proton-lead system. As a consequence, the high-x and low-x regions of the partons inside the lead nucleus can be probed separately.

The cross section of $\mu^+\mu^-$ production from Z boson decay in p-Pb collisions at $\sqrt{s_{\text{NN}}} = 8.16$ TeV is shown in the left panel of figure 3.33 for the forward and backward rapidity [69]. By convention, positive rapidities are used when the proton beam goes from the interaction point towards the muon spectrometer. In this configuration a Z boson produced forward is the result of the interaction of a sea quark inside the nucleus with a high-x quark in the proton. On the other hand, negative rapidity measurements probe the high-x region in the nucleus (see figure 3.26 and equation 3.5.4). The figure shows that the measurement is consistent with pQCD calculations which include nuclear modification to the PDFs. To comment the observed deviation to free-nucleon PDFs predictions, two points are important. (1) In p-Pb collision the nuclear modification affects only one of the colliding nucleons. Consequently the discrimination power between PDFs and nPDFs calculations in each rapidity interval is reduced with respect to the one found in Pb-Pb collisions. (2) At backward rapidities, where the agreement between free and nuclear PDFs is higher, the probed x range is in a region where multiple nuclear effects are present (likely, antishadowing and EMC effects) . The resulting effect is less pronounced than the one at positive y which is in a pure shadowing regime.

What is observed in Pb-Pb collisions at $\sqrt{s_{\text{NN}}} = 5.02$ TeV is roughly the convolution of the effects at forward and backward y. We want to fix some numbers. Since a good estimation of their theoretical errors is not available, only weak conclusions will be drawn. The ratios between the yields predicted by free PDFs (CT14) and nPDFs (nCTEQ), in the Pb-Pb, p-Pb and Pb-p configurations are as follows.

$$\frac{N_Z(\text{PDFs})}{N_Z(\text{nDPFs})} = \begin{cases} 1.38 \pm 0.18 & (\text{Pb-Pb at 5 TeV}) \\ 1.27 \pm 0.20 & (\text{p-Pb at 8 TeV}, y > 0) \\ 1.03 \pm 0.07 & (\text{Pb-p at 8 TeV}, y < 0) \end{cases}$$

nCTEQ set is chosen to reduce the correlation between free and nuclear PDFs calculation. Although the forward p-Pb ratio is already close to the Pb-Pb one, a better agreement with the Pb-Pb ratio is reached when forward and backward p-Pb are multiplied. This corroborates the hypothesis that the combined analyses of positive and negative y in p-Pb collisions offer a sensitivity to nuclear modification similar to the one found in the analysis presented in this chapter.

Together with the Z boson , figure 3.33 shows the measured (fiducial) production cross section of W^+, again studied in p-Pb collisions at $\sqrt{s_{NN}} = 8.16$ TeV and in the rapidity acceptance of the ALICE spectrometer. The W boson is measured in its muonic decay channel. The neutrino missing energy cannot be measured and the signal is extracted by fitting the single muon p_T distribution, once the heavy-flavour and Z boson decay contributions are subtracted with Monte Carlo templates as described in [67]. Here the same forward rapidity region discussed so far is further split in three intervals. The measured discrepancy with non-nuclear-modified CT14 PDFs increases toward higher rapidities, i.e. lower values of Bjorken-x, probably showing an increase in the shadowing effect strength. Other results on $W^{\pm}$ in forward/backward regions are accessible at [117].

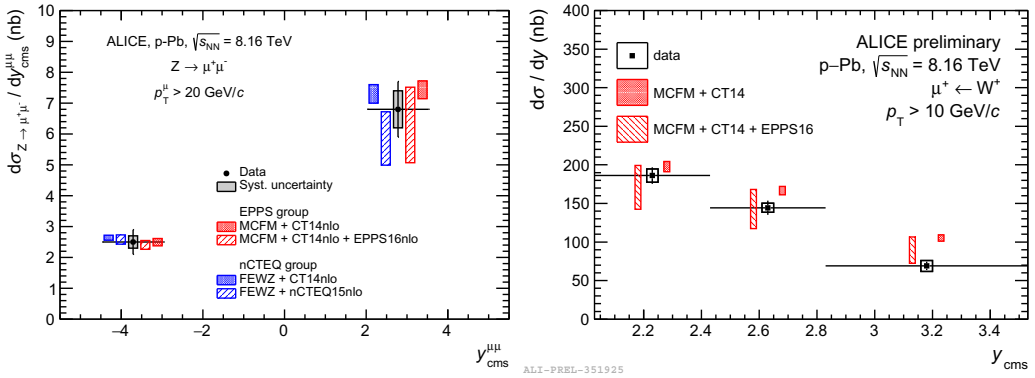

Figure 3.33. **Left:** Production cross section of $Z/\gamma^* \to \mu^+\mu^-$ measured in p-Pb collisions at $\sqrt{s_{NN}} = 8.16$ TeV . Positive and negative rapidities are referred to the direction of the proton beam. Data are compared to pQCD calculations with free-nucleon PDFs (CT14) or with nuclear PDFs (CT14+EPPS16 and nCTEQ15). The theory points are shifted for better readability. [69]. **Right:** Cross section of the production of μ^+ from the $W^+ \to \mu^+\nu$ decay in p-Pb collisions at $\sqrt{s_{NN}} = 8.16$ TeV . The measurement is compared to theory including or not including nuclear modification to the PDFs [117].

With regard to the comparison with other experiments, figure 3.34 shows the magnitude of the nuclear effect on Z boson production in Pb-Pb collisions measured by ATLAS [74] and ALICE (this work), therefore covering the full rapidity interval $0 < y < 4$. The analyses are performed in different fiducial regions. ATLAS extracts the Z boson signal from muons and electrons having $p_T > 20\,\mathrm{GeV}/c$, $|\eta| < 2.5$ and invariant mass between 66 and 116 GeV/c^2. Moreover, ATLAS uses data taken in the full 0-100% centrality range, even though we showed that also ALICE final calculations can be regarded as fully inclusive in centrality. A fair comparison of the fiducial yields is not possible because of these differences, but when computing a data-over-theory ratio the effect of the

(slightly) different cuts are greatly suppressed. In the figure the yields normalized by $\langle T_{\rm AA} \rangle$ are divided in each rapidity bin by the corresponding pQCD calculation based on CT14 PDFs. The deviation from unity of the datapoints quantifies the measured nuclear suppression or enhancement. A residual small bias is actually given by the different $\langle T_{\rm AA} \rangle$ values used by ATLAS and ALICE, being the ATLAS Glauber-MC calculation lower than ALICE by 1.5%.

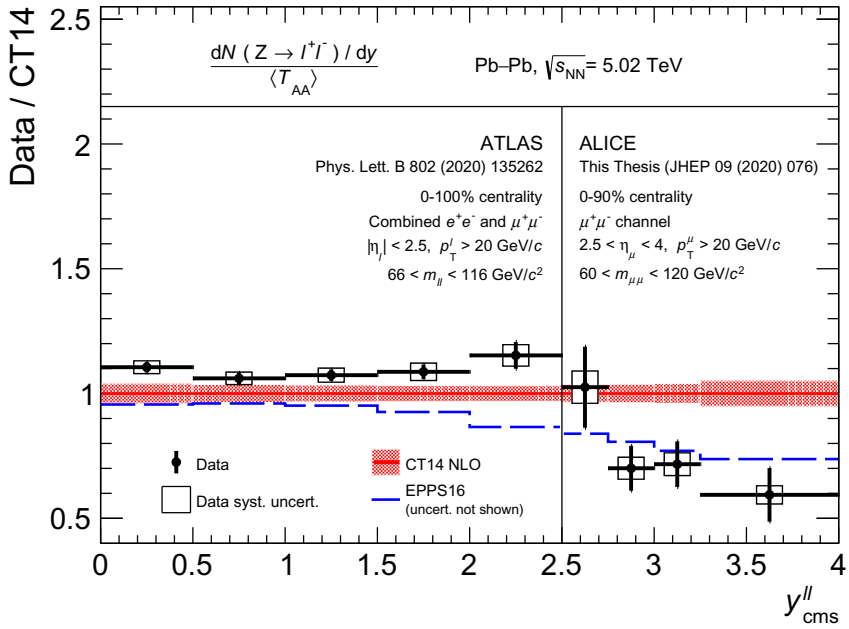

Figure 3.34. Comparison between Z boson normalized yields measured by ATLAS at midrapdity [74] and ALICE at large rapidity in Pb-Pb collisions at $\sqrt{s_{\rm NN}} = 5.02$ TeV . pQCD calculations based on CT14 free PDFs are taken as reference for the data/theory ratio. Details on the different fiducial cuts of the two analyses are given inside the figure and in the text. The boxes around unity represent the theoretical uncertainty on CT14 calculations. The uncertainty on the EPPS16/CT14 ratio is not shown. ⋆THIS THESIS⋆

We already noticed that the Drell-Yan production at midrapidity involves quarks which are expected to experience both nuclear shadowing and antishadowing, bringing to a reduced net effect (see sec. 1.5 and the figure at page 90). The nuclear suppression is expected to be enhanced at large rapidity, in the ALICE kinematic region. This is actually confirmed by the experiments. On the other hand figure 3.34 shows some tension between the measured trend versus y and the one predicted by EPPS16 nPDFs, displayed as dashed line. This is especially true in the interval $1 \lesssim y \lesssim 2.8$. Moreover, ATLAS data are sistematically

higher than free-nucleon PDFs calculations.[8] For sake of completeness, two facts should be noticed. (1) CT14 calculations underestimate ATLAS Z boson measurements also in pp collisions at $\sqrt{s} = 5.02\,\text{TeV}$ [118]. Indeed the experimental ATLAS R_{AA} is consistent with free-PDFs as one can see in [74]. (2) Such enhancement with respect to CT14 calculations in Pb-Pb collisions at $\sqrt{s_{\text{NN}}} = 5.02$ TeV is not confirmed by CMS results (reference [65]).

[8] In section 1.5 we already talked about the unexpected enhancement of Z and W production measured by ATLAS in peripheral collisions.

3.7 Summary and conclusions

This chapter presented the measurement of the production rate of Z bosons in lead-lead collisions at the nucleon-nucleon center-of-mass energy of $\sqrt{s_{\rm NN}} = 5.02$ TeV . The full statistics collected by ALICE in this collision system has been analyzed. The signal has been extracted by measuring opposite-sign muon pairs reconstructed in the ALICE muon spectrometer at large rapidity ($2.5 < y_{\mu\mu} < 4$). The main motivation behind this work is the ability of this measurement to provide new constraints on the study of the nuclear parton distribution functions (nPDFs). The reason why Z (and W) bosons are particularly suited to this purpose has been widely discussed in previous chapters. The acceptance of the ALICE muon arm makes it possible to provide results in a kinematic region where the nPDFs are less known, complementary to those investigated by ATLAS and CMS.

The production yield normalized by the nuclear overlap function $\langle T_{\rm AA} \rangle$ and the nuclear modification factor $R_{\rm AA}$ have been presented as a function of rapidity and centrality of the collision. The production rate was found to scale with the number of nucleon-nucleon binary collisions within uncertainties. The results have been systematically compared with pQCD calculations based on some of the most recent free-nucleon and nuclear PDFs. The comparison highlighted the presence of a significant nuclear shadowing: free-nucleon PDFs predictions overestimate the measurement by 3σ. This is one of the strongest evidence of nuclear modification measured with electroweak bosons in the literature. The differential studies showed a higher suppression at larger rapidity, where the very high Bjorken-x value of one of the involved partons is probed. This is compatible with the typical behavior of the nPDFs which at large x foresee a stronger nuclear suppression known as EMC effect. In each bin the experimental data are in agreement with calculations including nuclear-modified PDFs.

The differential results presented in this thesis, together with the new results by ALICE in other proton-nucleus collision systems, represent a considerable amount of new data points providing extra inputs for the nPDFs global fits.

Appendix to chapter 3

3.A Numeric tables

The following tables give the numeric results for the normalized yield $\frac{dN/dy}{\langle T_{AA} \rangle}$ and the R_{AA} of $Z \rightarrow \mu\mu$ production measured in Pb-Pb collisions at $\sqrt{s_{NN}} = 5.02$ TeV . The measurements are displayed in the figures of sections 3.5.1 and 3.5.2. The values provided by pQCD calculations are also shown. Some of the free-nucleon and nuclear PDFs discussed in the previous chapters have been chosen: CT14 [42], EPS09s for the centrality dependence [59] and EPPS16 [49].

	Data	CT14	CT14+EPPS16
full	$0.770 \pm 0.055 \pm 0.057$	1.052	0.826 ± 0.146
Centrality			
0-10%	$0.666 \pm 0.079 \pm 0.008 [\pm 0.048]$	↑	↑
10-20%	$0.914 \pm 0.117 \pm 0.013 [\pm 0.066]$		
20-90%	$0.787 \pm 0.095 \pm 0.016 [\pm 0.057]$		
Rapidity			
$y \in [2.50, 2.75]$	$1.073 \pm 0.170 \pm 0.076 [\pm 0.012]$	1.046	0.877 ± 0.140
$y \in [2.75, 3.00]$	$0.736 \pm 0.085 \pm 0.053 [\pm 0.009]$	1.050	0.847 ± 0.145
$y \in [3.00, 3.25]$	$0.756 \pm 0.097 \pm 0.056 [\pm 0.009]$	1.054	0.812 ± 0.147
$y \in [3.25, 4.00]$	$0.627 \pm 0.115 \pm 0.050 [\pm 0.007]$	1.056	0.779 ± 0.150

Table 3.A.1. $Z \rightarrow \mu\mu$ R_{AA} results and comparison with theory. The centrality-dependent values are integrated over rapidity and viceversa. The errors on data are split in statistical (first number), uncorrelated systematic (second number) and correlated systematic (between brackets). The latter amounts to 7.3% versus centrality and 1.2% versus rapidity. Arrows are used where the values are not centrality-dependent.

	Data	CT14	CT14 +EPS09s	CT14 +EPPS16
full	6.13 $\pm 0.44 \pm 0.38$	8.363 ± 0.324	6.63 ± 0.61	6.654 ± 1.188
Centrality				
0-10%	5.29 $\pm 0.63 \pm 0.056$ [± 0.32]		6.53[± 0.60]	
10-20%	7.26 $\pm 0.93 \pm 0.107$ [± 0.44]	↑	6.60[± 0.61]	↑
20-90%	6.26 $\pm 0.75 \pm 0.126$ [± 0.38]		6.80[± 0.63]	
Rapidity				
$y \in [2.50, 2.75]$	7.26 $\pm 1.15 \pm 0.45$ [± 0.08]	7.08 ± 0.25		5.94 ± 0.97
$y \in [2.75, 3.00]$	11.37 $\pm 1.46 \pm 0.70$ [± 0.13]	16.23 ± 0.60		13.09 ± 2.29
$y \in [3.00, 3.25]$	12.05 $\pm 1.54 \pm 0.75$ [± 0.14]	16.81 ± 0.67		12.95 ± 2.41
$y \in [3.25, 4.00]$	1.99 $\pm 0.36 \pm 0.12$ [± 0.02]	3.35 ± 0.17		2.47 ± 0.49

(pb)

Table 3.A.2. Values for the $Z \to \mu\mu$ normalized yield. All numbers are in picobarn. The centrality-dependent values are integrated over rapidity and vice versa. The errors on data are split in statistical (first number), uncorrelated systematic (second number) and correlated systematic (between brackets). The latter amounts to 6.1% versus centrality and 1.2% versus rapidity. Arrows are used where the values are not centrality-dependent.

Appendix A

Preparing ALICE for Run3: studies on the new ITS

The CERN accelerator complex and its experiments are being maintained and upgraded. The ongoing Long Shutdown (the second one, LS2) started at the end of 2018 with the main goal of implementing the High Luminosity LHC (HL-LHC) project that will increase the luminosity by a factor 10. HL-LHC is expected to be operational after the next LS3, in 2027. The study of the QCD matter at LHC after LS2 will focus on rare probes and their coupling with medium and hadronization processes. This includes: a precise measurement of heavy flavour in-medium energy loss; the study of a possible thermalization of heavy quarks in the medium; characterization of quarkonia dissociation and regeneration as a thermometer for the medium; more detailed jet studies, like the flavour dependence of the parton energy loss; study of low-mass dileptons and thermal photons which are sensitive to the initial temperature and the equation of state of the medium [119]. The greater integrated luminosity, foreseen to be 100 times larger than the Run2 one, will increase the statistical precision [120]. The ALICE detector and software are being upgraded to cope with the new program. Vertex reconstruction and tracking capabilities will be improved to allow high precision measurement of rare probes at very low transverse momentum at the increased luminosity. The new Pb-Pb collisions luminosity will amount to $6 \times 10^{27}\,\mathrm{cm}^{-2}\mathrm{s}^{-1}$, resulting in an interaction rate of 50 kHz, which cannot be sustained by the current 500 Hz readout capability. An example of the expected performance from Run3 and Run4 on the measurement of Z bosons is reported in figure A1.

The readout software will have to cope with the total throughput from the detector which will increase up to 3 TB/s. The whole data processing chain has been rethought, with a tighter integration between the online and offline processing software. More details on the structure of the resulting code, named O^2

(Online-Offline), can be found in [121, 122].

On the detector side, both the hardware and the readout electronics are being improved. The TPC multiwire chambers will be replaced by Gas Electron Multiplier (GEM) detectors and the electronics will be replaced allowing for a continuous readout [123]. The readout electronics of TRD, TOF, PHOS will also be upgraded . The Muon Spectrometer will manage to achieve a readout rate of 100 kHz thanks to an architecture where the signals are continuously sampled in a self-triggered readout mode [124].

A cornerstone of the ALICE upgrade is the introduction of a new high-resolution, high-granularity and high-transparency silicon pixel technology for tracking purpose. Such pixels will be used to install two new detectors. The first is the **Muon Forward Tracker (MFT)** which will be placed in front of the muon absorber, at pseudorapidity $-3.6 < \eta < -2.45$. The extrapolated tracks coming from the muon tracking chambers will be matched with the MFT tracks, resulting in a high pointing accuracy. New and improved measurements will be possible, especially in the study of quarkonium production, open heavy flavour and low-mass dimuons [125]. The second is a newly constructed **Inner Tracking System (ITS)**. The pixels will be arranged in seven cylindrical layers which will replace entirely the existing ones. Presently[1] the new detector is completed, mounted on surface at the CERN laboratories, and under commissioning.

After a short introduction on the pixels technology, a description of a campaign of ageing tests on the new ITS modules will be given. I carried out this work in collaboration with the INFN sections of Bari and Pavia [126].

A.1 The ALICE pixel detector

Silicon detectors are widely employed in different applications, and in experimental physics for particle and radiation detection and tracking. To better highlight the technology used for the new ALICE ITS, a first distinction between "traditional" hybrid pixel sensors and the monolithic ones is described. A typical hybrid pixel is on the left panel of figure A2. It consists of two separate silicon chips, one hosting the active volume and the other being the CMOS readout chip. When a particle crosses the sensor chip the energy released converts into electron-hole pairs and the charge is collected by drift in an electric field or by diffusion. The readout chip includes the readout electronics which processes the signal. Such technology takes advantage from the possibility of a separate optimization of the sensor and readout chips. A high reverse bias voltage can be applied to the sensor which can be fully depleted, allowing a more efficient and

[1] November 2020.

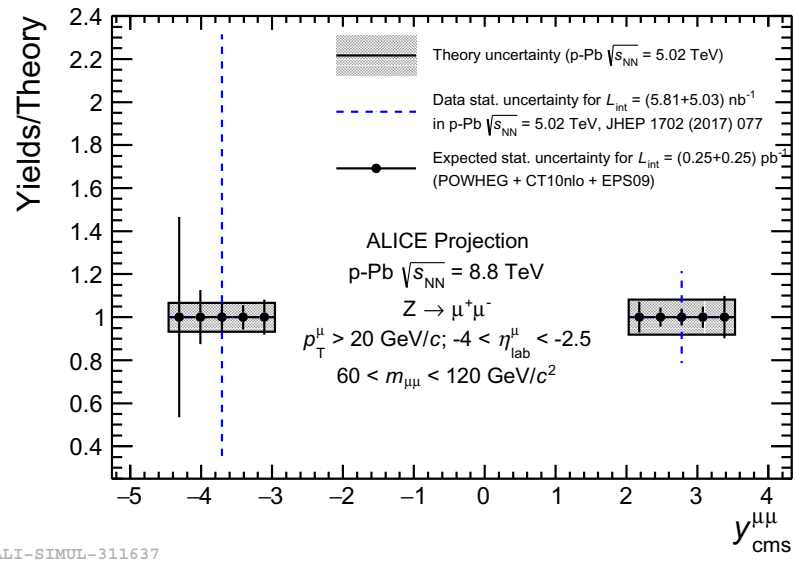

Figure A1. Expected statistical precision for Z boson yield versus rapidity, in p-Pb collisions at $\sqrt{s_{\rm NN}} = 8$ TeV . It can be compared to the cross section measured during Run2 and reported in figure 3.33. In the plot the comparison is done with the results published in [67]. The theoretical reference is simulated with POWHEG using EPS09 nPDFs with CT10 NLO baseline. Figure from [127].

faster charge collection, as well as an higher radiation tolerance. But hybrid sensors are thicker (more material budget means less transparency), more delicate and may suffer from intrinsic degradation of the detection efficiency because of the presence of the bump bonding between the chips.

On the other hand, a scheme of the Monolithic Active Pixel Sensors (MAPS) is presented in the right part of the figure. Here the active volume and the front-end electronics are integrated in the same volume, resulting in a huge gain in terms of material budget (ALICE ITS pixels are 50 μm or 100 μm thick, depending on the layer) and in a better charge collection thanks to the absence of the bump bonding. The MAPS sensors are based on the 180 nm CMOS technology of TowerJazz, which uses up to 6 metal layers to implement high density CMOS digital circuitry with low power consumption [129]. Other important features are the availability of high-resistive ($> 1\,\mathrm{k}\Omega\,\mathrm{cm}$) epitaxial layers that allows a better charge collection, and the possibility of reversing bias the substrate which significantly improves the charge collection [130]. The signal sensing elements are n-well diodes about 2 μm wide. The electrons reaching the depletion volume of the diode induce a current signal at the input of the pixel front-end. The TowerJazz manufacturing also provides a deep p-well layer to shield the epitaxial layer from the n-wells of the PMOS transistors (see figure A2) which otherwise would

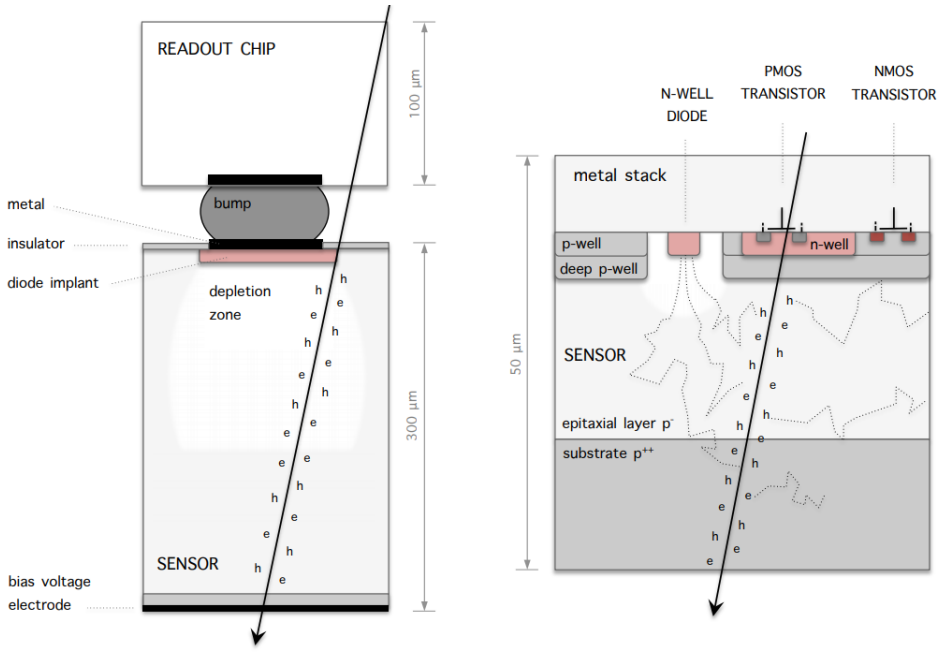

Figure A2. Cross sections of a hybrid pixel sensor (on the left) and of a monolithic pixel sensor (on the right). The deep p-well is a feature of the TowerJazz 180 nm CMOS process. Picture from [128].

compete with the sensing diodes in collecting the charge [131].

After several years of research and development, and after different prototypes, the pixels are now arranged in matrices which form a chip named ALPIDE (ALICE PIxel DEtector). Each chip measures 30 mm $\times$ 15 mm (z and $r\phi$ directions respectively in the detector layout) and contains a pixel matrix with 1024 columns and 512 rows (more than half a million pixels) allowing a spatial resolution of 5 μm over a large operational range. The analog power consumption of the chip is around 25 mW, while the digital and readout lines consumption is proportional to the readout rate and to the occupancy. During operation an overall consumption less than 40 mW/cm^2 will be reached. The very low fake-hit rate, less than 10^{-10} pixel/event, and the high detection efficiency, larger than 99%, are other remarkable features. Moreover, the compact manufacturing process allows to keep the thickness of the detector very small, down to 0.3% X_0 in the innermost layers where the chips are 50 μm thick and to $\simeq$ 1% X_0 in the outer layer where the chips are 100 μm thick.

The chips mounted on the detector cover a total active area of $\simeq$ 10 m^2 and are arranged in seven concentric cylindrical layers as shown on the left of figure A3. The first three innermost layers are part of the Inner Barrel (IB) and are located

between 2.2 and 4 cm in the radial direction. To allow the tracker being closer to the interaction vertex, the beam pipe radius will be reduced from 30 to 19.2 mm. The other four layers compose the Outer Barrel (OB) (two "middle layers" and two "outer layers"). The outermost layer has a radius of 40 cm. The length in the z direction ranges from 27 to 148 cm. Each layer is azimuthally segmented in several staves. The outer staves are split in two independent half-staves arranged in order to ensure a full (partially redundant) azimuth coverage. The smallest operable unit of each stave is called HIC (Hybrid Integrated Circuit) and consists of an array of ALPIDE chips. Nine chips in a row form the Inner Barrel HICs (IB HICs, here each stave is made by a single HIC) while 2 rows with 7 chips each form the OB HICs (4 or 7 HICs for middle and outer layers respectively). An exploded view of an OB HIC is visible in figure A3.

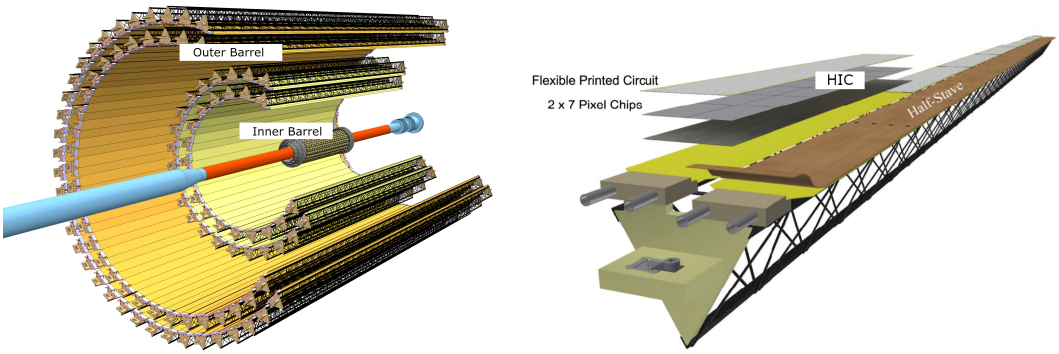

Figure A3. Layout of the new ITS. **Left:** Geometry of the seven concentric layers arranged in the Inner (layers 0, 1, 2) and Outer (layers 3, 4, 5, 6) Barrel. **Right:** Outer Barrel stave with exploded view of one of the HICs. Pictures taken from [132].

A.2 Assembling and testing the hybrid modules

The IB HICs were produced at CERN while OB HICs were assembled in Bari (IT), Liverpool (UK), Pusan/Inha (IN), Strasbourg (FR) and Wuhan (CN). A common procedure and a partially automated assembly system were used to ensure a homogeneous quality among the different sites involved in the assembly and during the whole production. 95 IB staves and more than 2500 OB HICs were produced, with a yield greater than 80% [133].

As a first step the chips are aligned with a precision of maximum 5 μm. Then, by means of an adhesive mask, a precise pattern of glue droplets (epoxy resin) is dispensed on a polymide Flexible Printed Circuit (FPC) which is aligned and glued to the chips. The assembly of the FPCs and their quality inspection were

performed in Trieste and Catania (IT). An array of connection pads is present on the top surface of each chip. The original idea was to connect them to the FPC for power supply and I/O by means of a laser soldering technique [132, 134] but then it was decided to use an ultrasonic wedge bonding with a 25 μm aluminum wire. Three redundant connections are soldered on each pad, as it is visible in the bottom-right panel of figure A6. Aluminum and copper are used as FPC conductors for IB and OB modules, respectively. Figure A4 reports a picture of the sensor side of an OB HIC, where the 14 chips are distinguishable.

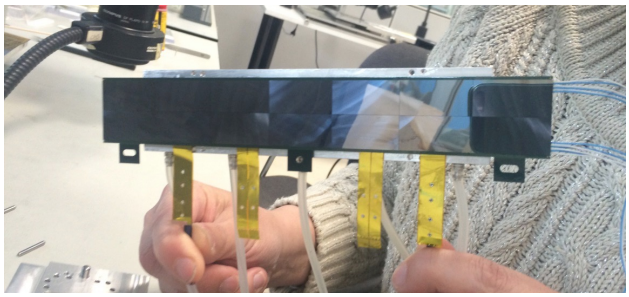

Figure A4. Sensor side of an Outer Barrel HIC. Four cross cables at the bottoms serve for electrical connection.

A.2.1 Ageing tests

The modules destined to be operational on the detector must pass a qualification procedure at the assembly site, made through custom electronics and interfaces. First, a fast "Impedance Test" is used to highlight the presence of shorts in the supply lines. Then the HIC is qualified through the "Qualification Test". Each pixel cell contains a sensing diode, a front-end amplifier and shaping stage, a discriminator and a digital section. This is shown in figure A5. In every pixel there is a pulse injection capacitor for the injection of test charge in the input of the front-end. The qualification test uses the digital and analogue lines to perform a series of scans over the pixels. The test identifies the number of working chips and classifies them in four categories (from `GOLD` to `NOT-WORKING`). The classification of the HIC is determined by the worst scan result. Different scans and different cuts on the result of each scan are used for the classification. The "Threshold Scan" uses the aforementioned internal testing functionality of ALPIDE. A charge is induced in the front-end circuit of the chips. The induced charge is changed and for each charge a number of injections is performed. Pixel by pixel, the number of recorded hits for each charge is measured. The resulting response function is a convolution of a pure step function (giving the threshold value) and a gaussian distribution representing the noise. Dedicated DAQ registers allow to tune the

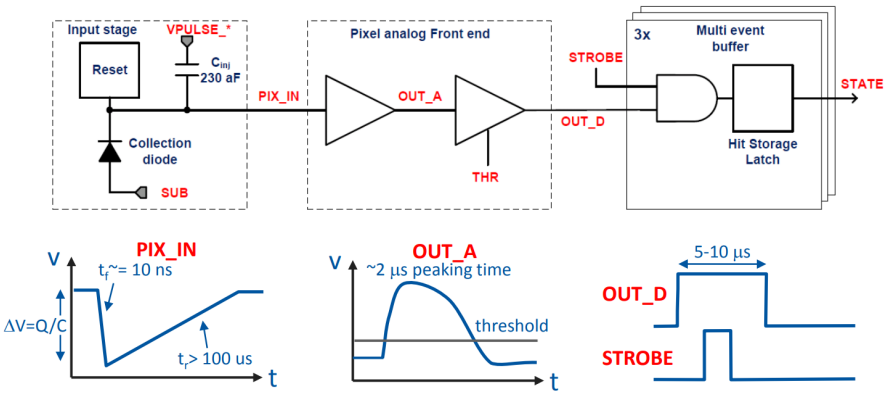

Figure A5. Block diagram of the ALPIDE pixel cell [131].

threshold chip by chip. The nominal value is chosen to be 100 electrons per pixel, averaged over the full chip. The typical pixel noise is about 5 electrons. Another test performed during the Qualification is the "Digital Scan". Here the internal testing functionality is used to inject pulses into the digital logic of the pixel cells. The test is performed in the range $\pm 10\%$ of the nominal supply voltage, which is 1.8 V. Problems in data transmission and the number of pixels not responding are registered.

Some HICs underwent more invasive tests designed to measure their mechanical strength. For example, during the "Peel Test" the FPC is ripped from the chips and the average breaking force is measured. The machine shown in the right panel of figure A6 is dedicated to the "Pull Test". The wired bonds are pulled out for a well defined number of the connecting pads on the HIC. The machine measures the distribution of the breaking force and looks for the presence of soldering damages.

Other tests of ageing were performed on a sub-sample of HICs with the purpose of ensuring their quality after several years of operation. We'll now describe those carried out at the INFN laboratories of Bari and Pavia [126]; other results are presented in [135].

The Arrhenius relationship [136] can be used to describe the effects of the temperature (and other factors such as the relative humidity) in the rate of the oxidation reactions on the chip-FPC bonding:

$$\mathcal{R} = \gamma_0 \, \exp\left[\frac{-E_a}{k_B \, T}\right]$$

where $\mathcal{R}$ is the reaction rate and E_a is the activation energy of the reaction. γ_0 is

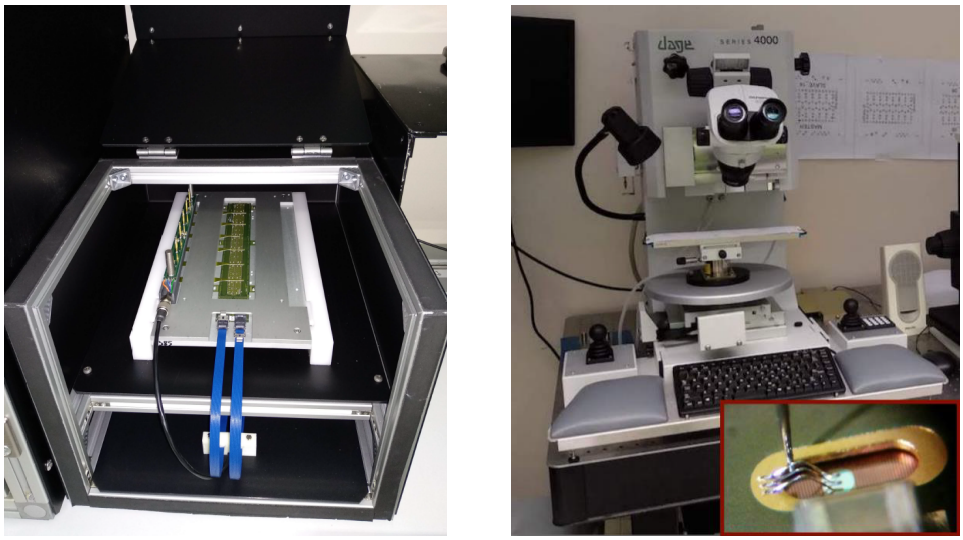

Figure A6. **Left:** Outer Barrel HIC in the station used for the Qualification Test. **Right:** The Pull Test station. [126]

a characteristic of the material. According to this equation, the acceleration factor $\mathcal{AF}$ induced by a temperature T_{stress} (with respect a normal operation at temperature T) is

$$\mathcal{AF} = \exp\left[\frac{E_a}{k_B}\left(\frac{1}{T} - \frac{1}{T_{stress}}\right)\right].$$

A sample of HICs were kept in a temperature and humidity controlled environment in order to simulate their ageing in the ALICE cavern. This allowed to check the endurance of the wire bonding as well as the stability of the electrical connections and the pixel response. According to reasonable estimates, with E_a in the range $0.7 - 0.8\,\text{eV}$ [126], a stress temperature of 60 °C causes an acceleration factor greater than 15, being the operating temperature equal to 25 °C. During the tests the HICs were kept in a climate chamber at 60 °C and 15% relative humidity: in these conditions a period of 4 weeks is sufficient to simulate one year of real operation. The HICs underwent up to five equivalent years of ageing. After each period the HICs were tested, both mechanically by means of the Pull Test and electrically by means of the Qualification Test.

After each ageing cycle, 56 wire bonds per HIC were pulled out and the distributions of the breaking forces were compared to those obtained before the cycle. A sample of the mean and minimum values of the forces is shown in figure A7. The bonding damages can be quantified by the number of peel off and lift off events occurred during the Pull Test, meaning the number of detachments of the solder with or without removal of the metallization. A view of such damages is

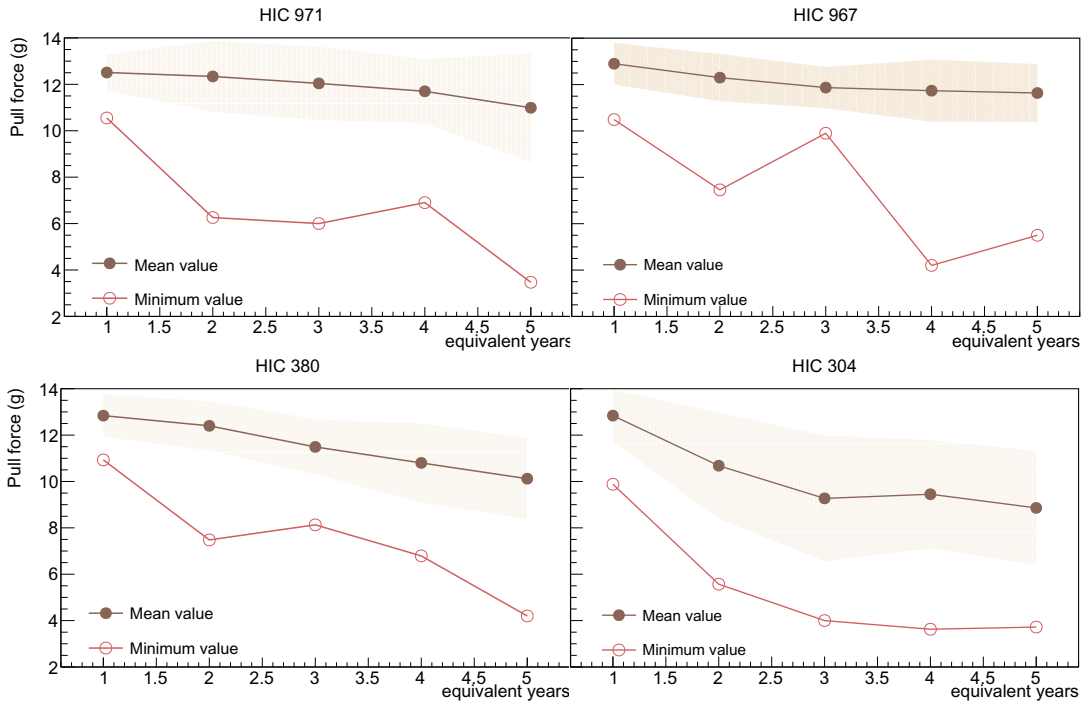

Figure A7. Distribution of the pull forces on four tested HICs as a function of time. The shadowed area is the standard deviation of the 56 measured values.

shown on the left of figure A8. The plot on the top reports the number of damages on the chip side after each ageing cycle. It is clear that the pad soldering didn't show sizable damages due to thermal effects. On the other hand, the deterioration of the soldering on the copper FPC was more evident. A correlation between the number of registered lift off and the minimum value of the breaking force during the pull test was also found (the larger is the number of damages on the FPC, the lower the breaking force). But those pads which registered a low force (< 5 grams is considered warning) were bound to other wires with higher breaking force, showing that the ageing seems to affect the pull test results on the single connection more than on the entire pad. Such lack of correlation between the low measured forces and the pad involved in the test confirms that the redundant connections keep the system reliable.

On the other hand, the results of the Qualification Tests were also used to monitor the HIC performances over time. The comparison of the outcome before and after each cycle was done on both the entire HIC and the single chips. If the HIC was working after the cycle in the climate chamber, the functionality of each chips was tested. The number of bad pixels in Digital or Threshold Scan and the pixel noise are parameters of interest. The results didn't show any systematic

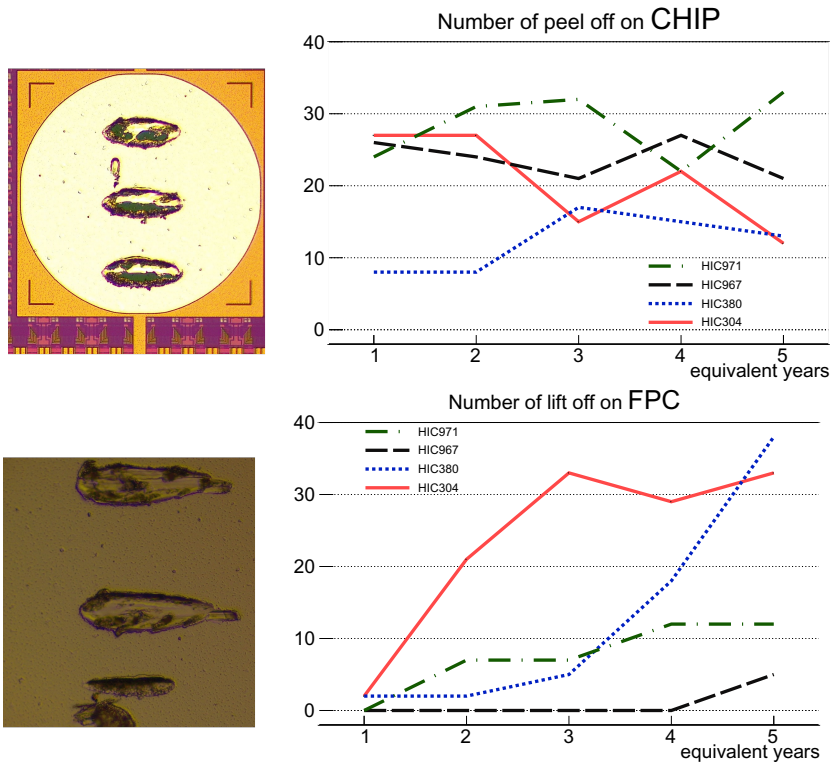

Figure A8. Peel off and lift off of the soldering on chip pad and FPC pad respectively. The plots report the evolution of the number of damages measured after each ageing period. Each line corresponds to a HIC.

effect due to the ageing: the number of working pixels as well as the noisy pixels and threshold distributions showed a good stability over time. As an example, let's consider the same 4 HICs shown in the previous figures. Over 56 chips, after two consecutive ageing cycles, 12 showed slightly worsened performance (with 323 more dead pixels per chip[2]), while 5 chips even resulted with a lower number of dead pixels. On average 42 ± 227 more bad pixels per chip were found saying that the intrinsic fluctuations of the test procedure masked any possible systematic effect due to the ageing.

A.2.2 Summary and conclusions

The modules of the new ALICE ITS were tested at the assembly sites using specially designed machinery and procedures. The qualification procedure was also used to evaluate the ageing of some modules subjected to thermal stress. As a conclusion, the electrical tests demonstrated no difference in the performances of

[2] 323 out of half a million!

the pixels over time. On the other hand, a worsening of the soldering strength is expected and a decrease in the value of the wire-bonding breaking forces has been actually measured. However, the average value (> 10 grams) and the minimum value (> 5 grams) after 5 equivalent-years of ageing, combined with the three-bond connections per pad, confirm the robustness of the system against ageing effects for the whole foreseen data taking period.

Bibliography

[1] V. Toivanen and D. Küchler, "Studies of the beam extraction system of the GTS-LHC electron cyclotron resonance ion source at CERN," *Review of Scientific Instruments* **87** no. 2, (Feb., 2016) 02B923. https://doi.org/10.1063/1.4934211.

[2] O. S. Bruning, P. Collier, P. Lebrun, S. Myers, R. Ostojic, J. Poole, and P. Proudlock, *LHC Design Report*. CERN Yellow Reports: Monographs. CERN, Geneva, 2004. https://cds.cern.ch/record/782076.

[3] C. Lefèvre, *The CERN accelerator complex. Complexe des accélérateurs du CERN*. Dec, 2008. https://cds.cern.ch/record/1260465.

[4] J. M. Jowett and M. Schaumann, "Overview of Heavy Ions in LHC Run 2," CERN. 2019. http://cds.cern.ch/record/2706427.

[5] M. Schaumann *et al.*, "First Xenon-Xenon Collisions in the LHC," in *9th International Particle Accelerator Conference*, p. MOPMF039. 2018.

[6] J. Jowett, "Colliding Heavy Ions in the LHC," in *9th International Particle Accelerator Conference*, p. TUXGBD2. 2018.

[7] J. Jowett *et al.*, "The 2015 Heavy-Ion Run of the LHC," in *7th International Particle Accelerator Conference*, p. TUPMW027. 2016.

[8] J. Jowett *et al.*, "The 2018 heavy-ion run of the LHC," in *10th International Particle Accelerator Conference*, p. WEYYPLM2. 2019.

[9] R. J. Glauber, "Theory of High Energy Hadron-Nucleus Collisions," in *High-Energy Physics and Nuclear Structure*, S. Devons, ed. Springer US, 1970.

[10] R. D. Woods and D. S. Saxon, "Diffuse surface optical model for nucleon-nuclei scattering," *Phys. Rev.* **95** (Jul, 1954) 577–578.

[11] **ALICE** Collaboration, "Centrality determination in heavy ion collisions,". https://cds.cern.ch/record/2636623. ALICE-PUBLIC-2018-011.

[12] M. L. Miller, K. Reygers, S. J. Sanders, and P. Steinberg, "Glauber modeling in high energy nuclear collisions," *Ann. Rev. Nucl. Part. Sci.* **57** (2007) 205–243, arXiv:nucl-ex/0701025.

[13] J. F. Owens, "Large-momentum-transfer production of direct photons, jets, and particles," *Rev. Mod. Phys.* **59** (Apr, 1987) 465–503.

[14] A. Bialas, M. Bleszynski, and W. Czyz, "Multiplicity Distributions in Nucleus-Nucleus Collisions at High-Energies," *Nucl. Phys. B* **111** (1976) 461–476.

[15] C. Loizides, J. Kamin, and D. d'Enterria, "Improved Monte Carlo Glauber predictions at present and future nuclear colliders," *Physical Review C* **97** no. 5, (5, 2018) .

[16] "Charged-particle multiplicity measurement in proton–proton collisions at $\sqrt{s} = 0.9$ and 2.36 TeV with ALICE at LHC,".

[17] **ALICE** Collaboration, P. (Cortese and others), "ALICE technical design report on forward detectors: FMD, T0 and V0,". http://cds.cern.ch/record/781854.

[18] D. J. Gross and F. Wilczek, "Ultraviolet behavior of non-abelian gauge theories," *Phys. Rev. Lett.* **30** (Jun, 1973) 1343–1346.

[19] H. D. Politzer, "Reliable perturbative results for strong interactions?" *Phys. Rev. Lett.* **30** (Jun, 1973) 1346–1349.

[20] Particle Data Group, "Review of Particle Physics," *Progress of Theoretical and Experimental Physics* **2020** no. 8, (08, 2020) .

[21] A. Bazavov *et al.*, "Equation of state in (2+1)-flavor QCD," *Physical Review D* **90** no. 9, (Nov, 2014) .

[22] R. S. Bhalerao, "Relativistic heavy-ion collisions,". http://cds.cern.ch/record/1695331.

[23] M. Alford, "Color Superconducting Quark Matter," *Annual Review of Nuclear and Particle Science* **51** no. 1, (Dec, 2001) 131–160.

[24] K. Fukushima and T. Hatsuda, "The phase diagram of dense QCD," *Reports on Progress in Physics* **74** no. 1, (Dec, 2010) 014001.

[25] J. D. Bjorken, "Highly relativistic nucleus-nucleus collisions: The central rapidity region," *Phys. Rev. D* **27** (Jan, 1983) 140–151.

[26] C. Grojean, ed., *2011 European School of High-Energy Physics*, CERN. CERN, Geneva, Dec, 2015. https://cds.cern.ch/record/1327568.

[27] J. Cleymans, "Status of the thermal model and chemical freeze-out," *EPJ Web of Conferences* **95** (2015) 03004.

[28] P. Koch, B. Muller, and J. Rafelski, "Strangeness production and evolution in quark gluon plasma," *Zeitschrift fur Physik A Atomic Nuclei* **324** no. 4, (Dec., 1986) 453–463.

[29] **STAR** Collaboration, G. Agakishiev *et al.*, "Strangeness Enhancement in Cu+Cu and Au+Au Collisions at $\sqrt{s_{NN}} = 200$ GeV," *Phys. Rev. Lett.* **108** (2012) 072301, arXiv:1107.2955 [nucl-ex].

[30] S. Singha, "Strange hadron and resonance production in Pb–Pb collisions at $\sqrt{s_{\rm NN}} = 2.76$ TeV with the ALICE experiment at LHC," *Nuclear Physics A* **904-905** (2013) 539c – 542c. The Quark Matter 2012.

[31] X.-N. Wang, *Quark–Gluon Plasma 5*. WORLD SCIENTIFIC, Feb., 2015. https://doi.org/10.1142/9533.

[32] F.-M. Liu and K. Werner, "On QGP Formation in pp Collisions at 7 TeV," *J. Phys. G* **38** (2011) 124183, arXiv:1106.5909 [hep-ph].

[33] R. Neufeld, I. Vitev, and B.-W. Zhang, "A possible determination of the quark radiation length in cold nuclear matter," *Physics Letters B* **704** no. 5, (2011) 590 – 595.

[34] F. Arleo *et al.*, "Revisiting scaling properties of medium-induced gluon radiation," *Physical Review D* **83** no. 11, (Jun, 2011) .

[35] F. Gelis, "Color glass condensate and glasma," *International Journal of Modern Physics A* **28** no. 01, (Jan, 2013) 1330001.

[36] C. Lourenço, R. Vogt, and H. K. Wohri, "Energy dependence of J/ψ absorption in proton-nucleus collisions," *Journal of High Energy Physics* **2009** no. 02, (Feb, 2009) 014–014.

[37] J. C. Collins, D. E. Soper, and G. F. Sterman, "Factorization of Hard Processes in QCD," *Adv. Ser. Direct. High Energy Phys.* **5** (1989) 1–91, arXiv:hep-ph/0409313.

[38] Y. L. Dokshitzer, "Calculation of the Structure Functions for Deep Inelastic Scattering and e+ e- Annihilation by Perturbation Theory in Quantum Chromodynamics.," *Sov. Phys. JETP* **46** (1977) 641–653.

[39] V. Gribov and L. Lipatov, "Deep inelastic electron scattering in perturbation theory," *Physics Letters B* **37** no. 1, (1971) 78 – 80.

[40] G. Altarelli and G. Parisi, "Asymptotic Freedom in Parton Language," *Nucl. Phys. B* **126** (1977) 298–318.

[41] J. Gao, L. Harland-Lang, and J. Rojo, "The structure of the proton in the lhc precision era," *Physics Reports* **742** (May, 2018) 1–121.

[42] S. Dulat, T.-J. Hou, *et al.*, "New parton distribution functions from a global analysis of quantum chromodynamics," *Physical Review D* **93** no. 3, (Feb, 2016) .

[43] "The ratio of the nucleon structure functions F_2^N for iron and deuterium," *Physics Letters B* **123** no. 3, (1983) 275 – 278.

[44] K. Eskola, V. Kolhinen, and P. Ruuskanen, "Scale evolution of nuclear parton distributions," *Nuclear Physics B* **535** no. 1-2, (Dec, 1998) 351–371.

[45] M. Arneodo, "Nuclear effects in structure functions," *Physics Reports* **240** no. 5, (1994) 301 – 393.

[46] P. Norton, "The EMC effect," *Rept. Prog. Phys.* **66** (2003) 1253–1297.

[47] J.-P. Blaizot, F. Gelis, and R. Venugopalan, "High energy pA collisions in the color glass condensate approach: gluon production and the Cronin effect," *Nuclear Physics A* **743** no. 1-3, (Oct, 2004) 13–56.

[48] K. Kovarik *et al.*, "nCTEQ15 - Global analysis of nuclear parton distributions with uncertainties in the CTEQ framework," *Phys. Rev. D* **93** no. 8, (2016) 085037, `arXiv:1509.00792 [hep-ph]`.

[49] K. J. Eskola, P. Paakkinen, H. Paukkunen, and C. A. Salgado, "EPPS16: Nuclear parton distributions with LHC data," *Eur. Phys. J. C* **77** no. 3, (2017) 163, `arXiv:1612.05741 [hep-ph]`.

[50] K. Eskola, H. Paukkunen, and C. Salgado, "EPS09 — A new generation of NLO and LO nuclear parton distribution functions," *Journal of High Energy Physics* **2009** no. 04, (Apr, 2009) 065–065.

[51] H. Paukkunen, "Nuclear PDFs Today," *PoS* **HardProbes2018** (2019) 014.

[52] J. F. Owens, J. Huston, C. E. Keppel, S. Kuhlmann, J. G. Morfín, F. Olness, J. Pumplin, and D. Stump, "Impact of new neutrino deep inelastic scattering and drell-yan data on large-xparton distributions," *Physical Review D* **75** no. 5, (Mar, 2007) .

[53] **CHORUS** Collaboration, "Measurement of nucleon structure functions in neutrino scattering," *Physics Letters B* **632** no. 1, (2006) 65 – 75.

[54] **ATLAS** Collaboration, "Z boson production in p+Pb collisions at $\sqrt{s_{\mathrm{NN}}} = 5.02$ TeV measured with the ATLAS detector," *Physical Review C* **92** no. 4, (Oct, 2015) .

[55] **CMS** Collaboration, "Study of Z boson production in pPb collisions at $\sqrt{s_{\mathrm{NN}}} = 5.02$ TeV" *Physics Letters B* **759** (Aug, 2016) 36–57.

[56] **CMS** Collaboration, "Study of W boson production in pPb collisions at $\sqrt{s_{\mathrm{NN}}} = 5.02$ TeV" *Physics Letters B* **750** (Nov, 2015) 565–586.

[57] A. Kusina, T. Ježo, *et al.*, "Impact of LHC vector boson production in heavy ion collisions on strange PDFs," *The European Physical Journal C* **80** no. 10, (Oct., 2020) .

[58] D. de Florian, R. Sassot, P. Zurita, and M. Stratmann, "Global analysis of nuclear parton distributions," *Phys. Rev. D* **85** (Apr, 2012) 074028.

[59] I. Helenius, K. Eskola, H. Honkanen, and C. Salgado, "Eps09s and eks98s: Impact parameter dependent npdf sets," *Nuclear Physics A* **904-905** (May, 2013) 999–1002.

[60] **ALEPH, DELPHI, L3, OPAL** Collaboration, "Precision electroweak measurements on the Z resonance," *Physics Reports* **427** no. 5-6, (May, 2006) 257–454.

[61] S. Catani, L. Cieri, G. Ferrera, D. de Florian, and M. Grazzini, "Vector Boson Production at Hadron Colliders: A Fully Exclusive QCD Calculation at Next-to-Next-to-Leading Order," *Physical Review Letters* **103** no. 8, (Aug, 2009) .

[62] **ATLAS** Collaboration, "Observation of Centrality-Dependent Acoplanarity for Muon Pairs Produced via Two-Photon Scattering in Pb+Pb Collisions at $\sqrt{s_{\mathrm{NN}}} = 5.02$ TeV with the ATLAS Detector," *Physical Review Letters* **121** no. 21, (Nov, 2018) .

[63] W. Zha, J. D. Brandenburg, Z. Tang, and Z. Xu, "Initial transverse-momentum broadening of Breit-Wheeler process in relativistic heavy-ion collisions," *Physics Letters B* **800** (Jan, 2020) 135089.

[64] Z. Conesa del Valle, "Vector bosons in heavy-ion collisions at the LHC," *The European Physical Journal C* **61** no. 4, (Apr, 2009) 729–733.

[65] **CMS** Collaboration, "New constraints of initial states in PbPb collisions with Z boson yields and azimuthal anisotropy at $\sqrt{s_{\mathrm{NN}}} = 5.02$ TeV" Tech. Rep. CMS-PAS-HIN-19-003, CERN, Geneva, 2020. https://cds.cern.ch/record/2719526.

[66] **LHCb** Collaboration, "Observation of Z production in proton-lead collisions at LHCb," *Journal of High Energy Physics* **2014** no. 9, (Sep, 2014) .

[67] **ALICE** Collaboration, "W and Z boson production in p-Pb collisions at $\sqrt{s_{\mathrm{NN}}} = 5.02$ TeV " *Journal of High Energy Physics* **2017** no. 2, (Feb, 2017) .

[68] **CMS** Collaboration, "Observation of nuclear modifications in $W^{\pm}$ boson production in pPb collisions at $\sqrt{s_{\mathrm{NN}}} = 8.16$ TeV " *Physics Letters B* **800** (Jan, 2020) 135048.

[69] **ALICE** Collaboration, "Z-boson production in p-Pb collisions at $\sqrt{s_{\mathrm{NN}}} = 8.16$ TeV and Pb-Pb collisions at $\sqrt{s_{\mathrm{NN}}} = 5.02$ TeV ," *Journal of High Energy Physics* **2020** no. 9, (Sept., 2020) .

[70] **ATLAS** Collaboration, "Measurement of Z boson Production in Pb-Pb collisions $\sqrt{s_{\mathrm{NN}}} = 2.76$ TeV with the ATLAS Detector," *Physical Review Letters* **110** no. 2, (Jan, 2013) .

[71] **ATLAS** Collaboration, "Measurement of the production and lepton charge asymmetry of W bosons in Pb+Pb collisions at $\sqrt{s_{\mathrm{NN}}} = 2.76$ TeV with the ATLAS detector," *The European Physical Journal C* **75** no. 1, (Jan, 2015) . http://dx.doi.org/10.1140/epjc/s10052-014-3231-6.

[72] **CMS** Collaboration, "Study of Z production in PbPb and pp collisions at $\sqrt{s_{\mathrm{NN}}} = 2.76$ TeV in the dimuon and dielectron decay channels," *Journal of High Energy Physics* **2015** no. 3, (Mar, 2015) .

[73] **CMS** Collaboration, "Study of W boson production in PbPb and pp collisions at $\sqrt{s_{\mathrm{NN}}} = 2.76$ TeV " *Physics Letters B* **715** no. 1-3, (Aug, 2012) 66–87.

[74] **ATLAS** Collaboration, "Z boson production in Pb+Pb collisions at $\sqrt{s_{\mathrm{NN}}} = 5.02$ TeV measured by the ATLAS experiment," *Physics Letters B* **802** (Mar, 2020) 135262.

[75] **ATLAS** Collaboration, "Measurement of $W^{\pm}$ boson production in Pb+Pb collisions at $\sqrt{s_{\mathrm{NN}}} = 5.02$ TeV with the ATLAS detector," *The European Physical Journal C* **79** no. 11, (Nov, 2019) .

[76] **ALICE** Collaboration, "Measurement of Z^0-boson production at large rapidities in Pb–Pb collisions at $\sqrt{s_{\mathrm{NN}}} = 5.02$ TeV ," *Physics Letters B* **780** (May, 2018) 372–383.

[77] **ALICE** Collaboration, G. Taillepied, "Electroweak-boson production in p-Pb and Pb-Pb collisions at the LHC with ALICE," *PoS* **HardProbes2020** (2020) 112, `arXiv:2008.07809 [nucl-ex]`.

[78] **LHCb** Collaboration, "Measurement of forward W and Z boson production in pp collisions at $\sqrt{s} = 8$ TeV," *Journal of High Energy Physics* **2016** no. 1, (Jan, 2016) .

[79] K. J. Eskola, I. Helenius, M. Kuha, and H. Paukkunen, "Shadowing in inelastic nucleon-nucleon cross section?," `arXiv:2003.11856 [hep-ph]`.

[80] **ALICE** Collaboration, S. Acharya and et al., "Centrality Dependence of the Charged-Particle Multiplicity Density at Midrapidity in Pb-Pb Collisions at $\sqrt{s_{NN}} = 5.02$ TeV," *Phys. Rev. Lett.* **116** (Jun, 2016) 222302.

[81] **ALICE** Collaboration, K. Aamodt *et al.*, "The ALICE experiment at the CERN LHC," *JINST* **3** (2008) S08002.

[82] M. Tarhini, *Measurement of Z-boson and J/ψ production in p-Pb and Pb-Pb collisions at* $\sqrt{s_{NN}} = 5.02$ *TeV with ALICE at the LHC*. Phd thesis, Université Paris-Saclay, June, 2017.

[83] J. Schukraft, "Heavy-ion physics with the ALICE experiment at the CERN Large Hadron Collider," *Philosophical Transactions of the Royal Society A: Mathematical, Physical and Engineering Sciences* **370** no. 1961, (Feb, 2012) 917–932.

[84] C. Oppedisano, "p–Pb collisions: Particle production and centrality determination in ALICE," *Nuclear Physics A* **932** (2014) 399 – 403. Hard Probes 2013.

[85] G. Dellacasa *et al.*, *ALICE time projection chamber: Technical Design Report*. Technical Design Report ALICE. CERN, Geneva, 2000. https://cds.cern.ch/record/451098.

[86] **ALICE** Collaboration, "The ALICE Transition Radiation Detector: Construction, operation, and performance," *Nuclear Instruments and Methods in Physics Research Section A: Accelerators, Spectrometers, Detectors and Associated Equipment* **881** (2018) 88 – 127.

[87] **ALICE** Collaboration, *ALICE Time-Of-Flight system (TOF): Technical Design Report*. Technical Design Report ALICE. CERN, Geneva, 2000. https://cds.cern.ch/record/430132.

[88] J. Allen *et al.*, "ALICE DCal: An Addendum to the EMCal Technical Design Report Di-Jet and Hadron-Jet correlation measurements in ALICE," Tech. Rep. CERN-LHCC-2010-011. ALICE-TDR-14-add-1, Jun, 2010. https://cds.cern.ch/record/1272952.

[89] **ALICE** Collaboration, *ALICE dimuon forward spectrometer: Technical Design Report*. Technical Design Report ALICE. CERN, Geneva, 1999. https://cds.cern.ch/record/401974.

[90] E. Mathieson, "Cathode charge distributions in multiwire chambers: 4. Empirical formula for small anode-cathode separation," *Nuclear Instruments and Methods in Physics Research Section A: Accelerators, Spectrometers, Detectors and Associated Equipment* **270** no. 2, (1988) 602 – 603.

[91] **ALICE** Collaboration, "ALICE: Physics Performance Report, Volume II," *Journal of Physics G* **32** (2006) 1295 – 2040.

[92] ALICE Internal Note, *Numerical Simulations and Offline Reconstruction of the Muon Spectrometer of ALICE*, 2020. https://edms.cern.ch/document/1054937/1.

[93] M. Chojnacki, "Soft probes of the Quark-Gluon Plasma measured by ALICE," *Nuclear and Particle Physics Proceedings* **273-275** (2016) 1553 – 1558. 37th International Conference on High Energy Physics (ICHEP).

[94] E. Bartsch, "Recent results on light (anti-)nuclei production with ALICE at the LHC," *Journal of Physics: Conference Series* **1602** (Jul, 2020) 012022.

[95] **ALICE** Collaboration, "Anisotropic Flow of Charged Particles in Pb-Pb Collisions $\sqrt{s_{\mathrm{NN}}} = 5.02$ TeV " *Physical Review Letters* **116** no. 13, (Apr, 2016) .

[96] **ALICE** Collaboration, "Production of charged pions, kaons, and (anti-)protons in Pb-Pb and inelastic pp collisions at $\sqrt{s_{\mathrm{NN}}} = 5.02$ TeV " *Physical Review C* **101** no. 4, (Apr, 2020) .

[97] **ALICE** Collaboration, "Analysis of the apparent nuclear modification in peripheral Pb–Pb collisions at 5.02 TeV," *Physics Letters B* **793** (Jun, 2019) 420–432.

[98] C. Loizides and A. Morsch, "Absence of jet quenching in peripheral nucleus–nucleus collisions," *Physics Letters B* **773** (Oct, 2017) 408–411.

[99] R. Arnaldi, "Experimental overview on quarkonium production," *Nuclear Physics A* **956** (Dec, 2016) 128–135.

[100] J. Hong and S. H. Lee, "Y(1S) transverse momentum spectra through dissociation and regeneration in heavy-ion collisions," *Physics Letters B* **801** (2020) 135147.

[101] J.-P. Lansberg and H.-S. Shao, "Towards an automated tool to evaluate the impact of the nuclear modification of the gluon density on quarkonium, D and B meson production in proton–nucleus collisions," *The European Physical Journal C* **77** no. 1, (Dec, 2016) .

[102] J. Wenninger, "Operation and Configuration of the LHC in Run 2,". `https://cds.cern.ch/record/2668326`.

[103] **ALICE** Collaboration, "Performance of the ALICE experiment at the CERN LHC," *International Journal of Modern Physics A* **29** no. 24, (Sep, 2014) 1430044.

[104] P. Cortese *et al.*, "Performance of the ALICE Zero Degree Calorimeters and upgrade strategy," *Journal of Physics: Conference Series* **1162** (Jan, 2019) 012006.

[105] S. Aziz. Private communication.

[106] G. R. Lynch and O. I. Dahl, "Approximations to multiple Coulomb scattering," *Nuclear Instruments and Methods in Physics Research Section B: Beam Interactions with Materials and Atoms* **58** no. 1, (1991) 6 – 10.

[107] S. Alioli, P. Nason, C. Oleari, and E. Re, "NLO vector-boson production matched with shower in POWHEG," *Journal of High Energy Physics* **2008** no. 07, (Jul, 2008) 060–060.

[108] M. Oreglia, *A Study of the Reactions $\psi' \to \gamma\gamma\psi$*. Phd thesis, 12, 1980. Appendix D.

[109] T. Sjöstrand, S. Mrenna, and P. Skands, "PYTHIA 6.4 physics and manual," *Journal of High Energy Physics* **2006** no. 05, (May, 2006) 026–026.

[110] V. Blobel and C. Kleinwort, "A New method for the high precision alignment of track detectors," in *Conference on Advanced Statistical Techniques in Particle Physics*. 6, 2002. arXiv:hep-ex/0208021.

[111] M. Cacciari, S. Frixione, and P. Nason, "The p_{T} spectrum in heavy-flavour photoproduction," *Journal of High Energy Physics* **2001** no. 03, (Mar, 2001) 006–006.

[112] O. Bugnon. Private communication.

[113] P. Pillot. Private communication.

[114] R. Boughezal *et al.*, "Color singlet production at NNLO in MCFM," *Eur. Phys. J. C* **77** no. 1, (2017) 7, arXiv:1605.08011 [hep-ph].

[115] R. Gavin, Y. Li, F. Petriello, and S. Quackenbush, "FEWZ 2.0: A code for hadronic Z production at next-to-next-to-leading order," *Comput. Phys. Commun.* **182** (2011) 2388–2403, arXiv:1011.3540 [hep-ph].

[116] A. Rotondi, P. Pedroni, and A. Pievatolo, *Probabilità, Statistica e Simulazione*. Springer Milan, 2012.

[117] "ALICE Collaboration, Preliminary results on W production in p-Pb collisions at 8.16 TeV [September 2020]." https://alice-figure.web.cern.ch/node/17608.

[118] **ATLAS** Collaboration, "Measurements of W and Z boson production in pp collisions at $\sqrt{s} = 5.02$ TeV with the ATLAS detector," *The European Physical Journal C* **79** no. 2, (Feb, 2019) .

[119] P. Antonioli *et al.*, "INFN What Next: Ultra-relativistic Heavy-Ion Collisions," *Frascati Phys. Ser.* **62** (2016) , arXiv:1602.04120 [nucl-ex].

[120] J. M. Jowett, M. Schaumann, and R. Versteegen, "Heavy ion operation from run 2 to HL-LHC,". https://cds.cern.ch/record/1977371.

[121] G. Eulisse, P. Konopka, M. Krzewicki, M. Richter, D. Rohr, and S. Wenzel, "Evolution of the ALICE software framework for Run 3," *EPJ Web Conf.* **214** (2019) 05010.

[122] P. Buncic, M. Krzewicki, and P. Vande Vyvre, "Technical Design Report for the Upgrade of the Online-Offline Computing System," Tech. Rep. CERN-LHCC-2015-006. ALICE-TDR-019, Apr, 2015. http://cds.cern.ch/record/2011297.

[123] **ALICE** Collaboration, "Upgrade of the ALICE Time Projection Chamber," Tech. Rep. CERN-LHCC-2013-020. ALICE-TDR-016, Oct, 2013. http://cds.cern.ch/record/1622286.

[124] **ALICE** Collaboration, P. Antonioli, A. Kluge, and W. Riegler, "Upgrade of the ALICE Readout and Trigger System," Tech. Rep. CERN-LHCC-2013-019. ALICE-TDR-015, Sep, 2013. https://cds.cern.ch/record/1603472.

[125] **ALICE** Collaboration, "Addendum of the Letter of Intent for the upgrade of the ALICE experiment : The Muon Forward Tracker," Tech. Rep. CERN-LHCC-2013-014, CERN, Geneva, Aug, 2013. http://cds.cern.ch/record/1592659.

[126] N. Valle, "Ageing tests of the Hybrid Modules for the ALICE ITS Upgrade," *PoS* **Vertex2019** (2020) 064.

[127] **ALICE** Collaboration, "ALICE upgrade physics performance studies for 2018 Report on HL/HE-LHC physics,". https://cds.cern.ch/record/2661798.

[128] J. W. van Hoorn, *Study and Development of a novel Silicon Pixel Detector for the Upgrade of the ALICE Inner Tracking System*. PhD thesis, TU Vienna, 10, 2015.

[129] "TowerJazz [September 2020]." http://www.towersemi.com.

[130] **ALICE** Collaboration, M. Mager, "ALPIDE, the Monolithic Active Pixel Sensor for the ALICE ITS upgrade," *Nucl. Instrum. Meth. A* **824** (2016) 434–438.

[131] **ALICE** Collaboration, G. Aglieri Rinella, "The ALPIDE pixel sensor chip for the upgrade of the ALICE Inner Tracking System," *Nucl. Instrum. Meth. A* **845** (2017) 583–587.

[132] **ALICE** Collaboration, "Technical design report for the upgrade of the ALICE inner tracking system," *Journal of Physics G: Nuclear and Particle Physics* **41** no. 8, (Jul, 2014) 087002.

[133] D. Colella, "ALICE Inner Tracking System Upgrade: construction and commissioning,". http://cds.cern.ch/record/2705698.

[134] G. Fiorenza, V. Manzari, C. Pastore, and V. Valentino, "The Hybrid Integrated Circuit of the ALICE Inner Tracking System upgrade," *Nuovo Cimento C* **39** no. 1, (2016) 257. http://cds.cern.ch/record/2282359.

[135] **ALICE** Collaboration, D. Andreou, "The upgrade of the ALICE Inner Tracking System," *JINST* **14** no. 05, (2019) C05004, arXiv:1904.13237 [physics.ins-det].

[136] L. A. Escobar and W. Q. Meeker, "A review of accelerated test models," *Statistical Science* **21** no. 4, (Nov, 2006) 552–577.

[137] R. Newton, *Scattering Theory of Waves and Particles*. Dover Books on Physics.

Acknowledgements

During these years my professional experience has grown thanks to the support of several people.

I would like to thank my supervisor Gianluigi Boca for his continuous support and assistance at every stage of my PhD journey. A big thank you also to Germano Bonomi, Alberto Rotondi and the entire group of colleagues in Pavia and Brescia.

I'm deeply grateful to Vito Manzari and to the ALICE group of Bari (special thanks to the patience of Domenico Colella) for what they taught me and for the opportunity to work in the ITS team.

A large number of "muon" people helped me to refine the results presented here. Sizar[1], Guillaume, Ophelie, Mohamad are just the youngest ones (I guess).

I also thank Daniele Pedrini and Alessandro Baldini for being referees of this thesis. I received from them precious inputs and extremely valuable suggestions.

Finally I want to acknowledge INFN for the opportunities offered to young physicists.

[1] Sizar, please find the efficiencies on page 76 :)